AD-A038 361 STANFORD UNIV CALIF DEPT OF CIVIL ENGINEERING F/G 8/3
WAVE-INDUCED VELOCITIES AND TURBULENT REYNOLDS STRESSES ABOVE A--ETC(U)
DEC 76 S P CHAO, E Y HSU, R L STREET N00014-76-C-0155
UNCLASSIFIED TR-204 NL

1 OF 2
AD A038361




AD A038361

(12)

FG

Technical Report No. 204

WAVE-INDUCED VELOCITIES AND TURBULENT REYNOLDS STRESSES ABOVE AN AIR-WATER INTERFACE

by

Shen P. Chao
En Y. Hsu
Robert L. Street

DDC
APR 19 1977
C

This research was supported by
Office of Naval Research
Contract No. N00014-76-C-0155
and
National Science Foundation
Grant No. ENG 73-04190

DISTRIBUTION STATEMENT A
Approved for public release;
Distribution Unlimited

December 1976

COPY

Department of CIVIL ENGINEERING
STANFORD UNIVERSITY

Department of Civil Engineering

Stanford University

Stanford, California

(6) WAVE-INDUCED VELOCITIES AND TURBULENT REYNOLDS STRESSES ABOVE AN AIR-WATER INTERFACE.

by

(10) Shen P. Chao

En Y. Hsu

Robert L. Street

DDC
AVAILABILITY
APR 19 1977
C

(9) Technical Report No. 204

(14) TR-204

This research was supported by

Office of Naval Research

(13) Contract No. N00014-76-C-0155, NSF-ENG-73-04190

and

National Science Foundation

Grant No. ENG 73-04190

ACCESSION for
NTIS White Section
DDC Buff Section
UNANNOUNCED
JUSTIFICATION
Form 50
on file
BY
DISTRIBUTION/AVAILABILITY CODES
Dist. AVAIL. and/or SPECIAL
A

(11) December 1976

(12) 173 p.

400 117

ABSTRACT

The progressive, sinusoidal water-wave-induced perturbations in a turbulent air flow above an air-water interface were studied. The velocity field was measured both in fixed and wave-following reference frames with a cross hot-film probe. Both the magnitude and phase of the wave-induced velocities and turbulent Reynolds stresses were obtained across the turbulent boundary layer.

The mean momentum transfer from the wind to water waves is comprised of:

(1) A critical layer part, which is proportional to the product of the velocity-profile curvature and the mean square of the wave-induced vertical velocity at the critical height, where the mean wind speed is equal to the wave speed.

(2) A vertical integral across the turbulent boundary layer of the mean product of the wave-induced vertical velocity and vorticity associated with the wave-induced turbulent Reynolds stresses.

(3) A contribution associated with the wave-induced turbulent Reynolds stresses at the air-water interface.

These quantities were evaluated for different wind speeds. The calculated results showed that the wave-induced turbulent Reynolds stresses are important in the evaluation of momentum transfer from wind to waves, their contribution comprising about 90 percent of the total transfer, while the critical layer contribution is about 10 percent.

The measured wave-induced velocities and turbulent Reynolds stresses were compared with numerical modeling results based on an assumed mean eddy viscosity and turbulent kinetic energy closure models of Norris and Reynolds. No definite conclusion was reached from the comparison because of the lack of experimental data close to the air-water interface.

ACKNOWLEDGEMENTS

Appreciation is expressed to Dr. L. H. Norris and Professor W. C. Reynolds for their help in using their computer program and many valuable discussions. Special appreciation is reserved for Mr. T. R. Mogel, for his assistance with instrumentation problem and computer operation in data reduction, and for Mr. C. T. Hsu for many valuable discussions during the course of this study. The drafting of the figures by Ms. Andrea Gill and the typing of the manuscript by Ms. Doris Yee are gratefully acknowledged.

Financial support for this investigation was provided by The Office of Naval Research under Contract No. N00014-76-C-0155 and The National Science Foundation under Grant No. ENG 73-04190.

TABLE OF CONTENTS

		Page
1.	INTRODUCTION	1
	1.1 Motivation and Previous Work	1
	1.2 Objectives of the Study	10
	1.3 Scope of the Study	11
2.	THEORETICAL BACKGROUND	13
	2.1 Decomposition and Averages	13
	2.2 The Governing Equations	15
	2.3 Momentum Transfer from Wind to Wave	18
3.	EXPERIMENTAL METHODS AND DATA REDUCTION	23
	3.1 Experimental Facilities	23
	3.1.1 Wind Wave Channel	23
	3.1.2 Probe Carriage and Traversing Mechanism	25
	3.1.3 Wave-Following System	25
	3.2 Instruments	27
	3.2.1 Hot Film Probe	27
	3.2.2 Pitot-Static Tube	28
	3.2.3 Wave Height Gauge	29
	3.3 Data Acquisition and Reduction	29
	3.3.1 Data Acquisition and Reduction System	29
	3.3.2 Data Acquisition Procedures	30
	3.3.3 Data Reduction Precedures	31
	3.3.4 Cross-Correlation	32
	3.3.5 Cross-Spectral Function and Coherence	33
4.	EXPERIMENTAL RESULTS AND MOMENTUM TRANSFER FROM WIND TO WAVE	37
	4.1 Mean Velocity and Turbulence Intensities	38
	4.2 Wave-Induced Velocites and Tuebulent Reynolds Stresses	40
	4.2.1 Fixed Probe Measurements	40
	4.2.2 Wave Follower Measurements	46

Page

4.3 Momentum Transfer From Wind to Wave..... 51

5. THEORETICAL MODELING..... 55

5.1 Transformation of Coordinates..... 57

5.2 Eddy Viscosity Model..... 58

5.2.1 Inner Region..... 60

5.2.2 Outer Region..... 61

5.3 Turbulent Kinetic Energy Model..... 64

5.3.1 Mean Turbulent Kinetic Energy..... 69

5.3.2 The Model Constants..... 70

5.4 Boundary Condition..... 73

5.5 Model Solutions and Comparison with the Data..... 73

5.5.1 No Critical Layer Case ($U_\infty/C = 0.883$)..... 75

5.5.2 Thick Critical Layer Case ($U_\infty/C = 1.115$)..... 76

5.5.3 Thin Critical Layer Case ($U_\infty/C = 2.283$)..... 77

5.6 Discussion..... 78

6. CONCLUSIONS AND RECOMMENDATIONS..... 81

REFERENCES..... 85

APPENDICES..... 89

I. UNCERTAINTY ANALYSIS..... 89

II. EXPERIMENTAL DATA..... 91

LIST OF FIGURES

Figure		Page
2.1	Cross Correlation and Decomposition	107
3.1	Schematic of the Wind-Wave Facility	108
3.2	Schematic of Probe Carriage	109
3.3	Wave Follower Installation Outside the Wind Wave Channel	110
3.4	Typical Hot Film Calibration Curves	111
3.5	Pressure Transducer Calibration Curves	112
3.6	Capacitance Type Wave Gauge	113
3.7	Typical Wave Height Gauge Calibration	114
3.8	Typical Correlations of $R_{\eta\tilde{u}}(\tau)$, $R_{\eta\tilde{v}}(\tau)$ and $R_{\eta\tilde{r}_{ij}}(\tau)$	115
3.9	Typical Spectrum of $\tilde{r}_{ij}$	116
3.10	Typical Coherence Spectrum of $\tilde{r}_{22}$	117
4.1	Mean Velocity Profile Above the Mechanically-Generated Waves	118
4.2a	Turbulent Intensities and Reynolds Stress for $U_\infty/C = 1.115$ in Wave Following Reference Frame	119
4.2b	Turbulent Intensities and Reynolds Stress for $U_\infty/C = 1.115$ in Fixed Reference Frame	120
4.3	Magnitude Distributions of $\tilde{u}$ and $\tilde{v}$ and Computed Results for $U_\infty/C = 0.883$	121
4.4	Phase Distributions of $\tilde{u}$ and $\tilde{v}$ and Computed Results for $U_\infty/C = 0.883$	122
4.5	Magnitude Distributions of $\tilde{u}$ and $\tilde{v}$ and Computed Results for $U_\infty/C = 1.115$	123
4.6	Phase Distributions of $\tilde{u}$ and $\tilde{v}$ and Computed Results for $U_\infty/C = 1.115$	124
4.7	Magnitude Distrivutions of $\tilde{u}$ and $\tilde{v}$ for $U_\infty/C = 1.34$	125
4.8	Phase Distributions of $\tilde{u}$ and $\tilde{v}$ for $U_\infty/C = 1.34$	126
4.9	Magnitude Distributions of $\tilde{u}$ and $\tilde{v}$ for $U_\infty/C = 1.836$	127
4.10	Phase Distributions of $\tilde{u}$ and $\tilde{v}$ for $U_\infty/C = 1.836$	128

Figure		Page
4.11	Magnitude Distributions of $\tilde{u}$ and $\tilde{v}$ and Computed Results for $U_\infty/C = 2.283$	129
4.12	Phase Distributions of $\tilde{u}$ and $\tilde{v}$ and Computed Results for $U_\infty/C = 2.283$	130
4.13a	Magnitude Distribution of $\tilde{r}_{11}$ and Computed Results for $U_\infty/C = 0.883$	131
4.13b	Magnitude Distribution of $\tilde{r}_{22}$ and Computed Results for $U_\infty/C = 0.883$	132
4.13c	Magnitude Distribution of $\tilde{r}_{12}$ and Computed Results for $U_\infty/C = 0.883$	133
4.14a	Phase Distribution of $\tilde{r}_{11}$ and Computed Results for $U_\infty/C = 0.883$	134
4.14b	Phase Distribution of $\tilde{r}_{22}$ and Computed Results for $U_\infty/C = 0.883$	135
4.14c	Phase Distribution of $\tilde{r}_{12}$ and Computed Results for $U_\infty/C = 0.883$	136
4.15a	Magnitude Distribution of $\tilde{r}_{11}$ and Computed Results for $U_\infty/C = 1.115$	137
4.15b	Magnitude Distribution of $\tilde{r}_{22}$ and Computed Results for $U_\infty/C = 1.115$	138
4.15c	Magnitude Distribution of $\tilde{r}_{12}$ and Computed Results for $U_\infty/C = 1.115$	139
4.16a	Phase Distribution of $\tilde{r}_{11}$ and Computed Results for $U_\infty/C = 1.115$	140
4.16b	Phase Distribution of $\tilde{r}_{22}$ and Computed Results for $U_\infty/C = 1.115$	141
4.16c	Phase Distribution of $\tilde{r}_{12}$ and Computed Results for $U_\infty/C = 1.115$	142
4.17	Magnitude Distributions of $\tilde{r}_{ij}$ for $U_\infty/C = 1.34$	143
4.18	Phase Distributions of $\tilde{r}_{ij}$ for $U_\infty/C = 1.34$	144
4.19	Magnitude Distributions of $\tilde{r}_{ij}$ for $U_\infty/C = 1.836$	145
4.20	Phase Distributions of $\tilde{r}_{ij}$ for $U_\infty/C = 1.836$	146

Figure		Page
4.21a	Magnitude Distribution of $\tilde{r}_{11}$ and Computed Results for $U_\infty/C = 2.283$	147
4.21b	Magnitude Distribution of $\tilde{r}_{22}$ and Computed Results for $U_\infty/C = 2.283$	148
4.21c	Magnitude Distribution of $\tilde{r}_{12}$ and Computed Results for $U_\infty/C = 2.283$	149
4.22a	Phase Distribution of $\tilde{r}_{11}$ and Computed Results for $U_\infty/C = 2.283$	150
4.22b	Phase Distribution of $\tilde{r}_{22}$ and Computed Results for $U_\infty/C = 2.283$	151
4.22c	Phase Distribution of $\tilde{r}_{12}$ and Computed Results for $U_\infty/C = 2.283$	152
4.23	Magnitude Distributions of Wave Induced Velocities: Wave Follower Results	153
4.24	Phase Distributions of Wave Induced Velocities: Wave Follower Results	154
4.25	Magnitude Distribution of $\tilde{r}_{11}$: Wave Follower Results	155
4.26	Magnitude Distribution of $\tilde{r}_{22}$: Wave Follower Results	156
4.27	Magnitude Distribution of $\tilde{r}_{12}$: Wave Follower Results	157
4.28a	Phase Distributions of $\tilde{r}_{ij}$: Wave Follower Results	158
4.28b	Phase Distributions of r_{ij}: Wave Follower Results	159
5.1	Lines of Constant y^*	160
5.2	Comparison of Mean Velocity Profile	161
5.3	Comparison of Turbulent Kinetic Energy	162

LIST OF TABLES

Table		Page
4-1	Free Stream Velocity Conditions.....	38
4-2	Comparison of Estimated and Measured (Fixed Probe Data) Phase Lags of $\tilde{u}$ and $\tilde{v}$ at the Lowest Measurement Point.....	43
4-3	Measured Values (Wave Follower Data) of Wave-Induced Vertical Velocity at the Lowest Measurement Point.....	47
4-4	Comparison of $\tilde{u}$ and $\tilde{v}$ Data Both in the Fixed and Wave Following Frames.....	49
4-5	Experimental Results of Momentum Transfer from Wind to Waves.....	52
4-6	Experimental Results of F_{wl} (Fixed Probe Data).....	53

NOMENCLATURE

A^+	sublayer thickness parameter in Van Driest's Law
C	wave celerity
c_1, c_2, c_3, c_4 and c_5	constants used in turbulent kinetic energy closure model
$C_{\eta f}$	cospectra of η and f
D	half depth of the wind-wave tunnel above the water surface
$\mathfrak{D}$	turbulence dissipation
$\tilde{\mathfrak{D}}$	periodic component of turbulence dissipation
E	eddy viscosity function for mean flow; voltage
F	mean momentum transfer from wind to wave; $F = F_c + F_{w1} + F_{w2}$, F_c = contribution due to critical layer; F_{w1} = contribution due to $\tilde{r}_{ij}$ at all layers above the wave surface; F_{w2} = contribution due to $\tilde{r}_{ij}$ at the air-water interface
f	arbitrary quantities of interest; frequency
$\overline{f}$	time averaged values of f
$\tilde{f}$	wave-induced perturbation quantities of f
f'	background random fluctuations of f
$\lvert \tilde{f} \rvert$	amplitude of the wave-induced signals
$< f >$	phase averaged values of f; $< f > = \overline{f} + \tilde{f}$
G_f	auto spectral function of f
$G_{\eta f}$	cross spectral function of η and f
h	distance between probe and mean water surface elevation in a fixed coordinate system
h_f	distance between probe and wave surface in a wave-following coordinate system

i	$(-1)^{\frac{1}{2}}$
K	wave number; $2\pi / \lambda$
ℓ	turbulent length scale function
L	turbulent length scale for mean flow
n	summation index; frequency
N	limit of summation
p	instantaneous pressure signal; $\bar{p}$ mean pressure; $\tilde{p}$ wave-induced pressure signal; p' turbulent pressure fluctuations
q^2	turbulent kinetic energy
$\tilde{q}^2$	periodic component of turbulent kinetic energy
Q^2	mean turbulent kinetic energy
Q^{+2}	non-dimensional mean turbulent kinetic energy in wall coordinate; $Q^{+2} = (Q/u^*)^2$ in y^+ coordinates
$Q_{\eta f}$	quadrature spectra of η and f
r_{ij}	negative of the turbulent Reynolds stresses
$\tilde{r}_{ij}$	periodic component of r_{ij}; $\tilde{r}_{ij} = < u_i' u_j' > - \overline{u_i' u_j'}$
R_{ij}	negative of the mean turbulent Reynolds stresses
$R_{\eta f}$	cross correlation function between η and f
Re	Reynolds number
S_{ij}	mean strain rate
$\tilde{S}_{ij}$	oscillating strain rate
t	time in untransformed coordinate system
t^*	time in transformed coordinate system
T	period for averaging; wave period
u_i	velocity component in the i-direction; $u_i = \bar{u}_i + \tilde{u}_i + u_i'$; $u_i = \bar{U}_i$

u, v	velocity components in the x and y directions, respectively
U_∞	free-stream velocity
u_d	velocity of the drifting current
U_{eff}	effective cooling velocity of hot film
u^*	shear velocity
u^+	x direction velocity component in wall coordinate; $u^+ = u/u^*$
$x_i = \underline{x}$	$(x_1, x_2, x_3) = (x, y, z)$; x, y, z directions in untransformed coordinate system
x^*, y^*, z^*	directions in the transformed coordinate system
y^+	normalized x_2 coordinate; $y^+ = yu^*/\nu$
y_c	critical height; the height where the local mean velocity equals the wave celerity

Greek symbols

δ	channel boundary layer thickness
τ	time delay in the correlation function
ε	eddy viscosity function
$\tilde{\varepsilon}$	periodic component of ε
θ	phase lag of the wave-induced signal with respect to the waveform; $\tilde{u}_\theta = \theta_1$, $\tilde{v}_\theta = \theta_2$; phase lags of $\tilde{r}_{11} = \theta_{11}$, $\tilde{r}_{22} = \theta_{22}$ and $\tilde{r}_{12} = \theta_{12}$
$\theta_{\eta f}$	phase relation between η and f
κ	von Kármán constant
ρ_a	density of air
λ	wave length

ν	kinematic viscosity
ν_T	eddy kinematic viscosity
μ	molecular viscosity
η	water surface elevation
$\lvert\eta\rvert$	amplitude of the mechanically generated wave
ω	angular wave frequency rad/sec; vorticity associated with $\tilde{r}_{ij}$
Π	wake parameter
Ω	wave-induced vorticity; $\Omega = \frac{\partial \tilde{u}}{\partial y} - \frac{\partial \tilde{v}}{\partial x}$

1. INTRODUCTION

1.1 Motivation and Previous Work

The search for an understanding of the physical mechanisms involved in the generation and maintenance of waves by wind has been one of the most difficult in the field of fluid mechanics. It is only in the past two decades that much progress has been made. In a survey paper, entitled "Wave Generation by Wind", Ursell (1956) commenced: "Wind blowing over a water surface generates waves in the water by physical processes which cannot be regarded as known". His review stimulated wide interest; since then many investigators have contributed to the clarification of the processes, and a general theoretical frame-work has emerged. The first significant contributions to the dynamical wave theory were Phillips' (1957) and Miles' (1957) theories, which yielded rigorous transfer expressions for certain aspects of the wave-atmosphere interactions.

Phillips' (1957) resonance mechanism accounts for the initial linear growth of a wave spectrum under the influence of random pressure fluctuations. The statistical properties of the pressure fluctuations are associated with the atmospheric turbulent wind field and assumed to be independent of the waves generated. The assumptions fail when wave amplitude is sufficiently large. If the waves, having already been initiated, are of sufficient amplitude the air flow over the undulatory surface will cause the generation of pressure differences along the perturbed water surface. Miles' (1957) inviscid model described the energy trans-

fer between the wind and the water wave by the wave-induced pressure component that is in phase with the vertical velocity component of the water surface. The model considered air flow over a single frequency progressive wave of infinitesimal amplitude. Turbulence in the air stream was neglected except in maintaining a prescribed parallel shear flow with logarithmic velocity distribution. The feedbacks from the wave were the wave-induced air velocity and the pressure perturbation. The wave-induced air velocity was assumed to be two dimensional and small enough to be unimportant in the nonlinear processes of the equations of motion. The flowfield in the water was considered inviscid, irrotational and incompressible. Mean water currents were assumed to be absent. The equations governing the wave-induced perturbations in the air stream are exactly the same as those in laminar-instability theory.

Miles' inviscid model has been tested both in the field and in the laboratory through the measurements of wave growth-rate and wave-induced pressure in the air stream. Wave growth measurements in the field by Snyder and Cox (1966) and by Barnett and Wilkerson (1967) indicated that the observed exponential growth rate exceeds that predicted by the inviscid model by an order of magnitude. The wave growth-rate obtained from Dobson's (1971) power and cross-power spectra of wave elevation and pressure agrees with the field measured wave growth-rate, but the measured wave growth-rate is larger by a factor between 5 to 8 than Miles' inviscid theoretical predictions.

Shemdin and Hsu (1967) investigated the wave-induced pres-

sure distribution over mechanically generated waves. Their results indicated that the growth rate was larger by a factor of about two than that indicated by the inviscid results. Bole and Hsu (1969) studied the growth of mechanically-generated waves under the action of wind in a channel. Based on the measured spatial growth of waves along the channel, they obtained the growth rate of the waves and found the measured growth-rate larger by a factor from one to ten than Miles' estimates. In order to examine the effect of neglecting the viscosity in Miles' inviscid model (the quasilaminar model), Benjamin (1959) and Miles (1959) included viscous term in the equations of motion and carried out the analysis in curvilinear, orthogonal coordinates. They found that the viscous effects are of second order and can be neglected.

A further contribution to dynamical wave theory was made by Phillips (1960) and Hasselmann (1962, 1963). They studied the energy transfer due to nonlinear wave-wave interactions. The most important simple result of these calculations is that the time scale for the interaction is much greater than the time scale of wave growth; the wave-wave interactions cannot transfer energy from a band of wave number as rapidly as it is acquired from the wind. Moreover, the energy transfer among the different components is weak and selective. Only for certain combinations of wave numbers and frequencies, which satisfy the resonance condition does the nonlinear interaction produce a continuing energy flux from one to another.

Hasselmann (1968) applied the theory of weak interaction in random fields to describe the wave field within the coupled ocean-atmosphere system. In his description, the lowest-order of transfer expressions for wave-atmosphere interactions are the Phillips and Miles processes, a nonlinear correction to Miles process, and wave-turbulence interactions. He stated that: "Present data suggests that the wave-turbulence interactions may be the most important of the four".

The influence of the background turbulent field on the wave-induced perturbation appears in the governing equations for the wave-induced field as an oscillation of the background turbulent Reynolds stresses. The significance of the wave-induced turbulent Reynolds stresses were revealed from the failure of Miles' inviscid models (1957, 1959), in which the wave-induced turbulent Reynolds stresses were neglected.

In predicting the wave-induced velocities and pressure in the turbulent air stream, the difficulties are that the dynamic equations describing those quantities in a turbulent flow are not closed, due to the presence of induced turbulent Reynolds stresses. There are more unknowns than equations. Efforts to seek closure by deriving dynamic equations for the induced turbulent Reynolds stresses cannot solve the closure problem but only create more unknown quantities. But the equations for the induced turbulent Reynolds stresses (see Reynolds and Hussain 1972) indicate that the induced turbulent Reynolds stresses are of the same order of magnitude as the other disturbance quantities in the air stream. Thus, even

for weak organized motions in the air stream one should expect oscillations of the turbulent Reynolds stresses of comparable magnitude.

Because of the lack of an adequate theory of turbulence at the present, plausible assumptions have been made through the use of the turbulent eddy viscosity and turbulent kinetic energy models in which induced turbulent Reynolds stresses are retained. The eddy viscosity and turbulent energy closure models have been carried out by Davis (1970), Hussain and Reynolds (1970), Saeger and Reynolds (1971), Long (1971), Townsend (1972), Davis (1972), Acharya and Reynolds (1975) and Norris and Reynolds (1975). Their results were compared with the experimental data of Stewart (1970), Hussain and Reynolds (1970), Saeger and Reynolds (1971), Dobson (1971), Acharya and Reynolds (1975), and Norris and Reynolds (1975).

Davis (1970) proposed that the Reynolds shear stress of the background turbulence is distorted by an amount proportional to the displacement that streamlines would have in an inviscid uniform velocity flow over the wavy boundary, the proportionality constant being the normal gradient of the turbulent shear stress in the undisturbed flow. He also proposed that the ratio between the different components of induced turbulent Reynolds stresses is the same as that of the turbulent Reynolds stresses in the turbulent boundary layer above a flat rigid surface. Numerical predictions based on this model are inconsistent with Stewart's (1970) wave-induced velocity data. Generally, at high wind speeds the predicted magnitudes of wave-induced velocities are larger than the

measured values, whereas at low wind speeds, the inverse is often the case. Davis also did quasilaminar calculations, whose predicted values of wave-induced velocities showed little agreement with the experimental data of Stewart (1970); the amplitudes tend to be too high at high wind speeds and the phases show poor agreement. The calculations also show the predicted wave-induced velocity data are sensitive to details of the mean velocity profile near the wave surface where no accurate, reliable experimental data exist.

Hussain and Reynolds (1970) studied the behavior of a periodic disturbance in turbulent shear flow. They postulated that the induced turbulent Reynolds stresses are proportional to wave-induced strain rate through an eddy viscosity and that the eddy viscosity for the perturbed flow is the same as that for the undisturbed flow. The eddy viscosity expression across the turbulent boundary layer used in their computation was the one proposed by Reynolds and Tiederman (1967). The relative success of their eddy viscosity model over the quasilaminar model in predicting wave behavior demonstrates that the distortion of the background turbulent field by the wave is important and should not be ignored. Saeger and Reynolds (1971) studied the interaction of sinusoidal travelling waves with turbulent shear flow in a two dimensional channel flow with one mechanically articulated, waving wall. The turbulent closure assumptions for the wave perturbed momentum equations are same as those of Hussain and Reynolds, namely, the eddy viscosity model. The measured oscillating pressures were compared with predictions of

inviscid, quasilaminar and turbulent eddy viscosity models. They found the trends of pressure amplitude and phases are correctly predicted for upstream running waves by all three models. For downstream running waves the models begin to differ substantially, namely, neither the amplitude nor phase agree with the data. Also, the inviscid model predicts smaller values of power transfer than those predicted by the turbulent eddy viscosity model.

The eddy viscosity model implies that the effect of turbulent mixing is similar to the effect of molecular viscosity in that the stress is proportional to the velocity shear. The model also implies that the turbulent Reynolds stresses is a local phenomenon; its effect at each point is determined by the character of the mean flow at that point. Noting that the flux of momentum which the Reynolds stress represents is largely the result of mixing between regions where the mean flow differs, Prandtl (1945) suggested that the turbulent Reynolds stresses must be related to the energy of turbulent fluctuation. Long (1971) adapted the turbulent energy closure model of Bradshaw, Ferriss and Atwell (1967) to obtain similar closure relations for wave-induced fields. The results of his model were compared with the results of Miles inviscid theory and the experimental work of Dobson. The experimental results of Dobson agree better with predictions of Long's (1971) turbulent model than with Miles' inviscid theory. In some typical cases the computed growth rate differs from Dobson's experimental values by a factor no more than two. On the whole, the comparisons between experimental and theoretical growth rate spectra and pressure

phase angles showed better agreement at the lower wind speeds than at the higher wind speeds. It was also reported that the computation was very sensitive to the boundary condition of wave-induced turbulent energy at the air water interface.

The visco-elastic behavior of a turbulent fluid was added to the Bradshaw, Ferriss and Atwell (1967) scheme by Townsend (1972) to investigate the distortion of turbulent boundary layer flow due to surface waves running in different directions from the mean velocity field. The induced turbulent Reynolds stresses were characterized by elastic elongation and rotation of the mean turbulent Reynolds stresses. The calculated wave growth rates are considerably less than those measured by Snyder and Cox (1966), Barnett and Wilkerson (1967), and Dobson (1971).

Both the turbulent kinetic energy and eddy viscosity models were reconsidered by Davis (1972). He used a phenomenological closure of the conservation equation for turbulent Reynolds stresses to test two generalizations of the Bradshaw, Ferriss and Atwell (1967) model. In one all stresses are assumed to vary proportionally to mean turbulent energy; in the second only the normal stress variations are proportional to turbulent energy and the conservation equation of the induced horizontal shear is retained. The computed growth rate for the first generalization was an order of magnitude less than the experimental results of Kendall (1970) and Dobson(1971). The computed results for the second generalization were worse. Davis' work also made clear that the models are very sensitive to the mean velocity profile near the air-water interface. This

makes it difficult to draw any definite conclusions from comparisons with experiments since the mean velocity profile is unknown near the wave surface.

Norris and Reynolds (1975) studied the wave-induced pressure in a two dimensional channel flow with one mechanically-articulated waving wall. The pressure measurements were on the stationary wall opposite to the moving wavy wall. They solved a mathematical model of the problem in a transformed coordinate system so that the boundary conditions are applied exactly at the waving wall. They reported that their turbulent kinetic energy, eddy viscosity, and quasilaminar models produced about equally good pressure predictions; the use of the coordinate transformation seemed crucial in their study and the choice of Reynolds stress model is not important. They found distinctly better results with the transformed coordinate system (recall Benjamin (1959) and Miles (1959) also used similar curvilinear coordinates). Acharya and Reynolds (1975) used the same turbulent model as Norris and Reynolds (1975) to study the response of turbulent channel flow to imposed oscillations. Their major conclusion is that the dynamics of the turbulence must be considered in any prediction of unsteady turbulent flows and a Reynolds stress equation model must be used.

Besides the phenomenological turbulent models mentioned above, Davis (1974), working on the basis of several assumptions, used a non-phenomenological model to investigate the generation of Reynolds stresses by an infinitesimal perturbation of a turbulent shear flow. The general method is,in principle, capable of

producing a constitutive relation, but unfortunately putting his method into practice requires a detailed description of the undisturbed turbulent field which is considerably more comprehensive than anything that can be obtained from presently available experimental data.

The possible significance of the induced turbulent Reynolds stresses on the momentum transfer from wind to wave was pointed out both by Miles (1967) and Phillips (1966). Kendall (1970) experimentally studied the response of the turbulent flow structure to the perturbation imposed by a wavy wall. He indicated experimentally the strong modulation of turbulent structure due to progressive waves and the non-negligible energy transfer to the waves due to induced turbulent Reynolds stresses.

Yu, *et al.* (1973) attempted for the first time to measure the induced turbulent Reynolds stresses over a progressive water wave in the turbulent boundary layer. Because of the limited accuracy provided by analog techniques in data taking and analysis their results were only qualitative and unsatisfactory.

1.2 Objectives of the Study

The experimental program was carried out in the Stanford Wind, Water-Wave Research channel with the objective of studying the interactions between a turbulent shear flow of air and a progressive, sinusoidal water wave. Both the magnitude and phase of wave-induced velocities and turbulent Reynolds stresses across the turbulent boundary layer were obtained.

The specific objectives of this study are as follows:

a. To reveal the nature of both the magnitude and phase distributions of wave-induced velocities and turbulent Reynolds stresses across a turbulent boundary layer. With a newly acquired digital data-acquisition-reduction system, we hoped to obtain experimental data of greatly improved quality and valuable information to facilitate the development of improved closure models.

b. To evaluate the importance of turbulence-wave interactions in the formulation of wind-wave generation theory. Specifically, from the measured wave-induced velocities and turbulent Reynolds stresses, the importance of turbulence effect on the momentum transfer from wind to waves could be verified.

c. To clarify the different and contradicting conclusions reached by various investigators regarding the importance of the wave-induced turbulent Reynolds stresses in relationship to different techniques employed in their analyses.

1.3 Scope of the Study

This work is divided into five major parts:

a. In Chapter 2, we define two averaging operators which allow us to decompose the air flow into overall mean, wave-induced, and turbulent components, then to apply these operators to the momentum and continuity equations to obtain the equations governing the wave-induced quanti-

ties. The relation of the wave-induced turbulent Reynolds stresses to wind-wave generation theory is also examined.

b. In Chapter 3, the experimental facilities and instrumentation used to study the interaction between the turbulent shear flow and a mechanically-generated progressive, sinusoidal water wave are described. The data acquisition and reduction schemes are also described.

c. In Chapter 4, the experimental results concerning the amplitude and phase distributions of wave-induced velocities and turbulent Reynolds stresses across the turbulent boundary layer are presented. The importance of wave-induced turbulent Reynolds stresses on the momentum transfer from wind to wave is verified based on the experimental data.

d. In Chapter 5, the turbulent models of Norris and Reynolds (1975), as adapted for the present wave-turbulent boundary layer interaction problem, are described. Furthermore, the comparison between the results of model computations and the experimental data is presented.

e. In Chapter 6, we summarize our work and present the conclusions and recommendations.

2. THEORETICAL BACKGROUND

A periodic disturbance in a turbulent shear flow will introduce additional periodic velocities and pressure in the flowfield. In this study, we consider turbulent air flow and a mechanically-generated, single frequency, progressive water wave at the air water interface, as a coupled dynamic system. Our interest is to study the wave-induced motions in the turbulent shear flow. Two distinct averaging procedures are used, as defined by Hussain and Reynolds (1970), to sort out the statistical contribution of the periodic disturbance from the background turbulent fluctuations. The averaging procedures enable us to decompose the air flow into overall mean, wave-induced, and turbulent components. Application of these averaging procedures to the momentum and continuity equations yields the resulting equations governing the wave-induced quantities. The appearance of the wave-induced turbulent Reynolds stresses in the equation and their relation to the momentum transfer from wind to wave is also examined.

2.1 Decomposition and Averages

The instantaneous signal $f(x,t)$ in a turbulent air stream disturbed by a small amplitude progressive water wave can be decomposed into three different components (see Figure 2.1);

$$f(\underline{x},t) = \overline{f}(\underline{x}) + f'(\underline{x},t) + \tilde{f}(\underline{x},t) \qquad (2.1)$$

Here $\bar{f}(\underline{x})$ is the time-independent mean component, $\tilde{f}(\underline{x},t)$ is the wave-induced quantity, and $f'(\underline{x},t)$ is the background turbulence. In order to single out the wave-induced quantities, two averaging procedures are defined. The time average which yields the mean value of $f(\underline{x})$ is defined as

$$\bar{f}(\underline{x}) = \lim_{T \to \infty} \frac{1}{T} \int_0^T f(\underline{x},t)dt \tag{2.2}$$

The phase average is defined as an average of the signal at a particular phase of the wave. Mathematically this can be expressed as

$$\langle f(\underline{x},t) \rangle = \lim_{N \to \infty} \frac{1}{N} \sum_{n=0}^{N} f(x, t + n\tau)$$

where τ is the period of the wave-induced disturbance. The background turbulence is assumed to be random and to make no contribution to a phase average. Hence, the phase average of $f(\underline{x},t)$ contains only the mean and wave-induced parts, viz.,

$$\langle f(\underline{x},t) \rangle = \bar{f}(\underline{x}) + \tilde{f}(\underline{x},t) \tag{2.3}$$

The wave-induced part can be obtained by subtracting the mean quantity from the phase-averaged quantity; hence,

$$\tilde{f}(\underline{x},t) = \langle f(\underline{x},t) \rangle - \bar{f}(\underline{x}) \tag{2.3a}$$

The wave-induced quantity $\tilde{f}(\underline{x},t)$ describes the interaction between the turbulent shear flow and the progressive water wave.

The equations governing the wave-induced velocities $\tilde{u}_i$ and pressure $\tilde{p}$ are derived in the following section.

2.2 The Governing Equations

The equations governing the incompressible, constant property, two-dimensional turbulent boundary layer air flow in the wind-wave channel (as shown in Figure 3.1) are the continuity and momentum equations. The dimensionless form of the equations based on the free-stream velocity U_∞ and the channel half height D (air portion only) are

$$\frac{\partial u_i}{\partial x_i} = 0 \tag{2.4}$$

$$\frac{\partial u_i}{\partial t} + u_j \frac{\partial u_i}{\partial x_j} = - \frac{\partial p}{\partial x_i} + \frac{1}{Re} \frac{\partial^2 u_i}{\partial x_j \partial x_j} \tag{2.5}$$

where $Re = U_\infty D/\nu$ is the Reynolds number and ν is the kinematic viscosity. The velocity and pressure fields in the air can be decomposed into three components as

$$u_i = \bar{u}_i + \tilde{u}_i + u_i' \tag{2.6}$$

$$p = \bar{p} + \tilde{p} + p' \tag{2.7}$$

We substitute Equations (2.6) and (2.7) for u_i and p in Equations (2.4) and (2.5). Taking the phase average and time average of the resulting equations and subtracting the time-averaged

equations from the phase-averaged equations yields the equations governing the wave-induced quantities (Hussain and Reynolds 1970).

$$\frac{\partial \tilde{u}_i}{\partial x_i} = 0 \tag{2.8}$$

$$\frac{\partial \tilde{u}_i}{\partial t} + \bar{u}_j \frac{\partial \tilde{u}_i}{\partial x_j} + \tilde{u}_j \frac{\partial \bar{u}_i}{\partial x_j} = -\frac{\partial \tilde{p}}{\partial x_i} + \frac{1}{Re} \frac{\partial^2 \tilde{u}_i}{\partial x_j \partial x_j}$$

$$+ \frac{\partial}{\partial x_j} \left(\overline{\tilde{u}_i \tilde{u}_j} - \tilde{u}_i \tilde{u}_j \right) - \frac{\partial}{\partial x_j} \left(\langle u_i' u_j' \rangle - \overline{u_i' u_j'} \right) \tag{2.9}$$

In a small-amplitude, linear analysis the term

$$\frac{\partial}{\partial x_j} \left(\overline{\tilde{u}_i \tilde{u}_j} - \tilde{u}_i \tilde{u}_j \right)$$

is quadratic in the induced quantities and can be neglected. The term

$$\langle u_i' u_j' \rangle - \overline{u_i' u_j'} = \tilde{r}_{ij}$$

is the difference between the phase averaged and time averaged Reynolds stresses and represents the oscillating components of the turbulent Reynolds stresses caused by the passage of waves.

Having neglected the nonlinear term in Equation (2.9), we produced in Equations (2.8) and (2.9) a linear system in the induced quanties $\tilde{u}_i$ and $\tilde{p}$. The $\tilde{r}_{ij}$ terms are unknown; hence, a closure assumption must be made. Both inviscid and quasi-

laminar models solve the closure problem by assuming that the travelling waves do not influence the turbulent structure and, hence, that $\tilde{r}_{ij}$ is zero. Miles inviscid model neglects the viscous term $\frac{1}{Re} \frac{\partial^2 \tilde{u}_i}{\partial x_j \partial x_j}$, also.

To seek a closure condition for $\tilde{r}_{ij}$, one could derive an equation for $\tilde{r}_{ij}$ by employing the equations for the background turbulence (Hussain and Reynolds, 1970), namely,

$$\frac{\partial u_i'}{\partial t} + \bar{u}_j \frac{\partial u_i'}{\partial x_j} + \tilde{u}_j \frac{\partial u_i'}{\partial x_j} + u_j' \frac{\partial \bar{u}_i}{\partial x_j} + u_j' \frac{\partial \tilde{u}_i}{\partial x_j}$$

$$= - \frac{\partial p'}{\partial x_i} + \frac{1}{Re} \frac{\partial^2 u_i'}{\partial x_j \partial x_j} + \frac{\partial}{\partial x_j} (\langle u_i' u_j' \rangle - u_i' u_j') \qquad (2.10)$$

When the governing equation for $\tilde{r}_{ij}$ are derived, more unknowns appear in the equations. Consequently, the closure problem is pushed to even higher orders. We are forced, then, to resort to a semi-empirical turbulent closure models by relating $\tilde{r}_{ij}$ to the other perturbation quantities. The eddy viscosity model considers that the effect of the turbulent mixing is similar to the effect of viscosity in that $\tilde{r}_{ij}$ is proportional to the wave-induced velocity field through an eddy viscosity. For "higher order" turbulent energy closures (see Reynolds, 1970), one can employ an equation for the wave-induced turbulent kinetic energy $\tilde{q}^2 = \tilde{u}_i^2$ in conjunction with constitutive equations relating $\tilde{r}_{ij}$ to

$\tilde{q}^2$. The wave-induced turbulent kinetic energy equation can be derived through procedures similar to those used in obtaining the $\tilde{r}_{ij}$ equation. The eddy viscosity and turbulent energy closure models of Norris and Reynolds (1975) adapted for the present study are discussed in Chapter 5. Although the wave-induced equations are not closed, the role played by $\tilde{r}_{ij}$ in the momentum transfer from wind to wave can be examined (see the following section).

2.3 Momentum Transfer from Wind to Wave

The wave-induced turbulent Reynolds stress contribution to the momentum transfer from wind to wave was evaluated both by Phillips (1966) and Miles (1967). Phillips (1966, page 94) derived from the wave-induced momentum equation an expression for the mean rate at which momentum is transferred from wind to wave, say F per unit area, i.e.,

$$F = -\rho_a \overline{(\tilde{u}\tilde{v})}_\eta - \rho_a \left(\overline{\tilde{r}_{11} \frac{\partial \eta}{\partial x}} - \eta \overline{\frac{\partial \tilde{r}_{12}}{\partial y}} \right)_\eta \qquad (2.11)$$

where the subscript η indicates these quantities are evaluated at the air water interface and η is the displacement from the mean of a periodic, surface wave propagating in the horizontal x-direction. The wave-induced Reynolds stress $-\rho_a \overline{(\tilde{u}\tilde{v})}_\eta$ can be expressed in terms of wave-induced vorticity Ω as

$$-\rho_a \overline{(\tilde{u}\tilde{v})}_\eta = \rho_a \int_\eta^\infty \overline{\tilde{v}\Omega}\, dy \qquad (2.12)$$

where

$$\Omega = \frac{\partial \tilde{u}}{\partial y} - \frac{\partial \tilde{v}}{\partial x}$$

and can be related to $\tilde{r}_{ij}$ through the equation for the wave-induced vorticity (Phillips 1966, page 97)

$$(\bar{u}-c)\frac{\partial \Omega}{\partial x} + \frac{d^2\bar{u}}{dy^2}\tilde{v} = \frac{\partial}{\partial x}\frac{\partial}{\partial y}(\tilde{r}_{22} - \tilde{r}_{11}) + \left(\frac{\partial^2}{\partial x^2} - \frac{\partial^2}{\partial y^2}\right)\tilde{r}_{12} \qquad (2.13)$$

through use of the following procedures:

a. Substitute the travelling wave expressions ($\tilde{f} = |\tilde{f}|\, e^{i(Kx-\omega t+\theta_f)}$) for Ω, $\tilde{v}$ and $\tilde{r}_{ij}$ into Equation (2.13) and express Ω as a function of $\tilde{r}_{ij}$, $\tilde{v}$ and $\bar{u}$.

b. Substitute the result of a. into Equation (2.12).

c. After simplifying, express the wave-induced Reynolds stress as

$$-\rho_a\overline{(\tilde{u}\tilde{v})}_\eta = \pi\rho_a\left[\frac{-\frac{d^2\bar{u}}{dy^2}\bar{\tilde{v}}^2}{K\frac{d\bar{u}}{dy}}\right]_c + \rho_a\int_\eta^\infty \overline{\tilde{v}\omega}\,dy \qquad (2.14)$$

Here ρ_a is the air density, K is the wave number and the expression for $\overline{\tilde{v}\omega}$ in Equation (2.14) is

$$\overline{\tilde{v}\omega} = \frac{1}{(\bar{u}-C)K} \times$$

$$\left\{ -\frac{K^2 |\tilde{v}||\tilde{r}_{11}|}{2}\cos(\theta_2 - \theta_{12} + \frac{\pi}{2}) - \frac{|\tilde{v}|}{2}\frac{d^2|\tilde{r}_{12}|}{dy^2}\cos(\theta_2 - \theta_{12} + \frac{\pi}{2}) \right.$$

$$- |\tilde{v}|\frac{d|\tilde{r}_{12}|}{dy}\frac{d\theta_{12}}{dy}\cos(\theta_{12} - \theta_2) - \frac{|\tilde{r}_{12}||\tilde{v}|}{2}\frac{d^2\theta_{12}}{dy^2}\cos(\theta_{12} - \theta_2)$$

$$+ \frac{|\tilde{v}||\tilde{r}_{12}|}{2}\left(\frac{d\theta_{12}}{dy}\right)^2\cos(\theta_2 - \theta_{12} + \frac{\pi}{2}) - \frac{K|\tilde{v}|}{2}\frac{d|\tilde{r}_{12}|}{dy}\cos(\theta_2 - \theta_{11} + \pi)$$

$$- \frac{K}{2}|\tilde{v}|\frac{d|\tilde{r}_{12}|}{dy}\cos(\theta_{22} - \theta_2) - \frac{K}{2}|\tilde{v}||\tilde{r}_{11}|\frac{d\theta_{11}}{dy}\cos(\theta_2 - \theta_{11} + \frac{\pi}{2})$$

$$\left. + \frac{K}{2}|\tilde{v}||\tilde{r}_{22}|\frac{d\theta_{22}}{dy}\cos(\theta_2 - \theta_{22} + \frac{\pi}{2}) \right\} \qquad (2.15)$$

where θ_2 and θ_{ij} are the phase lags between $\tilde{v}$ and η and $\tilde{r}_{ij}$ and η, respectively. Let

$$F_c = \pi \rho_a \left[\frac{-\frac{d^2\bar{u}}{dy^2}\bar{\tilde{v}}^2}{K\frac{d\bar{u}}{dy}} \right]_c \qquad (2.16)$$

$$F_{w1} = \rho_a \int_{\eta}^{\infty} \overline{\tilde{v}\omega} dy \qquad (2.17)$$

and $$F_{w2} = -\rho_a \left(\overline{\tilde{r}_{11}} \overline{\frac{\partial \eta}{\partial x}} - \eta \overline{\frac{\partial \tilde{r}_{12}}{\partial y}}\right)_{\eta} \qquad (2.18)$$

Thus, equation (2.11) can be expressed as

$$F = F_c + F_{w1} + F_{w2}$$

The momentum transfer F_c given by (2.16) is the contribution evaluated at the critical height (where the mean velocity is equal to the wave celerity). The F_c transfer term is identical in form with that for Miles' inviscid model, but has the significant difference that $\tilde{v}$ (the wave induced air velocity in the veritical y direction) depends implicitly on $\tilde{r}_{ij}$. Equations (2.17) and (2.18) represent additional sources of mean momentum transfer to the wave. F_{w1} is the contribution due to $\tilde{r}_{ij}$ at all layers above the air-water interface except at the critical height. F_{w2} is the contribution due to $\tilde{r}_{ij}$ at the air-water interface.

Since $\tilde{r}_{11}$ and $\tilde{r}_{12}$ are sinusoidal functions of x, the travelling wave expressions $\tilde{r}_{11} = |\tilde{r}_{11}| \, e^{i(Kx-\omega t+\theta_{11})}$ and $\tilde{r}_{12} = |\tilde{r}_{12}| e^{i(Kx-\omega t+\theta_{12})}$ can be used in Equation 2.18. The resulting equation is

$$F_{w2}=-\rho_a\left[\frac{\left|\tilde{r}_{11}\right|\left|K\eta\right|}{2}\cos\left(\frac{\pi}{2}-\theta_{11}\right)-\frac{\left|\eta\right|}{2}\frac{d\left|\tilde{r}_{12}\right|}{dy}\cos\theta_{12}\right.$$

$$\left.-\frac{\left|\tilde{r}_{12}\right|\left|\eta\right|}{2}\frac{d\theta_{12}}{dy}\cos\left(\frac{\pi}{2}+\theta_{12}\right)\right]_{\eta} \qquad (2.19)$$

For the inviscid and quasilaminar models, the turbulence structure is assumed not to be affected by the wave and, thus, there are no wave-induced components of the turbulent Reynolds stresses. Therefore, both F_{w1} and F_{w2} are zero. The importance of $\tilde{r}_{ij}$ in the momentum transfer from wind to wave can be evaluated according to Equations (2.14), (2.15) and (2.19), by use of experimentally measured values of the wave-induced velocity and turbulent Reynolds stresses. The experimental program conducted to study the interaction between a turbulent shear flow and a progressive water wave is described in Chapter 3. The methods used to obtain both the magnitude and phase of wave-induced velocity and $\tilde{r}_{ij}$ are also discussed there.

3. EXPERIMENTAL METHODS AND DATA REDUCTION

In this chapter, the experimental facilities and instrumentation used in this study are described. The velocity and wave height signals were measured by hot film sensors and a capacitance wave height gauge, respectively. The hot film probe was mounted on a vertical traversing mechanism to allow measurement throughout the whole turbulent boundary layer. A wave following system was also used in this study to supply data in close proximity to the air-water interface. Data were processed and analyzed on a digital data acquisition and reduction system. The wave-induced perturbations in the turbulent air stream were singled out by using both cross correlation and cross spectrum techniques.

3.1 Experimental Facilities

3.1.1 Wind Wave Channel

The experiment was conducted in the Stanford Wind, Water-Wave Research Facility as shown in Figure 3.1. A detailed description of the facility was given in Hsu (1965). The overall length of the channel is approximately 40m. The test section is approximately 20m long, 1m wide, and 2m high. Water depth in the channel is variable. For this study the channel was filled with water to a 1m depth and the upper half of the channel served as the air flow section. A horizontal-displacement-type mechanical wave-generator capable of generating selected wave forms is located at the up-

stream end of the channel. In the present study, a sinusoidal signal of frequency 1 Hz from a function generator with a frequency resolution of $\pm$ 1% formed the input to the closed-loop servo-control system for the generation of a progressive wave with an amplitude of 2.54 cm. A basket consisting of stainless steel turnings is placed behind the wave plate to minimize wave reflection. A beach consisting of stainless steel turnings is placed at the downstream end of the channel for the same purpose. The wave reflection coefficient for waves at a frequency of 1 Hz was found to be about 5 percent (Bole and Hsu, 1967). Air flow is produced by drawing air through the test section with a suction fan at downstream end of the channel. A stainless steel honeycomb is placed before the fan to eliminate vortex motion of the air flow caused by circular motion of the fan. The air inlet is positioned approximately 4m downstream of the wave plate to allow full establishment of the mechanical waves prior to wind action. The air moves through fiberglass filters, a honeycomb and 3 wire mesh screens before entering into the test section. A flat, smooth aluminium plate approximately 2m long was installed at downstream of the air inlet to provide a smooth transition to the water surface. The cross-sectional distribution of air flow in the channel reported by Hsu (1965) indicates that flow is two dimentional for substantially the entire test section. The location of the measurement station was selected at approximately 13m from the end of the aluminum plate in front of the air inlet.

3.1.2 Probe Carriage and Traversing Mechanism

The probe carriage and traversing mechanism permit remote contral of probe location in the longitudinal, transverse, and vertical directions within the wind-wave facility. The resolution in measuring the vertical distances is 0.0254cm. Details of the motorized carriage and traversing mechanism are given by Chambers, et al (1970). A sketch of the probe carriage and support is shown in Figure 3.2. The fixed frame measurements were conducted with the velocity probes mounted on the traversing mechanism. Data were taken at [illegible] fixed heights between 3.2cm and 34cm above the mean water surface.

3.1.3 Wave-Following System

A wave following device was used to measure the instantaneous signals at a fixed distance above the oscillating water surface. The system consists of a motor that provides the driving force, an aluminium channel that supports a pulley and cable assembly, and a stainless steel tube (used to attach the sensors) that follows the wave. The bulk of the wave-follower was installed outside the wind wave channel and on top of an aluminium structure, as shown in Figure 3.3. Only the supporting aluminium channel extended into the channel. The electrical controls of the wave follower system include (i) a position potentiometer for recording elevation, (ii) an offset dial that controls the probe position relative to the water surface and (iii) and input dial

which provides meters/voltage scaling in according to the wave height gauge calibration. The electric and mechanical devices are coupled in the wave follower system through a negative feedback control system. This system is capable of a maximum oscillation of 12.7cm. The signal from the capacitance wave height gauge provides the input to the mechanical system, changes in water surface elevation creating an error voltage between the position potentiometer and the input of wave gauge. This error is amplified and used to correct the system location, thereby restoring correspondence between input and output signals. Details of the mechanical and electrical control systems were described by Yu, et al (1971, 1973). A tachometer was attached to the back end of the shaft of the motor to indicate its speed of rotation. The rotation speed of the motor corresponds directly to the oscillating velocity of the wave follower. A calibrated relationship of the voltage output from the tachometer and the oscillating velocity of the wave follower was used to subtract the wave-follower-induced velocity from the hot-film-sensed vertical velocity component signal. In this study, the calibrated result was 1 volt per 0.305 m/s. The phase lag of the wave follower feedback control system at wave frequency 1 Hz is 2^{o} (calibrated by cross correlating between wave and wave follower signals). The phase lag was compensated by placing the wave gauge wire 0.864cm (equivalent distance of 2^{o} phase angle for 1 Hz water wave) upstream from the other measuring probes. After compensation the wave follower

motion was in phase with the wave and the follower maintained at a selected distance from the water surface. The data obtained in the wave-following frame of reference were taken at 8 different heights between 1.02 cm and 5.33 cm above the instantaneous water surface.

3.2 Instruments

3.2.1 Hot Film Probe

The horizontal and vertical turbulent velocity components were measured using quartz-coated cross hot-film sensors of diameter 0.05 mm and length 1.016 mm. The hot films were operated in a constant temperature mode and driven by Thermo-Systems Inc. Model 1010 anemometers. The film acts as one leg of the bridge circuit. The effective cooling velocity (velocity normal to the hot film) causes the film resistance to change. The corresponding voltage output due to the resistance change is amplified and used as a feedback signal in maintaining the bridge balance. During the experiment, the films were operated at a sufficiently high over heat ratio (1.6) to minimize the possibility of temperature contamination of the velocity signals. The experimental correlation applicable to hot films is

$$E^2 = A + BU_{eff}^n$$

where E is the voltage drop across the wire, U_{eff} is the cooling velocity normal to the film, and A, B and n are constants obtained

by least square curve fit.

Calibration of the hot film sensors was made in the core flow region of the wind-wave channel, immediately before and after each run. The mean velocity measured by the hot-film was also cross-checked with that measured by a pitot-static probe, the difference between the two results being within 3 percent of the mean velocity. In order to accurately calculate the effective cooling velocity, the orientation of the hot films relative to the probe centerline were measured with an optical comparator and the angle between the probe axis and the mean flow direction was obtained by successive calibrations with the probe rotated 180^{o} about the probe axis. The angle between the hot film and probe centerline was found to be within $\pm$ 7^{o} from the nominal angle of 45^{o} for the hot films used in this study. The angle between the probe axis and the mean flow direction was found to be less than 3^{o} after a careful experimental setup. Figure 3.4 presents typical cross hot film calibration curves.

3.2.2 Pitot-Static Tube

A 0.317 cm o.d. United sensor pitot-static tube connected to Pace differential-pressure transducer (Model P90D, full range of $\pm$ 2.12 cm of water) and Sanborn Series 650 recorder (Model 656-1100 Carrier Amplifier) were used to calibrate the hot film probe and cross-check the mean velocity obtained from the hot film probe. The Pace differential-pressure transducer was calibrated with a Combust micromanometer with a resolution of

$\pm$ 0.006 cm of fluid of specific gravity 0.82. A typical calibration curve is shown in Figure 3.5.

3.2.3 Wave Height Gauge

A Nyclad-insulated copper conductor wire was used as the capacitance wave height gauge. Figure 3.6 is a sketch of the wave gauge; a detail report of the gauge was given by Colonell (1966). The wire is acting as one leg of a Sanborn 958-1100 capacitance bridge amplifier circuit. A change in water surface elevation causes a change in the capacitance of the wire. Before the calibration, the wire was presoaked for several hours to achieve a stable condition. Static calibration of the capacitance wire was achieved by attaching the wire to the probe traversing mechanism and systematically varying the submergence of the wire into still water in the channel. Accuracy of the wire was within $\pm$ 1 percent of the mean wave height. Figure 3.7 shows a typical calibration curve of the wave height gauge.

3.3 Data Acquisition and Reduction

3.3.1 Data Acquisition and Reduction System

The central unit of the data acquisition and reduction system is a HP 2100A computer with 32K of 16 bit core memory. An analog to digital converter system with a 16 channel multiplexer capable of a maximum sampling rate of 45000 samples per second was used to digitize the input signals in a simultaneous-sample-hold

mode. The load capacity of the analog-digital system is $\pm$ 10 volt with a 5 mv. resolution. A CRT terminal is used for the purpose of interrupting or interrogating the computer. Program input to the controller is accomplished through a high-speed paper tape reader. An IBM digital magnetic unit with compatible 9-track format and 800 characters per inch density was used for data recording. The signal to noise ratio is approximately 1000. An evaluation report of this system was given by Takeuchi and Mogel (1975).

3.3.2 Data Acquisition Procedures

The following were the steps for the data taking procedures:

a. Calibrate the wave height gauge.

b. Calibrate the hot film probe and cross-check the mean velocity readings obtained from both the pitot tube and the hot film probe.

c. Check the wave tank water level. A pointer located 2.54 cm below the probes was made to contact the still water surface, thus registering the initial probe position above the mean water surface.

d. Generate the mechanical wave of frequency 1 Hz and wave amplitude 2.54 cm. Blow the wind for about 30 minutes to achieve steady state in the channel. Set the probe as close to the wave crest as possible (avoiding submergence of the sensors).

e. D.C. bias and amplify the signals to within the maximum dynamic range of the computer (± 10 volts). The turbulent energy above 500 Hz was analyzed to be small. Therefore, the signals were also low pass filtered at 500 Hz with Rockland 1022F filters to avoid the high frequency noise introduced by the electrical instruments. Monitor both the hot film and wave height signals with an oscilloscope (Wave-follower-induced vertical velocity signal was also monitored during the wave-following-frame data taking).

f. Digitize the analog signals every 0.001 second for 5 minutes and store the data on the magnetic tape (consists of 600 data blocks; each block consists of 512 data points from each individual signal).

g. Change the position of the probe and repeat the data taking procedures from step e.

3.3.3 Data Reduction Procedures

The following steps were used for the data reduction procedures:

a. Use the HP 2100A computer and a FORTRAN program, which includes the calibration characteristics of sensors, to convert the digitized voltages to the physical quantities of horizontal velocity, veritical velocity and wave height (for the wave-following-frame data reduction, the induced vertical velocity caused by the motion of the probe was subtracted from the computed vertical velocity).

b. Calculate the mean quantities of data in Step a.

c. Subtract the results of b from those of a to get $\tilde{u} + u'$, $\tilde{v} + v'$ and η.

d. Do cross correlation or cross spectra between η and $\tilde{u} + u'$ and η and $\tilde{v} + v'$.

e. Do the computation of $(\tilde{u} + u') \times (\tilde{u} + u')$, $(\tilde{u} + u') \times (\tilde{v} + v')$ and $(\tilde{v} + v') \times (\tilde{v} + v')$.

f. Do cross correlation or cross spectra between η and the results of e.

g. Curve fit the results of d and f with a sinusoidal curve to get the magnitude and phase of wave-induced velocities and turbulent Reynolds stresses.

The cross correlation and cross spectrum techniques used for the data reduction in this study are discussed in Sections 3.3.4 and 3.3.5.

3.3.4 Cross-Correlation

Cross-correlation is a technique by which a signal of certain known frequency can be extracted from the total signal. The definition of cross-correlation is

$$R_{\eta f}(\tau) = \lim_{T \to \infty} \frac{1}{T} \int_0^T \eta(t)\ f(t-\tau)dt$$

Here $R_{\eta f}$ is the cross correlation function and τ is a known time delay. If η is a sinusoidal signal and f is a signal containing a sinusoidal component $\tilde{f}$ at the same frequency as η with a phase lag θ, $R_{\eta f}$ can be expressed as

$$R_{\eta f}(\tau) = \frac{|\eta||\tilde{f}|}{2} \cos(\omega\tau - \theta) \qquad (3.1)$$

where $\omega = 2\pi f$ is the radian frequency.

In practice the integration process is replaced by a summation, namely,

$$R_{\eta f}(\tau) = \frac{1}{N} \sum_{i=1}^{N} \eta(t_i) f(t_i - \tau)$$

where N is a large number. Typically, N-values of 120,000 were used in this study. Figure 2.1 illustrates the cross correlation.

The magnitude and phase lag of wave-induced component $\tilde{f}$ were obtained by a least square cosine curve fit of the cross correlation results with (3.1). Typical results of cross correlation fitted by a cosine curve for the wave-induced velocities $\tilde{u}$ and $\tilde{v}$ are shown in Figure 3.8a. The corresponding results for the induced turbulent Reynolds stresses are shown in Figure 3.8b.

3.3.5 Cross-Spectral Function and Coherence

The cross correlation and cross spectrum are a Fourier

Transform pair. In order to cross-check the results from correlation and to improve the calculation speed, cross spectrum calculation with the Fast Fourier Transform technique was used also in this study to obtain the magnitude and phase relation of wave-induced quantities relative to the wave. In general, the power spectral function $G_{\eta f}(n)$ is complex with real and imaginary parts representing in phase and 90^{o} - out of phase power respectively; thus,

$$G_{\eta f}(n) = C_{\eta f}(n) - i\, Q_{\eta f}(n)$$

where $C_{\eta f}$ is the co-spectra and $Q_{\eta f}$ is the quadrature spectra. The magnitude of the cross correlation function is

$$\frac{|\eta||\tilde{f}|}{2} = \left[C^{2}_{\eta f}(n) + Q^{2}_{\eta f}(n) \right]^{\frac{1}{2}}$$

The phase relation between η and $\tilde{f}$ is

$$\theta_{\eta f}(n) = \tan^{-1}\left[\frac{Q_{\eta f}(n)}{C_{\eta f}(n)} \right]$$

Figure 3.9 shows a typical amplitude versus f plot of $\tilde{r}_{11}$, $\tilde{r}_{12}$ and $\tilde{r}_{22}$ calculated by this technique and using the measured signals of turbulent Reynolds stresses and the waves. The resolution of the spectra is 0.098 Hz. The results show that the magni-

tudes at higher harmonics of the wave frequency are considerably smaller than that at the generated wave frequency. The coherence between two signals is defined as

$$\text{Coherence} = \frac{\left| G_{\eta f}(n) \right|^2}{G_{\eta}(n) \times G_{f}(n)}$$

where G_{η} and G_{f} are the auto spectral functions of η and f respectively. The coherence gives information on how two signals correlate with each other. FIgure 3.10 is the coherence spectrum of $\tilde{r}_{22}$ with the wave. The results show strong coherence at harmonics of the wave frequency. Similar features were observed in the coherence spectra of $\tilde{r}_{11}$ and $\tilde{r}_{12}$ with the wave.

4. EXPERIMENTAL RESULTS AND MOMENTUM TRANSFER FROM WIND TO WAVE

In this chapter, the experimental results of the interaction between the 1 Hz sinusoidal progressive water wave and the turbulent shear flow are presented. The magnitude and phase of wave-induced velocity and turbulent Reynolds stresses are calculated both in the fixed and wave-following frames of reference.

The contribution of $\tilde{r}_{ij}$ to the momentum transfer from wind to wave as described in section 2.3 is distributed through the turbulent boundary layer above the air-water interface. To verify the importance of $\tilde{r}_{ij}$ in the momentum transfer from wind to wave, we need the wave-induced velocities and turbulent Reynolds stresses across the whole turbulent boundary layer. Recall that the fixed probe measurements were conducted to obtain the data at 20 fixed heights between 3.2 cm and 34 cm above the mean water surface. The data obtained in the wave-following mode was extended to the region as close to the wave surface as possible without damaging the sensor, covering the region from 1.02 cm and 5.33 cm above the wave surface. The comparison between the results of calculation of F_{w1} by using the fixed frame data alone and then using both the fixed and wave-following frame data shows the importance of $\tilde{r}_{ij}$ close to the air water interface. F_{w2} was evaluated with the wave-following frame data.

PRECEDING PAGE BLANK-NOT FILMED

4.1 Mean Velocity and Turbulence Intensities

Mean velocities over the progressive water wave as a function of height above the mean water surface are shown in Figure 4.1 for 5 different free stream velocities as tabulated in Table 4.1 These mean velocity profiles were used for the model computation as described in Chapter 5. The comparison between the results measured with pitot-static tube and hot-film probe is also shown in the same figure (for the case U_∞ = 1.87 m/sec). The difference is within 3% of the free stream velocity. The comparison assures the accuracy and reliability of the hot film data-taking and reduction procedures.

Table 4.1

Free Stream Velocity Conditions

$\frac{U_\infty}{C}$	Critical height above the mean water surface
0.883	∞ (Non-critical layer case)
1.115	12.34 cm (Thick critical layer case)
1.34	8.57 cm (Thick critical layer case)
1.836	cannot be reached by probe (Thin critical layer case)
2.283	cannot be reached by probe (Thin critical layer case)

As shown in Figure 4.1 the mean velocity profiles deviate from the logarithmic law in the lower portion of the turbulent boundary layer compared with the conventional profile over a

rigid flat surface. It seems reasonable to conclude that the departure from the logarithmic law may be attributed to the differences in the boundary conditions between a deformable air-water interface with wave motions and a rigid immobile surface. It has been discussed previously that the numerical calculations based on various adhoc, closure assumptions are extremely sensitive to the velocity distribution and the turbulence characteristics near the interface. This indicates that detailed experimental data of the flowfield in close proximity of the air-water interface should be valuable for further improvement of wind-wave generation theory.

Typical normalized distributions of turbulence intensities and Reynolds stress as a function of non-dimensional heights measured in wave-following and fixed frames of reference are shown in Figures (4.2a) and (4.2b), respectively. The distributions of the turbulence quantities in Figure 4.2a are presented as a function of non-dimensional heights Kh_f over the progressive water wave, where K is the wave number and h_f is the height above the instantaneous wavy surface. The magnitudes of the relative turbulence intensities $\overline{u^2}/U_\infty^2$ and $\overline{v^2}/U_\infty^2$ and of the turbulent Reynolds stress $-\overline{uv}/U_\infty^2$ are consistent with those obtained in a turbulent boundary layer over a rigid flat surface (Klebanoff, 1954). The distributions of the turbulence quantities measured in a fixed frame of reference as shown in Figure 4.2b are plotted

as a function of non-dimensional height above the mean water surface. The relative magnitude of the u-component in the fixed coordinates is larger than that in the wave-following coordinate whereas the relative magnitudes of the $\overline{v^2}$ and $-\overline{uv}$ components are smaller. Plausible reasons responsible for the differences in magnitude measured in different frame of references are offered as follows: First, if the mean velocity profile is assumed to follow the undulating wavy surface for a small amplitude wave, the fixed probe would sample different portions of the local mean velocity. Thus, the differences in the local mean velocities consistent with the propagating wave height are included as turbulence quantities. Second, since the magnitudes of both the $\overline{v^2}$ and $-\overline{uv}$ components decrease with height, the fixed probe samples relatively larger portion of the turbulent boundary layer at greater height from the interface (except near the wave crest region) than that of the wave-following probe and thus, gives smaller values of $\overline{v^2}$ of $-\overline{uv}$ components.

4.2 Wave-Induced Velocities and Turbulent Reynolds Stresses

4.2.1 Fixed Probe Measurements

Figures 4.3 through 4.12 show the magnitudes and phase lags of wave-induced velocity components $\tilde{u}$ and $\tilde{v}$ as a function of non-dimensional height Kh above the mean water surface for five different mean free-stream velocities. As shown in Figure 4.5 through 4.10 the wave-induced velocities obtained by

the correlation and cross spectrum techniques are in good agreement. Since the Fast Fourier Transform subroutine of the cross spectrum technique is four times faster than the correlation technique, the cross spectrum technique was adopted for most of the computation in this study.

When U_∞/C is equal to 0.883, there is no critical height in the flowfield. As shown in Figure 4.4, the phase lags of $\tilde{u}$ and $\tilde{v}$ are close to 180^o and 270^o respectively; the phase variations of $\tilde{u}$ and $\tilde{v}$ across the turbulent boundary layer are small. $U_\infty/C = 1.115$ corresponds to the case when the critical height is at 12.38 cm above the mean water surface. As shown in Figure 4.6, there is a 170^o phase shift of $\tilde{u}$ near the critical height. As a guide for the experimental phase lag data of $\tilde{u}$ and $\tilde{v}$ in the region close to the air water interface, the theoretical phase lags of $\tilde{u}$ and $\tilde{v}$ at the mean water surface were obtained from the kinematic boundary conditions for a small amplitude wave as follows. The kinematic boundary conditions at the air-water interface are

$$u\big|_{y=\eta} = u_d + CK\eta + O(\eta^2) = u\big|_{y=0} + \frac{\partial u}{\partial y}\Big|_{y=0} \eta + O(\eta^2) \qquad (4.1)$$

$$v\big|_{y=\eta} = \frac{\partial \eta}{\partial t} + u\frac{\partial \eta}{\partial x} + O(\eta^2) = v\big|_{y=0} + \frac{\partial v}{\partial y}\Big|_{y=0} \eta + O(\eta^2) \qquad (4.2)$$

Here u_d is the drift velocity at the air-water interface, and the velocities at the air-water interface are expressed in terms of the velocities at the mean water surface by using the Taylor series expansion. Using the decomposition of Equation (2.1),

phase averaging Equations (4.1) and (4.2), time averaging Equations (4.1) and (4.2) and subtracting the time averaged quantities from the phase averaged quantities result in

$$\tilde{u}\Big|_{y=0} = -\frac{d\bar{u}}{dy}\Big|_{y=0}\eta + CK\eta \tag{4.3}$$

$$\tilde{v}\Big|_{y=0} = \frac{\partial\eta}{\partial t} + \bar{u}\Big|_{y=0}\frac{\partial\eta}{\partial x} \tag{4.4}$$

With the travelling wave expression $\eta = |\eta|\cos(Kx-\omega t)$ substituted into Equations (4.3) and (4.4) we have

$$\tilde{u}\Big|_{y=0} = \left(\frac{d\bar{u}}{dy} - CK\right)\Big|_{y=0}|\eta|\cos(Kx-\omega t + 180^{o}) \tag{4.5}$$

$$\tilde{v}\Big|_{y=0} = (\omega - K\bar{u})\Big|_{y=0}|\eta|\cos(Kx-\omega t + 270^{o}) \tag{4.6}$$

In this study $\omega = 2\pi$ (frequency = 1 Hz) and $K = 2\pi/C$; thus, Equations (4.5) and (4.6) can be expressed as

$$\tilde{u}\Big|_{y=0} = \left(\frac{d\bar{u}}{dy} - 2\pi\right)\Big|_{y=0}|\eta|\cos(Kx-\omega t + 180^{o}) \tag{4.7}$$

$$\tilde{v}\Big|_{y=0} = 2\pi\left(1 - \frac{\bar{u}}{C}\right)\Big|_{y=0}|\eta|\cos(Kx-\omega t + 270^{o}) \tag{4.8}$$

Based on Equations (4.7) and (4.8), the phase lag of $\tilde{u}$ is 180^{o} when $\frac{d\bar{u}}{dy}\Big|_{y=0} > 2\pi$ and is 0^{o} when $\frac{d\bar{u}}{dy}\Big|_{y=0} < 2\pi$, while the phase lag of $\tilde{v}$ is 270^{o} when $\bar{u}\Big|_{y=0} < C$ and is 90^{o} when $\bar{u}\Big|_{y=0} > C$.

The measured phase lags of $\tilde{u}$ and $\tilde{v}$ at the lowest height of measurement (3.18 cm above the mean water surface) were compared with the results obtained from Equations (4.7) and (4.8) as shown in Table 4.2. In this experiment, $\frac{d\bar{u}}{dy} > 2\pi$ at the lowest measurement point for all the experimental runs (based on the measured mean velocities at the lowest two measurement points above the mean water surface). Experimental data also show that $\bar{u} < C$ for the cases of $U_\infty/C = 0.883$, $U_\infty/C = 1.115$ and $U_\infty/C = 3.4$, while $\bar{u} > C$ for the cases of $U_\infty/C = 2.28$, at the lowest measurement point.

Table 4.2

Comparison of Estimated and Measured (Fixed Probe Data) Phase Lags of $\tilde{u}$ and $\tilde{v}$ at the Lowest Measurement Point

U_∞ (m/sec)	U_∞/C	$\tilde{u}_\theta(\theta_1)$ (Equation 4.7)	$\tilde{u}_\theta(\theta_1)$ (Measured)	$\tilde{v}_\theta(\theta_2)$ (Equation 4.8)	$\tilde{v}_\theta$ (Measured)
1.381	0.883	180^o	184.24^o	270^o	273.77^o
1.744	1.115	180^o	187.2^o	270^o	277.99^o
2.096	1.34	180^o	166.76^o	270^o	273.46^o
2.872	1.84	180^o	130.79^o	90^o	24.45^o
3.571	2.28	180^o	128.68^o	90^o	54.41^o

As shown in Table 4.2, the discrepancy between the experimental results and the results obtained from Equations (4.7) and (4.8) increased as the wind velocity increased. A plausible reason for the consistent deviations could be that when the wind velocity is increased the shear velocity is increased, therefore the lowest measurement point in y^+ coordinates is raised until Equations (4.7) and (4.8) are no longer valid.

As shown in Figures 4.3, 4.5, 4.7, 4.9 and 4.11 the magnitude of $\tilde{u}$ is much larger than that of $\tilde{v}$ close to the air-water interface and the magnitude difference between $\tilde{u}$ and $\tilde{v}$ decreases as distance increases from the interface. This may be due to the fact that the fixed probe traversed different portions of the local mean velocity profile and the magnitude of $\tilde{u}$ is also contributed by the velocity gradient of the portion of the local mean velocity profile traversed by the sensor; therefore, as the mean velocity gradient is decreasing with Kh so does the magnitude difference between $\tilde{u}$ and $\tilde{v}$. As shown in Figure 4.7, the measured magnitude of $\tilde{u}$ is decreasing with Kh, while the magnitude of $\tilde{v}$ is increasing with Kh near the interface. The reason could be due to the fact that the magnitude of $\tilde{v}$ is a function of both the decay factor e^{-Kh} and the difference between the local mean velocity and wave celerity $(\bar{u} - C)$ (See Phillips 1966).

The measured values of the amplitude and phase of $\tilde{r}_{11}$, $\tilde{r}_{12}$ and $\tilde{r}_{22}$ as a function of non-dimensional height above the mean water surface are shown in Figures 4.13 through 4.22. As shown in Figures 4.13 (a, b, c), 4.15 (a, b, c), 4.17, 4.19 and 4.21 (a, b, c), the magnitude of $|\tilde{r}_{11}|$ is an order of magnitude larger than those of $|\tilde{r}_{12}|$ and $|\tilde{r}_{22}|$ and the magnitude of $|\tilde{r}_{22}|$ is the smallest close to the air-water interface. The distributions of $|\tilde{r}_{11}|$ across the turbulent boundary layer have the same decreasing trend as a function of Kh for all cases, i.e., non-critical layer, Figure 4.13a; thin critical layer, Figures 4.19 and 4.21a; and thick critical layer, Figures 4.15a and 4.17.

The magnitude and phase angle relations between the different $\tilde{r}_{ij}$ components at the air-water interface may be estimated as follows. By assuming that the streamline follows the wavy surface, i.e., that

$$\frac{\partial \eta}{\partial x} = \frac{v}{(u-C)} = \frac{(\bar{v} + \tilde{v} + v')}{(\bar{u} - C + \tilde{u} + u')}$$

or $$\bar{v} + \tilde{v} + v' = (\bar{u} - C + \tilde{u} + u') \frac{\partial \eta}{\partial x} \qquad (4.9)$$

we have a basic boundary condition. Now,

a. Multiply Equation (4.9) by v'.

b. Phase average the results of a.

c. Time average the results of a.

d. Subtract the result of c from that of b to obtain

$$|\tilde{r}_{22}| = \frac{2\pi|\eta|}{\lambda} |\tilde{r}_{12}|$$

and $$\theta_{22} = 90^{o} + \theta_{12} \qquad (4.10)$$

In this study $|\eta|$ = 2.54 cm and λ = 1.56 m; therefore,

$$|\tilde{r}_{22}| = 0.102 \; |\tilde{r}_{12}| \qquad (4.11)$$

e. Multiply Equation (4.9) by u'.

f. Phase average the result of e.

g. Time average the result of e.

h. Subtract the result of g from that of f to obtain

$$\theta_{12} = 90^{o} + \theta_{11} \qquad (4.12)$$

and $|\tilde{r}_{12}| = 0.102\ |\tilde{r}_{11}|$ (4.13)

The experimental results for $|\tilde{r}_{ij}|$ at the lowest measurement point as tabulated in Appendix II indicate comparable order of magnitude among the three components of $|\tilde{r}_{ij}|$ for experimental and theoretical estimates, particularly for the high wind-speed cases, $U_\infty/C = 1.34$, 1.84 and 2.23.

However, the experimentally measured phase lags of the $\tilde{r}_{ij}$ at the lowest measurement point disagree with the theoretical estimates given by Equations (4.10) and (4.12). The inconsistancy could be due to a sharp gradient of the phase angle close to the water surface, so that the measured data at the lowest measurement point does not represent the actual phase angle at the air-water interface.

4.2.2 Wave-Following Measurements

Figures 4.23 and 4.24 show the magnitudes and phase-lags of wave-induced velocity components $\tilde{u}$ and $\tilde{v}$ as a function of non-dimensional height Kh_f above the instantaneous wave surface for five different mean free-stream velocities. To establish the validity of the experimental data, the experimental results of $\tilde{v}$ at the lowest measurement point (h_f=1.143 cm) were compared with the estimate of $\tilde{v}$ obtained through the kinematic boundary condition on the wave surface.

Considering a sinusoidal wave $\eta = |\eta| \cos \omega t$, we find that the kinematic boundary condition for $\tilde{v}$ at the wave surface is

$$\tilde{v} = \frac{\partial \eta}{\partial t} = -\omega|\eta|\sin\omega t = \omega|\eta|\cos(\omega t - 270^{o})$$

The theoretical phase lag of $\tilde{v}$ is 270^{o} and the magnitude of $\tilde{v}$ is $\omega|\eta|$ at the wave surface. In this study, the wave amplitude is 2.54 cm and the wave frequency f is 1 Hz. Therefore, the theoretical value of $|\tilde{v}|$ is 16.0 cm/sec at the wave surface. The measured magnitude and phase of $\tilde{v}$ at the lowest measurement point is tabulated in Table 4.3 for comparison with the theoretical estimate of $\tilde{v}$ at the wave surface.

Table 4.3

Measured Values (Wave-Following Data) of Wave-Induced Vertical Velocity at the Lowest Measurement Point

U_{∞}/C	$(y^{+})_{min}$	$\lvert\tilde{v}\rvert$	$\tilde{v}_{\theta}$
1.11	55.9	13.045	268.97^{o}
1.34	72.9	10.394	271.46^{o}
1.49	89.1	8.352	276.38^{o}
1.84	128.0	5.09	291.77^{o}
2.28	164.0	2.652	303.99^{o}

Although the distance above the instantaneous wavy surface is closely the same for all free stream velocities, the relative position of the probe is farther away from the surface in y^+- coordinates at high wind speeds because of the increase in u*. In other words, the probe was not able to measure the "true" wave-induced quantities at high wind speeds. It can be seen from Table 4.3 that the discrepancy between the experimental results and the theoretical estimates increased as the wind velocity increased.

As shown in Figure 4.23, the magnitude of $\tilde{u}$ decreases with Kh_f for all wind speeds. However, $|\tilde{v}|$ decreases with Kh_f for the low wind cases (U_∞/C = 1.11, 1.34, and 1.49) and increases for the high wind cases (U_∞/C = 1.84 and 2.28). The differences in $|\tilde{v}|$ variation with respect to Kh_f observed for the high and low wind speeds may be due to the fact that $|\tilde{v}|$ is dependent on both the disturbance decay rate in the vertical direction and the local value of $(\bar{u} - C)$. As shown in Figure 4.24, the measured phase angles of $\tilde{v}$ are close to the theoretical boundary condition value of 270^o phase lag.

In order to show the differences in magnitude of the measured $\tilde{u}$ and $\tilde{v}$ components in both the fixed and wave-following frames of reference, the $|\tilde{u}|$ and $|\tilde{v}|$ at the lowest measuring position as well as at a fixed non-dimensional height, $Kh = Kh_f = 0.22$ were tabulated in Table 4.4.

Table 4.4

Comparison of $\tilde{u}$ and $\tilde{v}$ Data Both in the Fixed and Wave Following Frames

U_∞/C	1.11		1.34		1.84		2.28	
Measured Point 10^2	$\frac{\lvert\tilde{u}\rvert}{U_\infty}$	$\frac{\lvert\tilde{v}\rvert}{U_\infty}$	$\frac{\lvert\tilde{u}\rvert}{U_\infty}$	$\frac{\lvert\tilde{v}\rvert}{U_\infty}$	$\frac{\lvert\tilde{u}\rvert}{U_\infty}$	$\frac{\lvert\tilde{v}\rvert}{U_\infty}$	$\frac{\lvert\tilde{u}\rvert}{U_\infty}$	$\frac{\lvert\tilde{v}\rvert}{U_\infty}$
F (Lowest Point)	7.03	0.58	6.45	0.23	3.53	0.82	2.77	1.1
W-F (Lowest Point)	5.04	7.43	3.95	5.11	8.31	1.68	7.0	0.54
F ($Kh = 0.22$)	3.96	0.44	4.78	0.23	0.86	0.82	1.23	1.1
W-F ($Kh_f = 0.22$)	2.17	6.65	1.61	4.10	4.68	2.68	5.67	0.79

As discussed in Section 4.2.1, assuming that the mean velocity profile oscillates vertically with the surface wave motion means that the fixed probe measures different portions of the locan mean velotity profile associated with wave-following coordinates. Consequently, the difference in the local mean velocity which is a function of the wave amplitude and the mean velocity gradient, is included in the measured $|\tilde{u}|$ - component. Since the velocity gradient in the region of the fixed-probe decreases as the wind speed increases, there is less magnitude difference between moving and fixed frame values at high wind speeds than at the low wind speeds.

On the other hand, there is less magnitude difference between $|\tilde{u}|$ and $|\tilde{v}|$ in the wave-following measurements except at high wind speed, $U_\infty/C = 2.23$. The large difference between $|\tilde{u}|$ and $|\tilde{v}|$ at high wind speed may suggest "flow separation" where the mean velocity profile ceased to follow the surface wave motion as assumed.

Figures 4.25 and 4.27 show the magnitude of $\tilde{r}_{ij}$ as a function of Kh_f above the instantaneous water surface for five different free stream velocities. For the high wind cases ($\frac{U_\infty}{C} = 1.84$ and 2.28) $|\tilde{r}_{11}|$ is larger than $|\tilde{r}_{12}|$ and $|\tilde{r}_{22}|$. For the low wind cases, the orders of magnitude among $|\tilde{r}_{11}|$, $|\tilde{r}_{12}|$ and $|\tilde{r}_{22}|$ are the same. In Figure 4.25 the decay rate of $|\tilde{r}_{11}|$ as a function of Kh_f is more rapid for the high wind cases than it is for the low wind cases, while the opposite is observed for $|\tilde{r}_{22}|$ in Figure 4.26. In Figure 4.27, similar trends for $|\tilde{r}_{12}|$ as a function of Kh_f are observed for different wind velocities. Figure 4.28 shows the phase lags for $\tilde{r}_{11}$, $\tilde{r}_{12}$ and $\tilde{r}_{22}$. The phase lags or $\tilde{r}_{ij}$ were found not sensitive to different free-stream velocities, and the variation of the phase lags of $\tilde{r}_{ij}$ in the region measured was small.

4.3 Momentum Transfer from Wind to Wave

Kendall (1970) studied the structure of turbulent flow over a progressive wavy-wall. Because he did not make detailed measurements of the distribution $\tilde{r}_{ij}$ (both in magnitude and phase) throughout the turbulent boundary layer, the turbulence contributions of the momentum transfer from wind to waves could not be evaluated. However, based on his qualitative estimation he stated that the induced-turbulent Reynolds stresses are probably important in the momentum transfer from wind to waves.

From the measured mean velocity profile, wave-induced velocities, and turbulent Reynolds stresses described in the previous sections, the turbulent contribution to the momentum transfer from the wind to wave can be evaluated through the expressions in Equations (2.16) to (2.18) in Section 2.3 For example, from the experimental data taken at the lowest measuring point to the interface, the wave-induced Reynolds stress at the interface, $-\overline{\rho_a(\tilde{u}\tilde{v})}_\eta$ can be estimated and may be expressed as

$$-\overline{\rho_a(\tilde{u}\tilde{v})} = \frac{|\tilde{u}||\tilde{v}|}{2}\cos(\omega t + \theta)$$

where θ is the phase relation between $\tilde{u}$ and $\tilde{v}$. The results of F_c, F_{w1}, F_{w2} and $-\overline{\rho_a(\tilde{u}\tilde{v})}_\eta$ are tabulated in Table 4.5 for 5 different free-stream conditions.

Table 4.5

Experimental Results of Momentum Transfer from Wind to Waves

U_∞/C	y_c	F_c (N/m^2)	F_{w1} (N/m^2)	F_{w2} (N/m^2)	$-\rho_a \overline{\tilde{u}\tilde{v}}_{r_1}$
1.11	12.34	0.13×10^{-6}	0.35×10^{-6}	0.21×10^{-4}	0.20×10^{-4}
1.34	8.57	0.59×10^{-5}	0.48×10^{-5}	0.19×10^{-4}	0.18×10^{-4}
1.49	*	*	0.43×10^{-6}	0.10×10^{-4}	0.12×10^{-4}
1.84	*	*	0.11×10^{-6}	0.50×10^{-5}	0.51×10^{-5}
2.28	*	*	0.68×10^{-7}	0.49×10^{-5}	0.98×10^{-5}

* Cannot be measured or evaluated.

For large values of U_∞/C (1.49, 1.84 and 2.28), the critical height is so close to the air-water interface that the critical layer becomes inaccessible to the velocity probe. Thus, due to the lack of experimental data for $\frac{d^2\bar{u}}{dy^2}$, $\frac{d\bar{u}}{dy}$ and $\overline{\tilde{v}^2}$ at the critical height, F_c cannot be evaluated. For the cases of U_∞/C = 1.11 and 1.34, the values of $\frac{d^2\bar{u}}{dy^2}$ and $\frac{d\bar{u}}{dy}$ at the critical heights were evaluated from the best fit of a logarithmic profile to the measured mean velocity data. F_{w1} is the contribution due to $\tilde{r}_{ij}$ at all layers above the

critical height. The integral of Equation (2.17) was evaluated from 1.02 cm to 3.2 cm from the wave follower measured data and from 3.2 cm to 34 cm from the fixed probe measured data. (Due to lack of fixed frame data at $U_\infty/C = 1.49$, in this case F_{wl} was evaluated with the wave-follower measured data alone.) In order to evaluate the importance of the wave-induced turbulent Reynolds stresses in the region close to the air-water interface, F_{wl} was also evaluated by using the fixed-frame data only and the results are shown in Table 4.6.

Table 4.6

Experimental Results of F_{wl} (Fixed Probe Data)

U_∞/C	1.11	1.34	1.84	2.28
F_{wl}	0.21×10^{-7}	0.22×10^{-7}	0.18×10^{-7}	0.19×10^{-7}

The results of F_{wl} in Table 4.6 are small compared with those tabulated in Table 4.5. One may conclude, then, the importance of r_{ij} close to the air water interface.

As indicated in Equation (2.14), the sum of F_c and F_{wl} is equal to the wave-induced Reynolds stress at the air-water interface. As shown in Table 4.5 when U_∞/C is equal to 1.11 and 1.34 (cases when F_c can be evaluated experimentally), the sum of F_c and F_{wl} is smaller than the wave-induced Reynolds stresses,

$-\rho_a\overline{(\tilde{u}\tilde{v})}_\eta$ near the air-water interface. The difference may be attributed to the lack of experimental data in the immediate vicinity of the air-water interface where the integral of F_{w1} needs to be evaluated.

Since the lowest position of measurement above the instantaneous wavy surface in the wave-following system is the same for all free stream velocities, the probe is relatively farther away from the surface in y^+ coordinates due to the increase in u* with wind speed. In other words, the probe was not able to measure wave-induced quantities close to the air-water interface at high wind speed. Thus, whether the decrease in F_{w2} and $-\rho_a\overline{(\tilde{u}\tilde{v})}_\eta$ as the wind velocity increases as shown in Table 4.5 is due to less momentum transfer from wind to wave is uncertain. Note that F_{w2} has the same order of magnitude as $-\rho_a\overline{(\tilde{u}\tilde{v})}_\eta$, implying that a significant contribution to the total momentum transfer is derived from the wave-turbulence interaction. Clearly $\tilde{r}_{ij}$ cannot be neglected in the evaluation of the momentum transfer from wind to waves, their contribution as shown in Table 4.5 (U_∞/C = 1.11 and 1.34) comprising about 90 percent of the total transfer, while the critical layer contribution is about 10 percent.

5. THEORETICAL MODELING

Both Saeger and Reynolds (1971) and Norris and Reynolds (1975) studied the wave-induced pressure in a turbulent channel flow with a mechanically-articulated waving wall. In their theoretical modeling, they used different techniques to satisfy the time dependent boundary conditions at the wavy wall. Saeger and Reynolds solved the problem by transformation of the boundary conditions to the undisturbed and mean position of the moving wall using a Taylor-series expansion. Norris and Reynolds solved the problem by transformation of the entire problem to a time dependent coordinate system. In the transformed coordinate system, both walls are stationary and in particular the boundary condition can be applied exactly at the moving wall.

Norris and Reynolds (1975) calculated the wave-induced quantities by using quasilaminar, eddy viscosity, and turbulent energy closure models. By comparing their experimental and calculated results of wave-induced pressure on the stationary wall opposite the oscillating wavy wall, they concluded:

(1) The coordinate transformation approach is better than the boundary condition transfer approach. Since for turbulent shear flow the velocity curvature is large near the boundary, neglecting higher-order terms in the Taylor-series expansion introduces errors.

(2) The computational results in the transformed coordinate system checked well with the measured stationary wall pressure data

for upstream running waves and for downstream running waves in the range $0 \leq C/U_\infty \leq 0.4$. The eddy viscosity model results are slightly better than the turbulent kinetic energy model results compared with the measured pressure data.

(3) Although the calculated wave-induced pressure is quite insensitive to the wave-induced turbulent Reynolds stresses modeling used, differences in the calculated wave-induced velocities are noticed with different turbulent models. Thus, the velocity calculations are more sensitive to the assumed models than the pressure computations.

Both Benjamin (1959) and Norris and Reynolds (1975) solved the wave-induced field in a curvilinear coordinate system so that the boundary condition can apply at the wavy surface. Benjamin examined the effect of neglecting viscosity in the inviscid model. The results of his study indicated that the viscous effect is negligible while for the closure model $\tilde{r}_{ij}$ may be important. This result is inconsistant with the Norris and Reynolds' conclusions.

Norris and Reynolds compared their stationary wall pressure data with a simple inviscid analysis. Although the magnitude of the pressure appears to be inertially dominated for all wave speeds (upstream and downstream running waves), the phase shifts appear to deviate from such a simple inviscid analysis for downstream running waves, suggesting that important effects arise from viscous and turbulent influences. Inertia dominance appeared also in their laminar flow results. In other words, the stationary wall pres-

sure data cannot be used as a conclusive test of the need for a quality of turbulence modeling. Unfortunately, no experimental data on the velocity field were taken in their study. Therefore, the present experimental data on induced velocities and $\tilde{r}_{ij}$ directly over the progressive water wave can serve as a more sensitive test of their closure models. The objective of the modeling calculation in this study is to determine if either the coordinate transformation or the $\tilde{r}_{ij}$ terms are important in the wave-turbulence interaction problem.

In this chapter, the coordinate transform, the eddy viscosity model, and the turbulent energy model of Norris and Reynolds are described. In addition, the mean velocity profile, the eddy viscosity and the mean turbulent kinetic energy across the turbulent boundary layer used in the Norris and Reynolds modeling as adapted for the present wave-turbulent boundary layer interaction problem are presented.

5.1 Transformation of Coordinates

In the application of Norris and Reynolds, they solved the wave-perturbed equations in the following new coordinate system:

$$t^* = t \tag{5.1}$$

$$x^* = x \tag{5.2}$$

$$y^* = y - \eta(x,t)f(y) \tag{5.3}$$

where $$f(y) = \frac{\sinh\{K(2 - y)\}}{\sinh\{K(2 - \eta(x,t))\}} \tag{5.4}$$

and $K = \frac{2\pi}{\lambda}$ is the wave number.

Lines of constant y* at a given instant are shown in Figure 5.1; they are lines of constant stream function for an inviscid flow between a stationary wavy surface and a flat wall. In the transformed coordinate system, the flat and the waving surfaces do not move relative to the transformed coordinate system, i.e.,

$$y = \eta(x, t) \quad \rightarrow \quad y^*=0$$

$$y = 2 \quad \rightarrow \quad y^*=2$$

Since the y*=0 line is identical with the surface of the propagating water waves, the boundary conditions can be applied directly at the wave surface in the x*, y* coordinate system. Transferring the boundary condition to mean water surface employing Taylor series expansion is not necessary. The boundary conditions for the present wave and the turbulent boundary layer interaction problem are described in section 5.4.

5.2 Eddy Viscosity Model

The linearized perturbation Equations of (2.8) and (2.9) applied for two-dimensional boundary layer flow, with the vertical mean velocity $\bar{v}$ and the x-derivative of $\bar{u}$ considered to be small, are

Continuity Equation:

$$\frac{\partial \tilde{u}}{\partial x} + \frac{\partial \tilde{v}}{\partial y} = 0 \qquad (5.5)$$

x-Momentum Equation:

$$\frac{\partial \tilde{u}}{\partial t} + \bar{u}\frac{\partial \tilde{u}}{\partial x} + \frac{\partial \bar{u}}{\partial y}\tilde{v} = -\frac{\partial \tilde{p}}{\partial x} + \frac{1}{Re}\left(\frac{\partial^2 \tilde{u}}{\partial x^2} + \frac{\partial^2 \tilde{u}}{\partial y^2}\right) - \frac{\partial \tilde{r}_{11}}{\partial x} - \frac{\partial \tilde{r}_{12}}{\partial y} \qquad (5.6)$$

y-Momentum Equation:

$$\frac{\partial \tilde{v}}{\partial t} + \bar{u}\frac{\partial \tilde{v}}{\partial x} = -\frac{\partial \tilde{p}}{\partial y} + \frac{1}{Re}\left(\frac{\partial^2 \tilde{v}}{\partial x^2} + \frac{\partial^2 \tilde{v}}{\partial y^2}\right) - \frac{\partial \tilde{r}_{12}}{\partial x} - \frac{\partial \tilde{r}_{22}}{\partial y} \qquad (5.7)$$

There are six unknowns, namely $\tilde{u}$, $\tilde{v}$, $\tilde{p}$, $\tilde{r}_{11}$, $\tilde{r}_{22}$ and $\tilde{r}_{12}$, in the above Equations, (5.5), (5.6) and (5.7). The presence of the induced-turbulent Reynolds stresses introduces the closure problem for the set of equations. The quasilaminar model assumes that the passage of waves produces no effect on the background turbulent Reynolds stresses; consequently, the $\tilde{r}_{ij}$ terms in the above equations are zero. On the other hand, if the interactions between the wave and the turbulence field cannot be neglected, closure assumptions on the $\tilde{r}_{ij}$ terms must be made in order to obtain a solution of the perturbation quantities. The eddy viscosity closure model assumes that the wave-induced turbulent Reynolds stresses $\tilde{r}_{ij}$ are generated by the passage of a wave via the action of an eddy viscosity ν_T. In addition, the $\tilde{r}_{ij}$ are assumed to be related to the wave-induced strain rate $\tilde{S}_{ij}$ and expressed as

$$\tilde{r}_{ij} = -2\nu_T \tilde{S}_{ij} \qquad (5.8)$$

where

$$\tilde{S}_{ij} = \frac{1}{2}\left(\frac{\partial \tilde{u}_i}{\partial x_j} + \frac{\partial \tilde{u}_j}{\partial x_i}\right)$$

The eddy viscosity ν_T is assumed to be the same eddy viscosity as for the mean flow. Eliminating $\tilde{r}_{ij}$ between Equations (5.8), (5.6) and (5.7), we find that the coefficients of the resulting equations are functions of the mean flow parameters $(\bar{u}, \frac{d\bar{u}}{dy}, \frac{d^2\bar{u}}{dy^2})$ and ν_T. In order to solve the resulting equations, analytic expressions of mean velocity and eddy viscosity have to be specified throughout the complete turbulent boundary layer. The mean wind profile $\bar{u}(y)$ was measured in the experiment, but the physical limiations of instruments preclude obtaining experimental data in the close proximity of the air-water interface. Consequently, the analytic expressions of mean velocity and eddy viscosity above the progressive water wave have to be assumed. Because of the lack of experimental data, the empirical relationships describing the inner and outer regions of the turbulent boundary layer over a flat, rigid surface are used. The constants in these empirical expressions are determined with the best fit to the experimentally measured mean wind profile. Details are presented in Sections 5.2.1 and 5.2.2

5.2.1 Inner Region

Van Driest's (1956) eddy viscosity for the wall region is assumed in this calculation and expressed as a non-dimensional

eddy viscosity based on ν:

$$\nu_T = \frac{1}{2}\left[1 + 4\kappa^2 y^{+2}\left[1 - \exp(-y^+/A^+)\right]^2\right]^{\frac{1}{2}} - \frac{1}{2} \qquad (5.9)$$

where $y^+ = yu^*/\nu$, κ is the von Kármán constant, and A^+ is the parameter characterizing the viscous layer thickness on the y^+ scale. A^+ in this study was chosen such that the expressions for the inner and outer layer mean velocity profiles will overlap at $y^+ = 70$. The A^+ values for different wind velocities are described in Section 5.3.2.

The mean velocity in the wall region is defined by using Van Driest's eddy viscosity expression and the assumption of constant shear stress (Kline et al, 1968) so that

$$u^+(y^+) = \int_0^{y+} \frac{2d\zeta}{1 + \left[1 + 4\kappa^2\zeta^2\left[1 - \exp(-\zeta/A^+)\right]^2\right]^{\frac{1}{2}}}$$

$$0 \leq y^+ \leq 70 \qquad (5.10)$$

5.2.2 Outer Region

Coles' (1956) "law of the wake" expression was used for the outer region of the turbulent boundary layer. The velocity correlation in the outer region can be written as

$$\frac{U_\infty - \bar{u}}{u^*} = \frac{1}{\kappa}\ell n(y/\delta) + \frac{\Pi(x)}{\kappa}\left[1 + \cos(\pi y/\delta)\right],$$

$$\frac{70\nu}{u^*\delta} \leq y/\delta \leq 1.0 \qquad (5.11)$$

where δ is the boundary layer thickness, $70\ \nu/(u^*\delta)$ is the height corresponding to $y^+ = 70$, and Π is the wake parameter. The asymptotic matching condition between the inner and outer region velocity profiles provides (Stanford Conference, 1968):

$$\frac{U_\infty}{u^*} = \frac{1}{\kappa}\ell n\,(\delta u^*/\nu) + A + \frac{2\Pi}{\kappa} \qquad (5.11a)$$

with known values of U_∞, u^*, δ and A (obtained by least square fitting the measured mean velocity profile to $u^+ = \frac{1}{\kappa}\ell n y^+ + A$) Equation 5.11a was used to find the wake parameter.

The eddy viscosity expression was chosen such that it is a constant in the outer region and approaches κy close to the wall (Kline et al, 1968), i.e.,

$$\nu_T = F^2\left(\frac{\ell^2}{\nu}\right)\frac{d\bar{u}}{dy}$$

where ℓ is the mixing length determined, from experimental results for the turbulent boundary layer over a flat rigid surface, to be

$$\ell = 0.085\delta \tanh\left(\frac{\kappa}{0.085}\frac{y}{\delta}\right) \qquad (5.12)$$

and F is a correction factor determined from the velocity variation between the laminar sub-layer and the turbulent region. Using the law of the wall proposed by Van Driest (1956)

$$F = 1 - \exp\,(-y^+/A^+)$$

A typical comparison between the measured mean-velocity profile and the analytical expression from Equations (5.10) and (5.11) is shown in Figure 5.2. The analytic expression Equation (5.11) representing the velocity distribution in the outer region represents the experimental data quite well. (Note that the lowest height of measurement is $y^+ = 200$). Although the experimental data extends smoothly into the inner region represented by Equation (5.10), the adequacy of the representation (based on data over a rigid surface) cannot be confirmed because of the lack of detailed experimental data in close proximity of the air-water interface.

Norris and Reynolds (1975) solved the perturbation Equations (5.5 through 5.8) in the transformed coordinate system. Transformed Eddy viscocity Model was solved numerically by EDVIS, a FORTRAN program developed by Reynolds and Norris. Details relating to transformation of the governing perturbation equations into the (x^*, y^*, t^*) frame and the computer program used to solve the transformed perturbation equations were described in Norris and Reynolds (1975) and are not repeated here. In the transformed coordinate system, the mean velocity and eddy viscocity expressions above the wave surface were assumed to be the same as the expressions as described in Sections 5.2.1 and 5.2.2 with y being replaced by y^*. The comparison between the computed results and the experimental data is presented in section 5.6. The quasilaminar model computation was made by setting the eddy viscosity in the eddy viscosity model to zero.

5.3 Turbulent Kinetic Energy Model

The obvious shortcoming of the eddy viscosity model lies in the implication that the wave-induced turbulent Reynolds stresses are purely a local phenomenon and that their effect at each point is determined by the character of the mean flow at that point alone. The flux of momentum which the Reynolds stresses represent is largely the result of mixing between regions where the properties of the mean flow differ. The turbulence which accomplishes the mixing process is born, convected, diffused and dissipated through viscous action. Consequently, the turbulent structure and the mixing depend on the structure of the flow everywhere and are not strictly local phenomena. Prandtl (1945) recognized this difficulty and suggested that the turbulent kinetic energy equation must be introduced.

The turbulent kinetic energy equation may be expressed as (Norris & Reynolds, 1975)

$$\frac{\partial q^2}{\partial t} + \bar{u}_j \frac{\partial q^2}{\partial x_j} = 2\mathcal{P} - 2\mathcal{D} + \nu \frac{\partial^2 q^2}{\partial x_j \partial x_j}$$

$$- \frac{\partial}{\partial x_j} \left(\frac{1}{2} \overline{u_i' u_i' u_j'} + \overline{p' u_i'} \delta_{ij}/\rho \right) \qquad (5.13)$$

where $q^2 = \overline{u_i' u_i'}$. Here,

$$\mathcal{P} \equiv - R_{ij} S_{ij} \qquad (5.14)$$

is the "turbulence production".

and $\mathcal{D} = \nu \overline{\frac{\partial u_i'}{\partial x_j} \frac{\partial u_i'}{\partial x_j}}$ is the "isotropic dissipation" (Reynolds, 1970).

Norris and Reynolds (1975) introduced closure assumptions for $\mathcal{P}, \mathcal{D}$, the pressure velocity term and the triple velocity correlation term as follows:

The closure model for the turbulent Reynolds stresses R_{ij} is the constitutive equations

$$R_{ij} = \left(\frac{q^2}{3}\right) \delta_{ij} - 2 \nu_T S_{ij} \tag{5.15}$$

where the strain rate $S_{ij} = \frac{1}{2} \left(\frac{\partial \bar{u}_i}{\partial x_j} + \frac{\partial \bar{u}_j}{\partial x_i}\right)$

In Equation (5.15), the turbulent analogue of molecular viscous stress is assumed for R_{ij} and the eddy viscosity $\nu_T = c_1 \varepsilon$ is prescribed as a function of turbulent kinetic energy and a length scale (Prandtl, 1945) as follows

$$\nu_T = c_1 \varepsilon = c_1 q \ell \left(1 - e^{c_3 q y/\nu}\right) \tag{5.16}$$

In Equation (5.16) the small eddy viscosity characteristic of the viscous sublayer was retained by the near wall damping factor

$$\left(1 - e^{c_3 q y/\nu}\right).$$

In order to minimize the difference between the assumptions introduced in the eddy viscosity and turbulent kinetic energy models, the length scale ℓ in the turbulent kinetic energy model

was chosen to have the same characteristics as the mixing length specified for the eddy viscosity model; the length scale approaches κy in the wall region and equals a constant (0.085) in the outer region. Hence,

$$\ell = 0.085\delta\left[1 - (1 - y/\delta)^n\right] \tag{5.17}$$

where n is a constant chosen according to $n \times 0.085 = \kappa$, so that in the wall region, the length scale ℓ approaches κy. The production term $P = -R_{ij}S_{ij}$ for the special case of a shearing motion in this study is according to 5.14

$$P = -R_{12}\,S_{12} = -c_1\,\varepsilon\left(\frac{\overline{du}}{dy}\right)^2 \tag{5.18}$$

The dissipation term $\mathcal{D} = \nu\,\overline{\frac{\partial u_i'}{\partial x_j}\frac{\partial u_i'}{\partial x_j}}$ was modeled such that the behavior far from the wall is controlled by the large eddy expression $\mathcal{D} \propto q^3/\ell$ (Kolmogorov, 1942) and near the wall the dissipation is controlled by the viscosity $\mathcal{D} \propto \nu q^2/\ell^2$. The combined dissipations which include both near wall and far from the wall regions may be expressed as

$$\mathcal{D} = c_4\,\frac{q^3}{\ell}\left(1 + c_5\frac{\nu}{q\ell}\right) \tag{5.19}$$

The pressure velocity term the and triple velocity correlation term were modeled in a gradient diffusion manner, i.e.,

$$-\frac{\partial}{\partial x_j}\left(\frac{1}{2}\overline{u_i' u_i' u_j'} + \overline{p' u_i'}\,\delta_{ij}/\rho\right) = \frac{\partial}{\partial x_j}\left(c_2 \varepsilon \frac{\partial q^2}{\partial x_j}\right) \qquad (5.20)$$

The closure assumptions as discussed above contain five free constants, viz., c_1, c_2, c_3, c_4 and c_5. The determination of these constants is described in section 5.3.2.

Norris and Reynolds (1975) adopted the turbulent kinetic energy equation (5-13) and the x-momentum equation together with the assumed closure condition Equations (5-16) to (5-20) to calculate the mean flow quantities for a two-dimensional turbulent channel flow. Excellent agreement was achieved between the results of the mean model calculation and the experimental results of Hussian (1970) and Laufer (1951). It would seem natural and reasonable then to expect that these closure assumptions may be applicable to a two-dimensional channel flow with a wave-perturbed motion. Consequently, the perturbed turbulent kinetic energy equation was derived by formal perturbation of Equation (5-13) with assumed gradient diffusion term and with Equation (5-20) for the pressure velocity term and the triple velocity correlation term in Equation (5-13). The resulting perturbation turbulent kinetic energy equation is

$$\frac{\partial \tilde{q}^2}{\partial t} + \bar{u}\frac{\partial \tilde{q}^2}{\partial x} + \tilde{v}\frac{\partial Q^2}{\partial y} = 2\tilde{P} - 2\tilde{\varepsilon} + \frac{1}{Re}\left(\frac{\partial^2 \tilde{q}^2}{\partial x^2} + \frac{\partial^2 \tilde{q}^2}{\partial y^2}\right) +$$

$$c_2 E\frac{\partial^2 \tilde{q}^2}{\partial x^2} + c_2\tilde{\varepsilon}\frac{\partial^2 Q^2}{\partial y^2} + c_2 E\frac{\partial^2 \tilde{q}^2}{\partial y^2} + c_2\frac{\partial \tilde{\varepsilon}}{\partial y}\frac{\partial Q^2}{\partial y} +$$

$$c_2\frac{\partial E}{\partial y}\frac{\partial \tilde{q}^2}{\partial y} \qquad (5.21)$$

where Q^2 is the mean turbulent kinetic energy for perturbed channel flow and E is the eddy viscoscity function for the mean flow. When the formal perturbation technique used in obtaining Equation (5.21) is applied to the closure condition for the mean flow, the results are found to be

$$\tilde{r}_{ij} = \tilde{q}^2/3\,\delta_{ij} - \nu_T\left(\frac{\partial \tilde{u}_i}{\partial x_j} + \frac{\partial \tilde{u}_j}{\partial x_i}\right) - \tilde{\nu}_T\left(\frac{\partial \bar{u}_i}{\partial x_j} + \frac{\partial \bar{u}_j}{\partial x_i}\right) \qquad (5.22)$$

$$\tilde{\varepsilon} = \left[\frac{1}{2}\frac{E}{Q^2} + \frac{1}{2}c_3 ReLy^* e^{-c_3 ReQy^*}\right]\tilde{q}^2 \qquad (5.23)$$

$$\tilde{P} = c_1\tilde{\varepsilon}\left(\frac{\partial \bar{u}}{\partial y}\right)^2 + 2\,c_1 E\left[\left(\frac{\partial \tilde{u}}{\partial y}\right)\left(\frac{\partial \bar{u}}{\partial y}\right) + \left(\frac{\partial \tilde{v}}{\partial x}\right)\left(\frac{\partial \bar{u}}{\partial y}\right)\right] \qquad (5.24)$$

$$\tilde{D} = \left[\frac{3}{2}c_4\,Q/L + \frac{c_4 c_5}{Re\cdot L^2}\right]\tilde{q}^2 \qquad (5.25)$$

where $Re = QL/\nu$ and $\tilde{\nu}_T = c_1 \tilde{\varepsilon}$. Here, in contrast to the eddy viscosity model, the eddy viscosity is allowed to have perturbations in the turbulent energy model as shown in Equation (5.23), i.e., $\tilde{\varepsilon} = c_6 q^2$ where c_6 is a function only of a mean field parameter. Calculation of a perturbation turbulent energy provides a means for calculating a wave related eddy viscosity. The length scale $L = 0.085\delta \times \left[1 - (1 - y^*/\delta)^n\right]$ has been assumed as a function of y^* and the functional relationship is the same as Equation (5.17) with y being replaced by y^*. Norris and Reynolds solved Equations (5.5), (5.6), (5.7), and (5.21) together with the closure assumptions (5.22) through (5.25) in the transformed coordinate system. The transformed Turbulent Kinetic Energy Closure Model was solved numerically by use of a FORTRAN computer program developed by Reynolds and Norris. Again, the mean velocity $\bar{u}(y^*)$ and mean eddy viscosity $E(y^*)$ expression above the wave surface in our study were assumed to be same as the expressions as described in Sections (5.2.1) and (5.2.2) with y being replaced by y^*. The mean turbulent kinetic energy expression $Q(y^*)$ above the wave surface is assumed to be the same as that of a turbulent boundary layer over a flat rigid surface and is described in Section (5.3.1). The five free constants c_1, c_2, c_3, c_4, and c_5, in Equations (5.15), (5.16), (5.19) and (5.20) are dischussed in Section (5.3.2).

5.3.1 Mean Turbulent Kinetic Energy

As shown in Equation (5.21), the perturbation turbulent energy equation has non-constant coefficients determined by the

mean turbulent kinetic energy gradient. Since there was no mean turbulent energy measurement made above the wavy surface in this study, the analytic expression for the non-dimensional mean turbulent kinetic energy (based on u^*) $Q^{+2} = \frac{Q^2}{u^{*2}}$ was obtained by a curve fit of Klebanoff's (1954) turbulent boundary layer experimental results (above a solid rigid surface) with the expression

$$Q^{+2} = By^{+(2-d)} \exp\left[-\overline{d^2(\ell n y^+ - b)^2 + F}\right] \qquad (5.26)$$

where B = exp (-0.012), d = 1.115, b = 2.94 and F = 0.0001. Figure (5.3) shows the comparison between the experimental data and the curve fit of Equation (5.26).

5.3.2 The Model Constants

From Equations 5.15, 5.16, 5.19 and 5.20, the turbulent kinetic energy model contains five free constants c_1, c_2, c_3, c_4 and c_5 which need to be determined. From several known characteristics of turbulent boundary layer flows these constants can be either closely or precisely determined. First, in the logarithmic section of the layer the slope of the mean velocity profile in semi-logarithmic wall coordinates is $1/\kappa$, production and dissipation are approximately equal and the dissipation at the wall is a non-zero finite value. The constants chosen should reflect these facts and experimentally measured A^+ values and q^2 profiles. Details of the derivation of the constants are given in Norris and Reynolds (1975) and Achary and Reynolds (1975) and are not repeated here.

The main features in obtaining those constants and the constants used in this study are as follows:

1. Norris and Reynolds integrated the momentum equation for the turbulent channel flow in wall coordinates and obtained

$$c_1 = 1/q^+$$

by using the slope of $1/\kappa$ as noted above. Based on Laufer's (1951) channel flow data,

$$5.0 < q^{+2} < 8.0$$

in the logarithmic region extending from $30 \lesssim y^+ \lesssim 300$. They chose a value of $q^{+2} = 6.5$ (c_1 close to κ is a good number to choose) and obtained $c_1 = 0.39$. In this study we chose $q^{+2} = 5.95$ and obtained $c_1 = 0.41$.

2. Norris and Reynolds assumed that the turbulent diffusivity for turbulent kinetic energy and momentum should be approximately equal to each other, therefore $c_2 = c_1$. Their calculations showed that the model is not sensitive to the c_2 value chosen (they varied the c_2 value from $0.5\ c_1$ to $2\ c_1$).

3. Considering that the eddy viscosity damping factor $(1 - e^{-c_3 q^+ y^+})$ in Equation (5.16) and the Van Driest's damping factor $(1 - e^{-y^+/A^+})$ play the same role, clearly $c_3 = 1/q^+A^+$. This constant reflects experimentally measured A^+ and q^+ values. As described in Section 5.2.1, the A^+ in this study was obtained by matching the experimentally obtained mean velocity profile in the outer region (curve fit with the Equation 5.11) with the assumed inner region velocity expression of Equation 5.10. Kays (1971)

showed that $A^+ = 26$ for the flat plat boundary layer. In this study, when $U_\infty/C = 0.883$, 1.115 and 2.283, the corresponding A^+ values are 8.42, 7.55 and 6.18, respectively. This suggests that the velocity profile above the progressive water wave has a thinner sublayer as compared with that above the flat plate. In determining the q^+ value, we used Klebanoff's experimental data for turbulent boundary layer flow that in the region ($20 \leq y^+ \leq 40$) strongly affected by the eddy viscoscity damping term, $q^{+2} = 12$, therefore $q^+ = 3.464$. In Norris and Reynold's study, they used Lanfer's channel flow data and chose $q^{+2} = 8$.

4. From experimental data, it is known that in the log region production and dissipation approximately balance each other. If production and dissipation are equated

$$c_4 = c_1^3$$

5. Norris and Reynolds used the facts that at the wall the dissipation is a finite non-zero value and turbulent production and eddy viscosity are zero to determine from Equation (5.19) and the turbulent energy equation that

$$c_5 = \kappa^2/c_4$$

Therefore, a typical set of values of the model constants based on the above derivations is

$$c_1 = 1/q^+ = 0.41 \quad (q^+ = 2.55)$$

$$c_2 = c_1 = 0.41$$

$c_3 = 1/(q^+A^+) = 0.03428$ ($q^+ = 3.464$ and $A^+ = 8.42$ when $\frac{U_\infty}{C} = 0.883$)

$c_4 = c_1^3 = 0.06892$

$c_5 = \kappa^2/c_4 = 2.439$

5.4 Boundary Conditions

The boundary conditions for a channel flow with progressive waves at the lower channel boundary are as follows. Because all fluid velocities at the flat stationary upper wall are zero, the no slip condition requires, $\tilde{u} = \tilde{v} = \tilde{q}^2 = 0$ there. The lower boundary is a progressive wave and the kinematic boundary condition requires that $\tilde{u} = CK\eta$ and $\tilde{v} = -iKC\eta$ at the wave surface. Because of the effect of the wind, small ripples are generated on the surface of the mechanically-generated waves. Therefore, the turbulence energy need not vanish at the wave surface. In considering the undertainties regarding the wind field and wave field interaction and the sensitivity of the wave-induced turbulent energy boundary condition to the computation (Long, 1970), we assumed that all background turbulence velocity components are zero at the air-water interface, i.e., $\tilde{q}^2 = 0$ at wave surface.

5.5 Model Solutions and Comparisons with the Data

Norris and Reynolds solved the perturbation equations in the transformed coordinate system described above so that the boundary

conditions could be applied directly at the wave surface. Since the wave follower measurement is neither in the (x, y, t) nor in the transformed(x^*, y^*, t^*) coordinate systems, the fixed probe measurements were compared with the model predictions. After the computed results of wave-induced velocities and turbulent Reynolds stresses were obtained in the transformed coordinate system, the following steps were used to obtain the corresponding results from the fixed probe measurements.

(a) Obtain the values of $\left|\tilde{u}\ (y^*)\right|$, $\left|\tilde{v}(y^*)\right|$ and $\left|\tilde{r}_{ij}(y^*)\right|$ from the modified Norris and Reynolds (1975) computer program as a functions of y^* and phase angle (a total of 11 phase angles with 30^o increment) with respect to wave. Based on the coordinate transformation their corresponding values, i.e. $\left|\tilde{u}(y)\right|$, $\left|\tilde{v}(y)\right|$ and $\left|\tilde{r}_{ij}\ (y)\right|$ were calculated. Note that $\left|\tilde{u}(y)\right|$ is related to $\left|\tilde{u}(y^*)\right|$ by

$$\left|\tilde{u}(y)\right| = \left|\tilde{u}(y)\right| - \frac{\overline{du}}{dy} * \eta f + 0\ (\eta^2)$$

where f is given by Equation (5.4)

(b) Pick up the results of $\left|\tilde{u}(y)\right|$, $\left|\tilde{v}(y)\right|$ and $\left|\tilde{r}_{ij}(y)\right|$ from (a) for a particular value of y over different phases of the wave.

(c) Lease-square curve fit the results of (b) with a sinusoidal curve to obtain the magnitude and phase of $\tilde{u}$, $\tilde{v}$ and $\tilde{r}_{ij}$ for a fixed height above the mean water surface.

(d) Repeat (b) and (c) to obtain the magnitude and phase of $\tilde{u}$, $\tilde{v}$, and $\tilde{r}_{ij}$ for different heights above the mean water (10 heights were chosen corresponding to the heights used in the experi-

ment). The model computations were carried out for three different mean flow conditions, and the results are presented below.

5.5.1 No Critical Layer Case ($U_\infty/C = 0.883$)

Saeger and Reynolds (1971) found that their turbulent models were not adequate for the flowfield with a critical layer and better agreements were achieved for upstream running waves, i.e., cases with no critical layer in the flowfield. Therefore, it is interesting to see whether similar conclusions can be reached here.

In Figure 4.3 the trends of computed $|\tilde{u}|$ and $|\tilde{v}|$ are similar to those of the experimental data for both the eddy viscosity and turbulent energy models. However, the computed values of $|\tilde{u}|$ and $|\tilde{v}|$ are consistently higher than the experimental data. In Figure (4.4), the computed and experimental phase lags agree well. The comparisons of the magnitude of $\tilde{r}_{ij}$ are shown in Figures 4.13a, b, c. Both computer models predicted the same order of magnitude for all three components or $\tilde{r}_{ij}$, while the experimental results show order of magnitude difference among the three components of $\tilde{r}_{ij}$ in the region close to the wave surface. The comparison of the phase lag of $\tilde{r}_{ij}$ is shown in Figure 4.14a, b, c. Clearly, both models fail to predict both the magnitude and the phase angle variation as a function of non-dimensional distance Kh.

5.5.2 Thick Critical Layer Case ($U_\infty/C = 1.115$)

The critical layer height is 12.38 cm above the mean water surface. As shown in Figure 4.6, the experimental data show a sharp phase shift of the $\tilde{u}$-component near the critical layer height. Such a behavior may be used as an indication of the capability of prediction of various closure models. The quasilaminar model was included also in this case by setting the eddy viscosity in the eddy viscosity model to zero to reveal the sensitivity of the $\tilde{r}_{ij}$ terms. Figure 4.5 shows the comparison for the magnitude of wave-induced velocities. Again, all the computational results are larger than those of the experimental data. However, the difference between models is small. Figure 4.6 is the comparison for the phase lags of wave-induced velocities. The computed results agreed well with the experimental data close to the wave surface, but fail to follow the trend of the experimental data away from the surface. The eddy viscosity and quasilaminar models yield the same trend for the phase angle of the $\tilde{v}$-component, while the eddy viscosity and turbulent energy models yield the same trend for the phase angle of $\tilde{u}$-component. None of the models predict the large phase variation of $\tilde{u}$ near the critical layer. The comparisons of $\tilde{r}_{ij}$ between experimental data and computed results are shown in Figures 4.15a, b, c. Similar to the non-critical layer case, the models yield the same order of magnitude on all $|\tilde{r}_{ij}|$ while the experimental data indicate differences in their magnitude, $|\tilde{r}_{11}|$ being the largest compared to both $|\tilde{r}_{22}|$ and $|\tilde{r}_{12}|$. The corres-

ponding phase lags of $\tilde{r}_{ij}$ terms are shown in Figure 4.16a, b, c. The phase lags of $\tilde{r}_{11}$ predicted by the turbulent energy model agree well with the experimental data, while the eddy viscosity model predicted higher values. Both models fail to predict the phase lags of $\tilde{r}_{12}$ and $\tilde{r}_{22}$ variation as function of Kh.

5.5.3 Thin Critical Layer Case ($U_\infty/C = 2.283$)

In this case, the Reynolds number is the largest among all the experimental runs conducted. Because of the high wind speed the critical layer was inaccessible to the probe. Only the eddy viscosity model was analyzed in this case. Figure 4.11 shows the comparison between the experimental and computed magnitude of wave-induced velocities. Although the trends agree well with the experimental data, the computed results are higher than those of the experiments. Figure 4.12 shows the phase lag comparison for the wave-induced velocities and the trends compare favorably with those of the experiment. As shown in Figure 4.21a, b, c and 4.22a, b, c, the agreement between the computational and experimental results are poor for both the magnitude and phase of wave-induced turbulent Reynolds stresses. The model cannot predict the order of magnitude difference among $\tilde{r}_{ij}$ in the region close to the interface and cannot predict the trend of the phase lags of $\tilde{r}_{ij}$ particularly when far from the interface.

5.6 Discussion

In Norris and Reynolds (1975) the ratio of wave length to wave amplitude is 281, the Reynolds number is 13,958, and C/U_∞ for the downstream running wave is in the range $0 \leq C/U_\infty \leq 0.4$. In this study, the wave length to amplitude ratio is 62, the Reynolds number varies from 43,670 to 112,862 and C/U_∞ is in the range $0.43 \leq C/U_\infty \leq 1.13$. Norris and Reynolds (1975) (perturbation pressure calculation in channel flow of moderate Reynolds number) indicates that in the case of a long wave, the use of coordinate transformation to apply the boundary conditions directly at the wave surface seems crucial and the choice of Reynolds stress model is irrelevant. In our study the computed results from the models of Norris and Reynolds do not agree with the measured wave-induced perturbations. The results are conclusive, but the reader should note the following:

(a) The coefficients of the wave-perturbed momentum and energy equations are functions of the mean velocity and turbulent energy across the turbulent boundary layer. Due to the fact that the experimental data in close proximity to the air water interface could not be obtained, the mean velocity profile (below $y^+ = 200$) and the turbulent energy above the water waves used to calculate the coefficients were adapted from the data of turbulent boundary layer flow over a flat rigid surface. Also, the requirement that the velocity be continuous across the air-water interface restricts the mean velocity at the mobile wave surface to

be equal to the mean current. With the adapted mean velocity profile, the velocity is zero at the air-water interface. Davis pointed out in both of his studies (1970, 1972) that the model calculation is very sensitive to the mean velocity profile close to the air-water interface.

(b) The uncertainties inherent in the choice of the proper boundary condition to apply at the wave surface are the following: The water surface is roughened by the turbulent shear flow, hence the turbulent energy need not vanish at the interface and it is possible that there exists an oscillating component of turbulent energy which is correlated with the wave. Moreover, the eddy viscosity which used to represent the turbulent Reynolds stress at the interface need not vanish at the roughened wave surface. In this study, both the eddy viscosity and turbulent energy are assumed to be zero at the wave surface. Long (1971) used the non-zero boundary condition of turbulent energy at the wave surface and carried out several calculations; the computed induced pressure amplitude was too large by several orders of magnitude. His calculations imply that the model calculation is very sensitive to the boundary condition used.

(c) Is the linear model is applicable to use in this study? It is observed in this study that the measured wave-induced Reynolds stress $\overline{\tilde{u}\tilde{v}}$ is as large as the induced turbulent Reynolds stress $|\tilde{r}_{12}|$. Also as pointed out by Norris and Reynolds (1975), the calculated perturbation kinetic energy magnitudes are as

large as the mean turbulent kinetic energies. Therefore, the linear assumption used in their and in our studies for the model computation might not be applicatble.

6. CONCLUSIONS AND RECOMMENDATIONS

The overall objectives of this investigation were largely accomplished. A comprehensive and reliable set of experimental data on both the magnitude and the phase of wave-induced velocities and turbulent Reynolds stress was acquired across a turbulent boundary layer above a small amplitude 1 Hz progressive water wave. The data reveals the importance of the wave-induced turbulent Reynolds stress in the momentum transfer from wind to water waves. In addition, further numerical calculations based on various closure models for predicting the wave-induced perturbations in a turbulent shear flow should be postponed until more basic experimental data on the structure of turbulence above the air-water interface is available.

The specific conclusions derived from this study and the recommendations made for the future study are as follows:

(1) The quasilaminar model ($\tilde{r}_{ij} = 0$) is not adequate for description of water-wave generation by the wind. This study indicates that a significant contribution to the total momentum transfer from wind to wave is derived from the $\tilde{r}_{ij}$ terms and from the region close to the air-water interface.

(2) It is clear from the discussion of Section 5.6 that the experimental data for mean velocity, turbulent energy, and turbulent Reynolds stresses above the mobile deformable wave surface are important to clarify the adequacy of the eddy viscosity and turbulent energy models used in this study. Both the

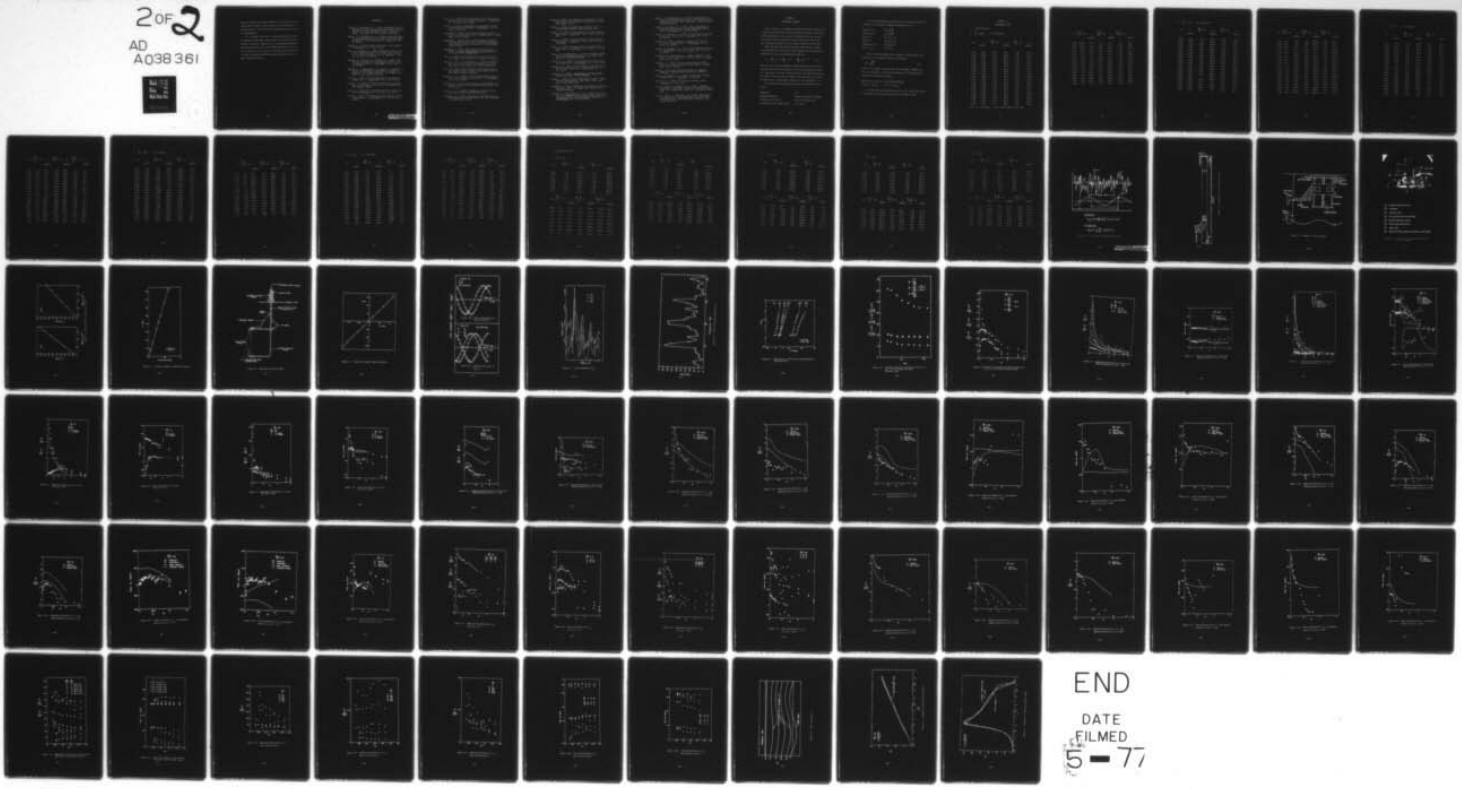
fixed and wave following frame measurements as used in this study cannot obtain the data at the air-water interface. The development of the Laser Dopler Anemometer Measurement Technique may allow us to obtain data in close proximity to the air-water interface.

(3) The effects of drift current and the superposed capillary waves, which ride on the progressive water waves, on the turbulent structure should be studied together with the detailed wave height signal to reveal better information for determining the empirical function for the closure models. Uzkard and Reynolds (1967) studied the effect of a moving rigid wall on the structure of a turbulent boundary layer. As indicated in their experimental results, the turbulent fluctuations were suppressed. If the current at the air-water interface is comparable to the movement of a solid boundary, the turbulent structure above the air-water interface would be different from that above the flat rigid surface. Also, the turbulent energy and Reynolds stresses need not vanish at the interface because the water surface is roughened by the turbulent shear flow.

(4) The magnitude of the mean quantities, e.g., velocity, eddy viscosity and turbulent kinetic energy, are assumed to be constant along a constant y^* coordinate in the model computation of this study. In other words, the functional relationships in the transformed coordinate system are assumed to be the same as those in the untransformed coordinate system except for the coordinate y being replaced by y^*. This assumption seems to be physically

AD-A038 361 STANFORD UNIV CALIF DEPT OF CIVIL ENGINEERING F/G 8/3
WAVE-INDUCED VELOCITIES AND TURBULENT REYNOLDS STRESSES ABOVE A--ETC(U)
DEC 76 S P CHAO, E Y HSU, R L STREET N00014-76-C-0155
UNCLASSIFIED TR-204 NL

2 OF 2
AD A038361



END
DATE FILMED
5-77

realistic because values adjust themselves in accordance with the passing waves instead of being constant in the untransformed coordinate system. The above described assumptions should be verified experimentally.

(5) According to the study of Acharya and Reynolds (1975), the turbulent energy model cannot predict the transfer of energy between the different components of $\tilde{r}_{ij}$ and adequate modeling of the pressure strain terms in the dynamic equations of $\tilde{r}_{ij}$ is crucial if success is to be achieved. Therefore, modeling the flow by using the turbulent Reynolds stresses equations could be of great interest and utility.

REFERENCES

Acharya, M. and Reynolds, W. C. (1975), "Measurements and Predictions of a Fully Developed Turbulent Channel Flow with Imposed Controlled Oscillations", Dept. of Mechanical Engrg., Tech, Report No. TF-8, Stanford University.

Barnett, T. P. and Wilkerson, J. C. (1967), "On the Generation of Ocean Wind Waves as Inferred from Airborne Radar Measurements of Fetch-Limited Spectra", J. Mar. Res. 25(3) pp. 292-321.

Benjamin, T. B. (1959), "Shearing Flow Over a Wavy Boundary", J. Fluid Mech., Vol. 6, pp. 161-205.

Bole, J. B. and Hsu, E. Y. (1967), "Response of Gravity Water Waves to Wind Excitation", Civil Engrg. Dept., Report No. 79, Stanford University, also J. Fluid Mech., (1969) Vol. 25, Part 4, pp. 657-675.

Bradshaw, P., Ferriss, D. H. and Atwell, N. P. (1967), "Calculation of Boundary Layer Development Using the Turbulent Energy Equation", J. Fluid Mech., Vol. 28, Part 3, pp. 593-616.

Chambers, A. J., Mangarella, P. A., Street, R. L. and Hsu, E. Y. (1970), "An Experimental Investigation of Transfer of Momentum at an Air-Water Interface", Civil Engrg. Dept., Report No. 133, Stanford University.

Coles, D. E. (1956), "The Law of the Wake in the Turbulent Boundary Layer", J. Fluid Mech., Vol. 1, pp. 191-226.

Colonell, J. M. (1966), "Laboratory Simulation of Sea Waves", Dept. of Civil Engrg., Tech. Rept. 65, Stanford University, Stanford, Calif..

Davis, R. E. (1970), "On the Turbulent Flow Over a Wavy Boundary", J. Fluid Mech., Vol. 42, Part 4, pp. 721-731.

Davis. R. E. (1972), "On Prediction of the Turbulent Flow Over a Wavy Boundary", J. Fluid Mech., Vol. 52, Part 2, pp. 287-306.

PRECEDING PAGE BLANK-NOT F

Davis, R. E. (1974), "Perturbed Turbulent Flow, Eddy Viscosity and the Generation of Turbulent Stresses", J. Fluid Mech., Vol. 63, Part 4, pp. 673-693.

Dobson, F. W. (1971), "Measurements of Atmospheric Pressure on Wind-Generated Sea Waves", J. Fluid Mech., Vol. 48, Part 1, pp. 91-127.

Hasselmann, K. (1962), "On the Nonlinear Energy Transfer in a Gravity-Wave Spectrum", Part 1, General Theory, J. Fluid Mech., 12, pp. 481-500.

Hasselmann, K. (1963), "On the Nonlinear Energy Transfer in a Gravity-Wave Spectrum", Part 2, Consevation Theorems, Wave-Particle Analogy; Irreversibility, J. Fluid Mech., 15, pp. 273-281.

Hasselmann, K. (1968), "Weak-Interaction Theory of Ocean Waves", from Basic Developments in Fluid Dynamics, Vol. 2, Ed. By M. Holt, Academic Press.

Hsu, E. Y. (1965), "A Wind, Water-Wave Research Facility", Civil Engrg. Dept., Report No. 57, Stanford University.

Hussain, A. K. M. F. and Reynolds, W. C. (1970), "The Mechanics of a Perturbation Wave in Turbulent Shear Flow", Mech. Engrg. Dept., Report FM-6, Stanford University.

Kays, W. M. (1971), "Heat Transfer to the Transpired Turbulent Boundaty Layer", Technical Report HMT-14, Dept. of Mech. Engrg. Stanford University.

Kendall, J. J. Jr. (1970), "The Turbulent Boundary layer Over a Wall with Progressive Surface Waves", J. Fluid Mech., Vol. 41, pp. 159-281.

Klebanoff, P. S. (1954), "Characteristics of Turbulence in a Boundary Layer with Zero Pressure Gradients", NACA Tech. Note No. 3178.

Kline, S. J. et al (1968), "Computation of Turbulent Boundary Layer", AFOSR-IFP-STANFORD Conference.

Kolmogorov, A. N. (1942), "Equations of Turbulent Motion of an Incompressible Turbulent Fluid", Izv. Akad, Nauk SSSR Sir Phys. VI. No. 1-2, 56.

Long, R. B. (1971), "On Generation of Ocean Waves by a Turbulent Wind", Ph.D. Dissertation, University of Miami, Coral Gables, Florida.

Laufer, J. (1951), "Investigation of Turbulent Flow in a Two-Diminsional Channel", NACA Report No. 1053.

Miles, J. W. (1957), "On the Generation of Surface Waves by Shear Flows", J. Fluid Mech., Vol. 6. Part 2, pp. 568-582.

Miles, J. W. (1959), "On the Genefation of Surface Waves by Shear Flows", J. Fluid Mech., Part 2, Vol. 6, Part 4, pp. 568-582.

Miles, J. W. (1967), "On the Generation of Surface Waves by Shear Flows", J, Fluid Mech., Vol. 30, Part 5, pp. 163-175.

Norris, H. L. and Reynolds, W. C. (1975), "Turbulent Channel Flow with a Moving Wavy Boundary", Mech. Engrg. Dept., Report TF-7, Stanford University.

Phillips, O. M. (1957), "On the Generation of Surface Waves by Turbulent Wind", J. Fluid Mech., Vol. 2, pp. 417-445.

Phillips, O. M. (1960), "On the Dynamics of Unsteady Gravity Waves of Finite Amplitude", J. Fluid Mech., Vol. 9. pp. 193-217.

Phillips, O. M. (1966), The Dynamics of the Upper Ocean, Combridge University Press, Combridge.

Prandtl, L. (1945), "Uber die Susgebildete Turbulens", ZAMN 5;136-139 (1925) and Proc. 2nd. Intern. Congr. Appl. Mech., Zurich 1926: 62-75.

Reynolds, W. C. (1970), "Computation of Turbulent Flows-State-Of-The-Art, 1970", Mech. Engrg. Dept., Report MD-27, Stanford University.

Reynolds, W. C. and Hussain, A. K. M. F. (1972), "The Mechanics of an Organized Wave in Turbulent Shear Flow. Part 3. Theoretical Models and Comparisons with Experiments", J. Fluid Mech., Vol. 54, pp. 263-288.

Saeger, J. C. and Reynolds, W. C. (1971), "Perturbation Pressures Over Traveling Sinusoidal Waves with Fully Developed Turbulent Shear Flow", Mech. Engrg. Dept., Report No. FM-9, Stanford University.

Shemdin, O. H. and Hsu, E. Y. (1967), "Direct Measurements of Aerodynamic Pressure Above a Simple Progressive Gravity Wave", J. Fluid Mech., Vol. 30, pp.403-416.

Snyder, R. L. and Cox, C. S. (1966), "A field Study of the Wind Generation of Ocean Waves", J. Mar. Res., Vol. 24 (2), pp. 141-178.

Stewart, R. H. (1970), "Laboratory Studies of the Velocity Field Over Deep-Water Waves". J. Fluid Mech., Vol. 42, Part 4, pp. 733-754.

Takeuchi, K. and Mogel, T. R. (1974), "A Performance Evaluation of a Mini-Computer", Rev. Sci. Instrum., Vol. 46, No. 6 pp. 686-691.

Tiederman, W. G. and Reynolds W. C. (1967), "Stability of Turbulent Flow with Application to Malkus' Theory", J. Fluid Mech., 27, pp. 253.

Townsend, A. A. (1972), "Flow in a Deep Turbulent Boundary Layer Over a Surface Distorted By Water Waves", J Fluid Mech., 55, pp. 719-753.

Ursell, F. (1956), "Wave Generation by Wind", in Survey in Mechanics, Cambridge University Press, pp. 216-249.

Uzkan, T. and Reynolds, W. C. (1967), "A Shear Free Turbulent Boundary Layer", J. Fluid Mech., 28, pp. 803.

Van Drist, E. R. (1956), "On Turbulent Flow Near a Wall", J. Aero. Sci., 23, pp. 1007.

Yu, H. Y., Hsu, E. Y. and Street, R. L. (1971), "A Refined Measurement of Aerodynamic Pressure Over Progressive Water Waves". Civil Engrg. Dept., Report No. 146, Stanford University.

Yu, H. Y., Hsu, E. Y. and Street, R. L. (1973), "Wave-Induced Perturbations in a Turbulent Boundary Layer Over Progressive Water Waves", Civil Engrg. Dept., Report No. 172, Stanford University.

APPENDIX I

UNCERTAINTY ANALYSIS

When a result, R, is computed from several different inputs, each of which has an uncertainty, then the value of the result is uncertain. If the uncertainties in the inputs are bounded then we can describe the greatest possible excursion in R which could occur due to the least favorable combination of the largest excursions in each input.

Kline and McClintock (1953) have shown that the way to combine the individual effect which most nearly preserves the true statistical probability is to use a root-sum-square addition:

$$\delta R = \{(\frac{\partial R}{\partial x_1} \delta x_1)^2 + (\frac{\partial R}{\partial x_2} \partial x_2)^2 + \ldots (\frac{\partial R}{\partial x_i} \delta x_i)^2\}^{\frac{1}{2}} \qquad (A.1)$$

Where the δx_i's are the independent random uncertainties with normal distributions upon which R depends and δR is the uncertainty interval in R, expressed at the same confidence level as was used in describing the inputs. Note that only the largest error and terms of like order of magnitude will significantly contribute to the uncertainty in R.

The following uncertainties were used in the uncertainty calculation.

Temperature	$\pm 1^{\circ}$ F
Pressure difference	±0.006 cm of 0.82 S. G. fluid
Calibration of hot film	±4% of calibration curve
Calibration of wave height gauge	±1% of mean

The resulting maximum uncertainties of wave induced perturbations computed by data reduction program and Equation (A-1) are

Magnitude of $\tilde{u}$	$\pm 4\%$ of $\lvert\tilde{u}\rvert$
Magnitude of $\tilde{v}$	$\pm 5\%$ of $\lvert\tilde{v}\rvert$
Phase of $\tilde{u}$	$\pm 3^{o}$ of $\tilde{u}_{\theta}$ (θ_1)
Phase of $\tilde{v}$	$\pm 4^{o}$ of $\tilde{v}_{\theta}$ (θ_2)
Magnitude of $\tilde{r}_{ij}$	$\pm 8\%$ of $\lvert\tilde{r}_{ij}\rvert$
Phase of $\tilde{r}_{ij}$	$\pm 5^{o}$ of θ_{ij}

Besides the single-sample error estimate as described above, the uncertainty in the spectral result is estimated by

$$\epsilon = \sqrt{\frac{1}{N}} \qquad \text{(A-2)}$$

where N is the number of spectra used for the average, and ϵ is the error in the spectra. The resulting uncertainty of wave induced perturbation for 60 spectra average is

Magnitude of $\tilde{u}_i$ and $\tilde{r}_{ij}$	$\pm$ 13% of $\lvert\tilde{u}_i\rvert$ and $\lvert\tilde{r}_{ij}\rvert$
Phase of $\tilde{u}_i$ and $\tilde{r}_{ij}$	$\pm 8^{o}$ of θ_i and θ_{ij}

The statistical uncertainty due to the use of a finite data record is much greater than the uncertainty due to instrument errors.

APPENDIX II

EXPERIMENTAL DATA [1]

A. Fixed Probe Data

1. $\frac{U_\infty}{C} = 0.883$ $\quad \dot{u}^* = 0.0725$ m/sec

Kh	$\bar{u}$ (m/sec)	$\frac{\lvert\tilde{u}\rvert}{U_\infty} \times 10^2$	$\tilde{u}_\theta$ (degree)	$\frac{\lvert\tilde{v}\rvert}{U_\infty} \times 10^2$	$\tilde{v}_\theta$ (degree)
0.143	0.947	10.46	184.2	1.86	275.1
0.166	0.989	7.43	183.3	1.82	278.8
0.191	1.041	6.43	182.9	1.76	276.1
0.217	1.054	5.70	185.5	1.66	275.4
0.242	1.082	4.91	181.0	1.59	276.3
0.268	1.104	4.52	182.2	1.49	275.8
0.293	1.128	4.17	179.4	1.47	277.9
0.319	1.142	3.73	180.0	1.41	278.1
0.344	1.149	3.33	175.0	1.39	279.0
0.396	1.182	3.01	182.7	1.27	278.8
0.447	1.204	2.42	187.3	1.07	277.0
0.498	1.192	2.00	185.2	0.88	281.2
0.549	1.226	1.70	185.8	0.85	275.7
0.600	1.256	1.80	197.6	0.76	274.7
0.651	1.279	1.77	192.9	0.66	277.1
0.702	1.283	1.41	192.9	0.59	281.8
0.804	1.312	0.89	198.9	0.51	270.4
0.008	1.343	0.59	194.2	0.42	268.4
0.314	1.374	0.15	202.1	0.32	282.8
1.488	1.379	0.11	208.2	0.35	276.8

[1] Note: $C = 1.564$ m/sec $\quad K = \frac{2\pi}{\lambda} = 4.019$ rad/m for all cases.

Kh	$\frac{\lvert \tilde{r}_{11} \rvert}{U_\infty^2} \times 10^4$	θ_{11} (degree)	$\frac{\lvert \tilde{r}_{22} \rvert}{U_\infty^2} \times 10^4$	θ_{22} (degree)	$\frac{\lvert \tilde{r}_{12} \rvert}{U_\infty^2} \times 10^4$	θ_{12} (degree)
0.143	100.94	30.2	0.70	92.2	4.06	308.1
0.166	38.23	42.2	0.87	76.2	2.35	264.8
0.191	23.93	44.0	0.85	80.5	2.58	253.0
0.217	15.13	53.9	0.56	100.8	1.79	254.2
0.242	11.46	67.2	0.57	79.5	1.99	236.8
0.319	6.67	51.3	0.32	54.3	1.36	228.0
0.344	4.49	47.0	0.60	32.4	1.45	232.2
0.396	2.87	58.4	0.49	356.2	1.46	237.0
0.498	2.26	48.3	0.44	347.5	0.88	237.4
0.549	1.51	22.0	0.49	332.1	0.94	207.5
0.600	1.81	111.5	0.37	348.8	0.75	212.3
0.651	1.71	137.0	0.31	321.1	0.65	196.2
0.804	0.57	187.6	0.45	292.0	0.42	201.5
0.008	0.35	209.0	0.21	187.0	0.32	209.2
0.314	0.28	208.2	0.23	195.0	0.22	189.4
1.488	0.22	207.0	0.04	180.1	0.18	275.0

2. $\frac{U_\infty}{C} = 1.115$ $\quad u^* = 0.0927$ m/sec

Kh	$\overline{u}$ (m/sec)	$\frac{\lvert\tilde{u}\rvert}{U_\infty} \times 10^2$	$\tilde{u}_\theta$ (degree)	$\frac{\lvert\tilde{v}\rvert}{U_\infty} \times 10^2$	$\tilde{v}_\theta$ (degree)
0.130	1.263	7.03	187.2	0.58	267.1
0.140	1.278	6.51	187.8	0.55	269.1
0.166	1.319	5.88	189.0	0.49	269.7
0.191	1.349	4.81	191.1	0.51	267.2
0.217	1.379	3.96	189.6	0.44	273.5
0.242	1.401	3.72	190.5	0.36	273.6
0.268	1.419	3.08	189.3	0.38	263.5
0.293	1.435	2.77	196.9	0.32	267.8
0.319	1.461	2.50	188.3	0.29	260.9
0.396	1.503	1.60	192.9	0.21	243.1
0.447	1.532	1.02	190.7	0.19	231.5
0.498	1.560	0.72	195.0	0.17	217.8
0.549	1.567	0.59	185.1	0.16	232.9
0.600	1.604	0.36	166.0	0.16	206.9
0.651	1.624		330.7	0.11	191.8
0.702	1.639	0.26	330.6	0.12	171.7
0.804	1.667	0.25	7.7	0.17	149.3
1.008	1.714	0.23	112.4	0.12	94.0
1.714	1.740	0.15	83.4	0.1	56.6
1.488	1.741	0.14	77.3	0.07	66.7

Kh	$\frac{\lvert\tilde{r}_{11}\rvert}{U_\infty^2} \times 10^4$	θ_{11} (degree)	$\frac{\lvert\tilde{r}_{22}\rvert}{U_\infty^2} \times 10^4$	θ_{22} (degree)	$\frac{\lvert\tilde{r}_{12}\rvert}{U_\infty^2} \times 10^4$	θ_{12} (degree)
0.130	40.0	6.08	0.11	330.99	1.09	339.45
0.140	35.0	6.94	0.28	406.8	0.76	272.47
0.166	25.9	14.0	0.53	24.92	1.48	214.44
0.191	19.4	32.53	0.65	29.21	1.28	215.97
0.217	14.9	35.17	0.81	47.5	1.75	200.99
0.242	15.6	36.82	0.80	32.37	1.75	192.27
0.268	13.1	41.35	0.87	40.17	1.65	182.35
0.293	12.4	40.17	0.90	47.33	1.70	181.03
0.319	13.4	43.21	0.84	32.00	1.42	187.35
0.396	10.9	41.49	0.89	30.09	1.23	188.97
0.447	6.13	49.49	0.67	35.23	0.55	156.23
0.498	7.67	38.72	0.71	26.07	0.94	174.82
0.549	5.75	41.26	0.75	39.03	0.59	171.15
0.60	3.99	29.53	0.53	26.41	0.45	163.84
0.651	3.45	23.32	0.49	33.99	0.27	160.32
0.702	3.05	33.9	0.39	24.99	0.16	207.62
0.804	1.94	29.84	0.30	11.26	0.26	284.69
1.008	2.05	352.83	0.20	331.57	0.17	263.25
1.314	0.47	311.42	0.14	290.95	0.15	239.38
1.488	0.31	319.63	0.12	303.93	0.12	233.73

3. $\frac{U_\infty}{C} = 1.34$ $\quad u^* = 0.121$ m/sec

Kh	$\bar{u}$ (m/sec)	$\frac{\lvert\tilde{u}\rvert}{U_\infty} \times 10^2$	$\tilde{u}_\theta$ (degree)	$\frac{\lvert\tilde{v}\rvert}{U_\infty} \times 10^2$	$\tilde{v}_\theta$ (degree)
0.156	1.392	6.45	166.8	0.23	299.0
0.166	1.417	5.74	162.9	0.28	311.0
0.191	1.426	5.15	163.3	0.25	328.2
0.217	1.454	4.78	162.6	0.23	356.5
0.242	1.474	4.15	157.8	0.30	11.4
0.268	1.502	3.80	158.1	0.34	25.1
0.293	1.532	3.70	154.0	0.46	23.4
0.319	1.559	3.03	151.3	0.59	28.7
0.344	1.576	2.91	151.1	0.57	33.0
0.396	1.627	2.41	136.0	0.72	38.6
0.447	1.674	2.12	129.6	0.86	33.6
0.498	1.715	1.83	128.5	0.97	31.7
0.549	1.762	1.40	134.9	1.05	32.1
0.60	1.788	1.06	122.5	1.17	27.8
0.651	1.792	0.93	120.1	1.12	28.2
0.702	1.824	0.64	117.4	1.13	27.4
0.804	1.958	0.30	149.2	1.01	26.9
0.008	2.108	0.22	93.4	0.82	26.7
1.314	2.086	0.12	17.8	0.41	27.8
1.488	2.122	0.10	333.7	0.35	24.8

Kh	$\frac{\lvert\tilde{r}_{11}\rvert}{U_\infty^2} \times 10^4$	θ_{11} (degree)	$\frac{\lvert\tilde{r}_{22}\rvert}{U_\infty^2} \times 10^4$	θ_{22} (degree)	$\frac{\lvert\tilde{r}_{12}\rvert}{U_\infty^2} \times 10^4$	θ_{12} (degree)
0.156	31.4	14.0	0.181	330.4	2.75	77.5
0.166	24.8	16.2	0.137	309.2	2.55	79.1
0.191	22.1	27.1	0.526	329.8	2.54	88.2
0.217	20.4	24.4	0.525	333.2	2.43	93.0
0.242	18.1	24.2	0.496	350.5	1.99	112.3
0.268	17.4	20.9	0.456	334.5	2.04	92.5
0.293	17.0	19.2	0.588	328.9	1.90	95.3
0.319	17.4	12.3	0.803	332.0	1.75	106.6
0.344	14.0	8.7	0.501	339.2	1.45	89.5
0.396	12.8	357.7	0.484	324.4	1.45	82.3
0.447	13.2	4.04	0.780	354.7	0.91	77.5
0.498	11.1	350.2	0.886	340.1	0.97	83.7
0.549	9.8	345.6	0.598	347.5	0.69	61.3
0.60	8.4	342.5	0.998	329.7	0.68	39.4
0.651	7.4	341.1	0.984	342.1	0.73	23.1
0.702	6.2	336.1	0.981	338.6	0.51	350.2
0.804	5.6	353.9	0.60	19.3	0.30	208.9
0.008	3.2	310.8	0.296	17.3	0.20	205.9
1.314	1.09	246.3	0.285	225.4	0.27	205.1
1.488	0.3	192.3	0.104	216.2	0.11	194.2

4. $\frac{U_\infty}{C} = 1.836$ $\quad u^* = 0.137$ m/sec

Kh	$\bar{u}$ (m/sec)	$\frac{\lvert\tilde{u}\rvert}{U_\infty} \times 10^2$	$\tilde{u}_\theta$ (degree)	$\frac{\lvert\tilde{v}\rvert}{U_\infty} \times 10^2$	$\tilde{v}_\theta$ (degree)
0.136	2.136	3.53	130.8	0.824	25.8
0.140	2.162	3.28	129.0	0.789	27.3
0.166	2.251	1.68	113.9	0.816	32.0
0.191	2.265	1.60	79.8	0.766	31.9
0.217	2.331	0.861	64.5	0.824	29.1
0.242	2.374	1.11	21.8	0.77	28.3
0.268	2.403	1.10	15.2	0.733	26.5
0.293	2.409	0.954	3.5	0.729	21.0
0.319	2.446	0.998	339.3	0.706	22.9
0.396	2.523	0.798	318.5	0.641	16.2
0.447	2.569	1.01	288.9	0.631	16.3
0.498	2.607	0.532	315.6	0.553	6.2
0.549	2.628	0.523	289.9	0.546	13.9
0.60	2.674	0.291	314.5	0.506	7.6
0.651	2.688	0.388	309.3	0.511	12.1
0.702	2.705	0.477	312.8	0.423	13.9
0.804	2.787	0.469	313.8	0.401	6.1
1.008	2.830	0.274	290.8	0.345	353.3
1.314	2.859	0.051	192.4	0.271	335.6
1.473	2.871	0.032	186.8	0.215	340.2

Kh	$\frac{\lvert\tilde{r}_{11}\rvert}{U_\infty^2} \times 10^4$	θ_{11} (degree)	$\frac{\lvert\tilde{r}_{22}\rvert}{U_\infty^2} \times 10^4$	θ_{22} (degree)	$\frac{\lvert\tilde{r}_{12}\rvert}{U_\infty^2} \times 10^4$	θ_{12} (degree)
0.136	21.9	333.1	0.61	238.4	4.9	66.4
0.140	11.2	325.5	0.49	236.8	3.49	62.5
0.166	12.5	292.6	0.44	204.7	3.05	56.4
0.191	10.9	282.4	0.49	225.3	2.44	48.3
0.217	9.2	250.7	0.69	237.5	1.24	42.2
0.242	7.3	249.0	0.70	199.1	1.34	39.5
0.268	5.9	243.3	0.79	194.6	0.75	43.5
0.293	4.95	237.5	0.53	191.5	0.77	30.9
0.319	2.65	228.8	0.46	176.2	0.65	25.5
0.396	3.28	198.8	0.78	132.3	0.61	15.8
0.549	2.63	179.6	0.27	10.9	0.5	126.3
0.60	2.72	7.3	0.355	338.1	0.82	169.4
0.702	1.09	293.1	0.375	319.1	0.67	118.7
1.008	1.4	193.2	0.25	107.7	0.43	79.3
1.314	1.02	72.4	0.21	61.5	0.37	224.1
1.473	0.83	39.8	0.209	27.6	0.345	223.3

5. $\frac{U_\infty}{C} = 2.283$ $\quad u^* = 0.261$ m/sec

Kh	$\bar{u}$ (m/sec)	$\frac{\lvert\tilde{u}\rvert}{U_\infty} \times 10^2$	$\tilde{u}_\theta$ (degree)	$\frac{\lvert\tilde{v}\rvert}{U_\infty} \times 10^2$	$\tilde{v}_\theta$ (degree)
0.140	2.387	2.77	131.5	1.1	54.7
0.166	2.479	1.42	92.5	1.15	57.0
0.191	2.546	0.91	50.4	1.17	48.8
0.217	2.607	1.23	354.5	1.10	57.1
0.242	2.680	1.47	318.0	1.11	49.8
0.268	2.702	1.25	345.0	1.02	44.0
0.293	2.764	1.61	323.0	0.96	51.0
0.319	2.797	1.30	330.9	0.91	45.2
0.344	2.819	1.20	327.8	0.87	49.3
0.396	2.874	0.93	321.2	0.81	49.7
0.447	2.927	0.581	330.7	0.774	47.2
0.498	3.020	0.663	343.1	0.693	55.2
0.549	3.046	0.611	12.8	0.669	47.3
0.60	3.080	0.517	17.8	0.661	41.2
0.651	3.131	0.605	24.8	0.656	36.8
0.702	3.171	0.835	27.0	0.613	41.0
0.804	3.265	0.614	24.5	0.632	33.4
1.008	3.009	0.247	350.7	0.188	22.0
1.314	3.339	0.157	345.1	0.140	11.5
1.480	3.563	0.106	340.2	0.1	11.4

Kh	$\frac{\lvert\tilde{r}_{11}\rvert}{U_\infty^2} \times 10^4$	θ_{11} (degree)	$\frac{\lvert\tilde{r}_{22}\rvert}{U_\infty^2} \times 10^4$	θ_{22} (degree)	$\frac{\lvert\tilde{r}_{12}\rvert}{U_\infty^2} \times 10^4$	θ_{12} (degree)
0.140	19.2	311.9	1.12	246.5	3.6	50.3
0.166	16.2	281.3	1.08	210.2	3.3	44.1
0.191	12.4	259.0	1.14	175.3	3.55	45.8
0.217	10.0	252.2	0.85	138.4	3.1	43.9
0.242	8.5	230.1	1.05	128.2	2.9	32.6
0.268	7.5	225.7	0.72	103.7	2.85	14.8
0.293	7.3	207.3	0.67	97.9	2.25	2.4
0.319	6.9	170.7	0.58	101.0	2.2	338.2
0.344	6.9	190.8	0.51	89.0	1.48	21.3
0.396	3.45	134.4	0.24	64.9	0.76	281.7
0.447	2.82	214.4	0.17	23.9	0.39	225.5
0.498	1.7	303.3	0.35	330.0	0.2	165.7
0.651	1.5	282.9	0.24	300.1	0.17	178.2
0.702	1.1	246.5	0.2	280.5	0.13	172.6
0.804	1.1	343.8	0.15	283.9	0.18	185.1
1.008	1.3	334.8	0.17	23.9	0.11	194.0
1.314	0.5	317.3	0.14	29.8	0.11	190.0
1.480	0.2	320.0	0.12	30.0	0.11	195.0

B. Wave Follower Data

1. $\frac{U_\infty}{C} = 1.115$

Kh_f	$\frac{\lvert\tilde{u}\rvert}{U_\infty} \times 10^2$	$\tilde{u}_\theta$ (degree)	$\frac{\lvert\tilde{v}\rvert}{U_\infty} \times 10^2$	$\tilde{v}_\theta$ (degree)
0.036	5.04	123.64	7.43	268.97
0.051	3.19	127.19	7.73	269.44
0.077	2.20	118.37	7.55	269.92
0.102	1.70	91.92	7.08	269.51
0.128	2.13	87.23	7.32	269.33
0.153	1.94	83.14	6.90	69.96
0.179	1.89	84.1	6.74	269.49
0.214	2.17	74.03	6.65	269.72

Kh_f	$\frac{\lvert\tilde{r}_{11}\rvert}{U_\infty^2} \times 10^4$	θ_{11} (degree)	$\frac{\lvert\tilde{r}_{12}\rvert}{U_\infty^2} \times 10^4$	θ_{12} (degree)	$\frac{\lvert\tilde{r}_{22}\rvert}{U_\infty^2} \times 10^4$	θ_{22} (degree)
0.036	19.61	32.69	11.27	118.2	10.28	348.6
0.051	17.46	22.27	13.64	124.21	16.27	344.12
0.077	9.33	62.83	7.17	117.05	14.67	343.66
0.102	9.56	52.59	6.14	122.93	14.60	349.21
0.128	8.84	76.03	6.46	130.69	17.04	338.51
0.153	9.16	43.03	6.79	148.08	18.35	346.34
0.179	6.60	100.93	7.38	136.25	19.24	344.33
0.214	5.27	101.63	6.29	139.76	17.97	346.65

2. $\frac{U_\infty}{C} = 1.34$

Kh_f	$\frac{\lvert\tilde{u}\rvert}{U_\infty} \times 10^2$	$\tilde{u}_\theta$ (degree)	$\frac{\lvert\tilde{v}\rvert}{U_\infty} \times$ [illegible] ^{2}	$\tilde{v}_\theta$ (degree)
0.036	3.95	114.66	5.11	271.46
0.051	3.15	116.9	4.90	270.39
0.077	2.62	120.3	4.68	270.14
0.102	1.19	114.15	4.51	270.22
0.128	1.01	90.27	4.56	270.77
0.153	1.06	91.03	4.43	270.78
0.179	1.20	65.93	4.32	270.48
0.214	1.61	54.89	4.10	270.64

Kh_f	$\frac{\lvert\tilde{r}_{11}\rvert}{U_\infty^2} \times 10^4$	θ_{11} (degree)	$\frac{\lvert\tilde{r}_{12}\rvert}{U_\infty^2} \times 10^4$	θ_{12} (degree)	$\frac{\lvert\tilde{r}_{22}\rvert}{U_\infty^2} \times 10^4$	θ_{22} (degree)
0.036	11.29	336.97	14.95	120.71	11.46	1.33
0.051	10.76	357.21	11.51	115.41	10.44	358.71
0.077	11.10	17.25	10.86	121.85	10.38	8.46
0.102	7.30	61.45	9.07	120.25	10.93	8.23
0.128	11.74	52.92	6.38	122.86	10.62	7.99
0.153	12.9	53.99	6.24	129.04	11.69	2.83
0.179	9.12	57.01	6.93	129.83	12.02	7.04
0.214	7.86	53.55	5.52	135.21	10.51	5.92

3. $\frac{U_\infty}{C} = 1.49$

Kh_f	$\frac{\lvert\tilde{u}\rvert}{U_\infty} \times 10^2$	$\tilde{u}_\theta$ (degree)	$\frac{\lvert\tilde{v}\rvert}{U_\infty} \times 10^2$	$\tilde{v}_\theta$ (degree)
0.451	2.86	122.15	3.53	276.38
0.051	2.78	119.33	3.35	275.39
0.077	2.54	120.18	3.06	276.49
0.102	1.73	122.54	2.95	276.49
0.128	1.52	177.92	2.78	277.19
0.153	1.38	128.02	2.63	278.9
0.174	1.29	110.34	2.46	280.97
0.214	1.36	104.39	2.48	282.04

Kh_f	$\frac{\lvert\tilde{r}_{11}\rvert}{U_\infty^2} \times 10^4$	θ_{11} (degree)	$\frac{\lvert\tilde{r}_{12}\rvert}{U_\infty^2} \times 10^4$	θ_{12} (degree)	$\frac{\lvert\tilde{r}_{22}\rvert}{U_\infty^2} \times 10^4$	θ_{22} (degree)
0.041	8.88	338	7.17	118.61	4.62	1.89
0.051	9.84	344.36	6.65	113.73	4.80	5.03
0.077	6.17	7.07	4.27	111.37	4.57	5.26
0.102	8.43	12.33	4.19	120.25	5.01	0.59
0.128	7.06	22.19	4.36	137.54	5.84	3.86
0.153	6.57	29.95	3.95	139.85	5.93	1.89
0.174	7.95	31.33	3.96	136.25	5.77	1.64
0.214	8.37	19.79	3.07	127.02	5.16	356.13

4. $\frac{U_\infty}{C} = 1.836$

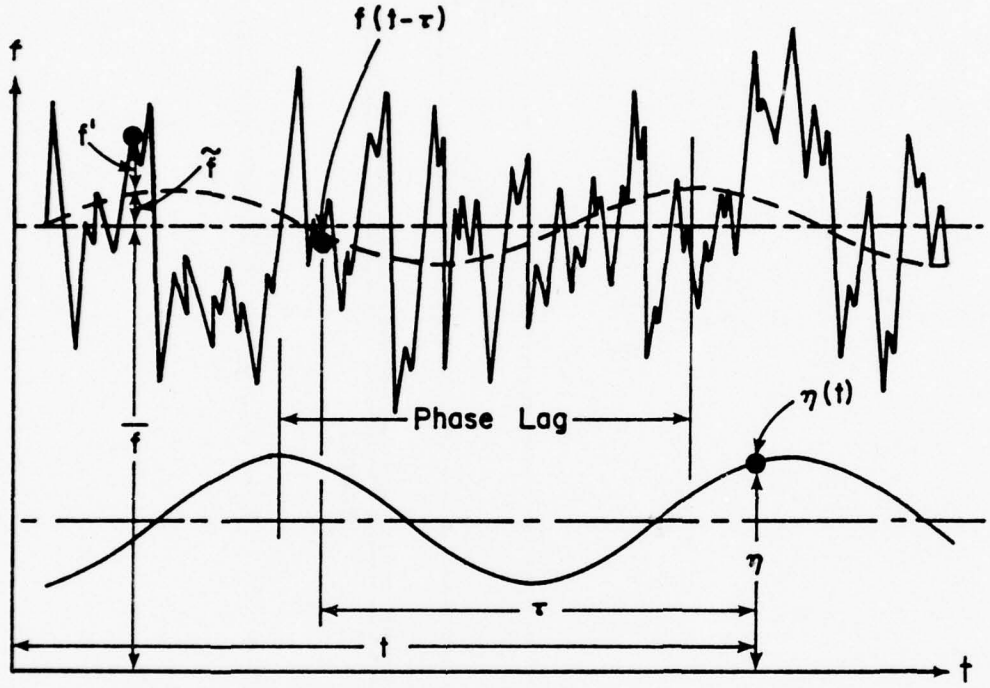
Kh_f	$\frac{\lvert\tilde{u}\rvert}{U_\infty} \times 10^2$	$\tilde{u}_\theta$ (degree)	$\frac{\lvert\tilde{v}\rvert}{U_\infty} \times 10^2$	$\tilde{v}_\theta$ (degree)
0.056	8.31	52.19	1.68	291.77
0.061	8.12	49.09	1.58	295.77
0.077	6.63	45.84	1.94	288.17
0.102	6.76	42.93	2.17	284.79
0.128	6.33	34.04	2.01	288.19
0.135	6.32	29.84	2.09	284.84
0.179	5.38	27.45	2.53	280.23
0.214	4.68	20.58	2.68	280.02

Kh_f	$\frac{\lvert\tilde{r}_{11}\rvert}{U_\infty^2} \times 10^4$	θ_{11} (degree)	$\frac{\lvert\tilde{r}_{12}\rvert}{U_\infty^2} \times 10^4$	θ_{12} (degree)	$\frac{\lvert\tilde{r}_{22}\rvert}{U_\infty^2} \times 10^4$	θ_{22} (degree)
0.056	61.03	312.09	8.88	89.3	2.95	317.91
0.061	55.07	318.94	8.4	75.83	3.90	325.27
0.077	40.53	307.83	6.50	85.6	2.89	323.32
0.102	37.74	311.4	6.07	92.31	3.38	318.76
0.128	33.82	305.5	5.42	83.79	3.05	321.44
0.135	29.14	297.43	5.06	74.23	2.71	304.01
0.179	23.81	292.77	3.58	75.77	3.27	319.83
0.214	19.52	280.47	3.17	55.59	4.17	317.04

5. $\frac{U_\infty}{C} = 2.283$

Kh_f	$\frac{\lvert\tilde{u}\rvert}{U_\infty} \times 10^2$	$\tilde{u}_\theta$ (degree)	$\frac{\lvert\tilde{v}\rvert}{U_\infty} \times 10^2$	$\tilde{v}_\theta$ (degree)
0.056	7.00	31.77	0.54	303.99
0.061	6.90	32.13	0.65	306.76
0.077	6.81	26.87	0.72	317.43
0.102	7.00	20.7	0.81	317.78
0.128	6.68	16.55	0.80	311.22
0.153	6.71	11.59	0.81	311.22
0.179	6.06	5.61	0.82	318.75
0.214	5.67	1.49	0.79	314.83

Kh_f	$\frac{\lvert\tilde{r}_{11}\rvert}{U_\infty^2} \times 10^4$	θ_{11} (degree)	$\frac{\lvert\tilde{r}_{12}\rvert}{U_\infty^2} \times 10^4$	θ_{12} (degree)	$\frac{\lvert\tilde{r}_{22}\rvert}{U_\infty^2} \times 10^4$	θ_{22} (degree)
0.056	38.64	325.32	6.82	75.75	12.31	271.37
0.061	32.75	328.18	6.44	83.12	13.78	263.61
0.077	33.07	319.65	6.4	79.44	13.43	269.27
0.102	25.03	302.61	6.38	55.63	10.97	239.09
0.128	24.39	285.4	4.84	55.28	10.62	236.22
0.153	26.43	277.0	4.67	51.89	9.57	227.12
0.179	15.7	266.86	4.44	48.05	8.94	222.53
0.214	15.23	257.7	3.76	39.5	9.59	207.38



DEFINITION:

$$R_{\eta f}(\tau) \equiv \underset{T-\infty}{\text{LIM}} \frac{1}{T} \int_0^T \eta(t)\, f(t-\tau)\, dt$$

IN PRACTICE:

$$R_{\eta f}(\tau) = \frac{1}{N} \sum_{i=1}^{N} \eta(t_i)\, f(t_i - \tau)$$

Figure 2.1 Cross Correlation and Decomposition

PRECEDING PAGE BLANK-NOT FILMED

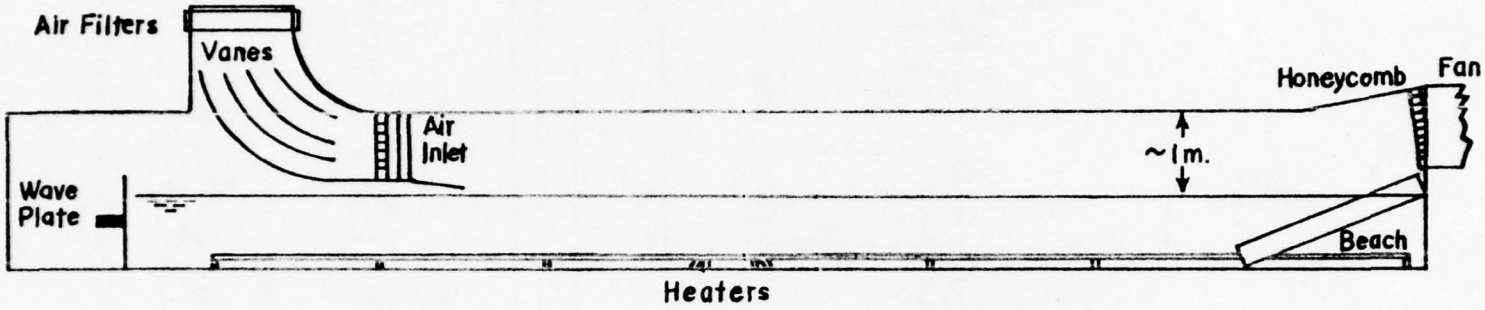


Figure 3.1 Schematic of the Wind-Wave Facility

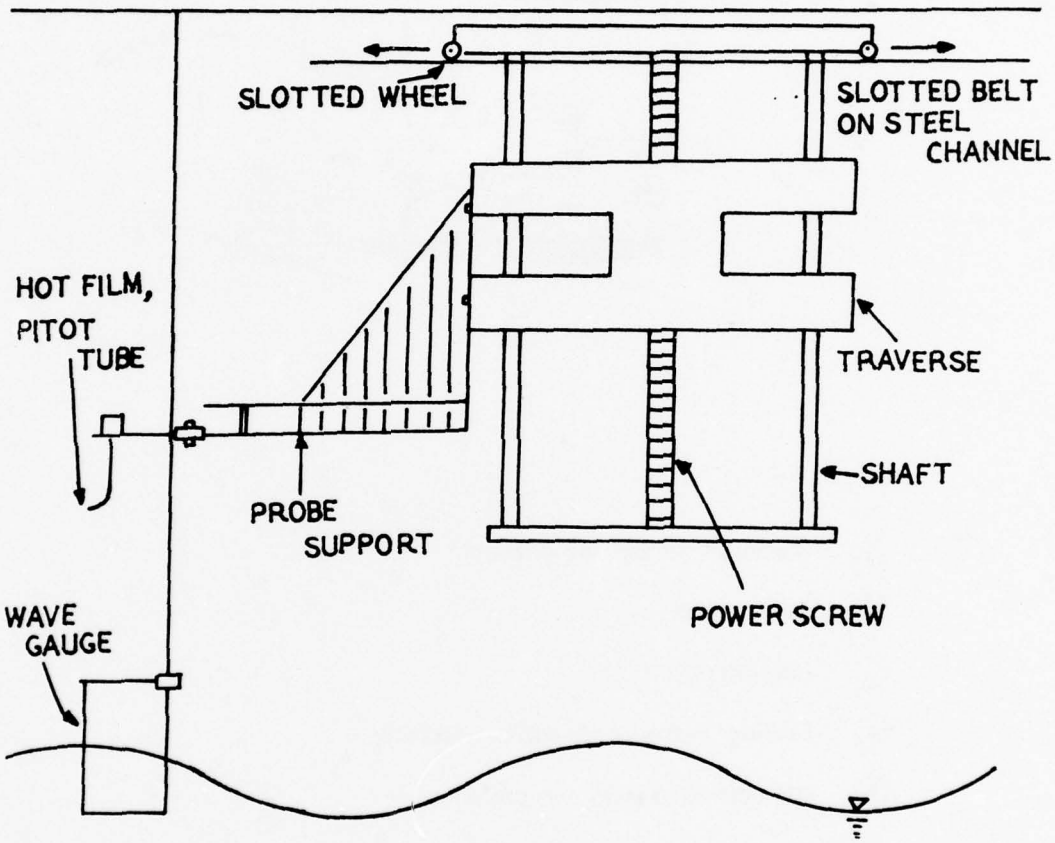
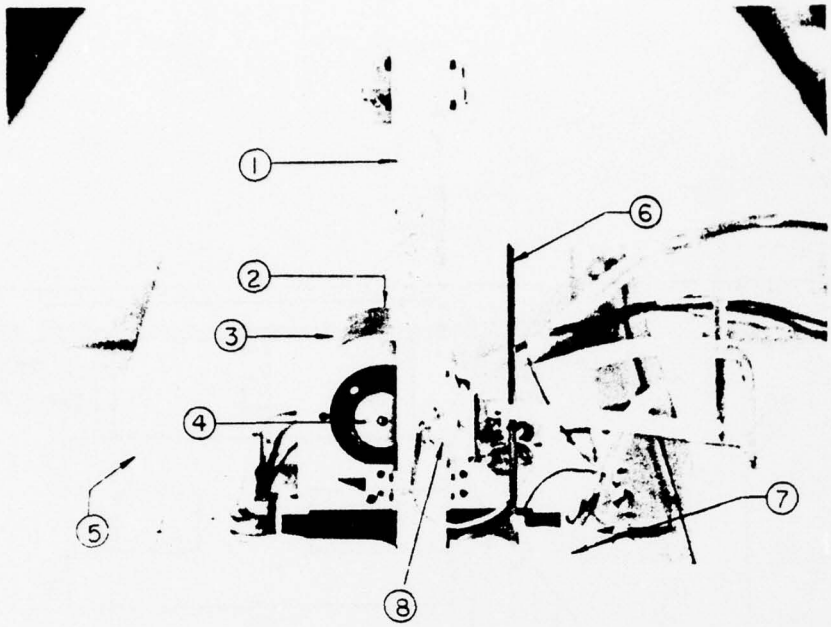


Figure 3.2 Schematic of Probe Carriage



① Aluminum supporting channel

② Tachometer

③ Low-inertia motor

④ Driving pulley-and-cable assembly

⑤ Movable aluminum structure

⑥ Wave-gauge supporting rod

⑦ Center plate

⑧ Pulley-and-cable assembly and position potentiometer

Figure 3.3 Wave Follower Installation Outside the Wind Wave Channel

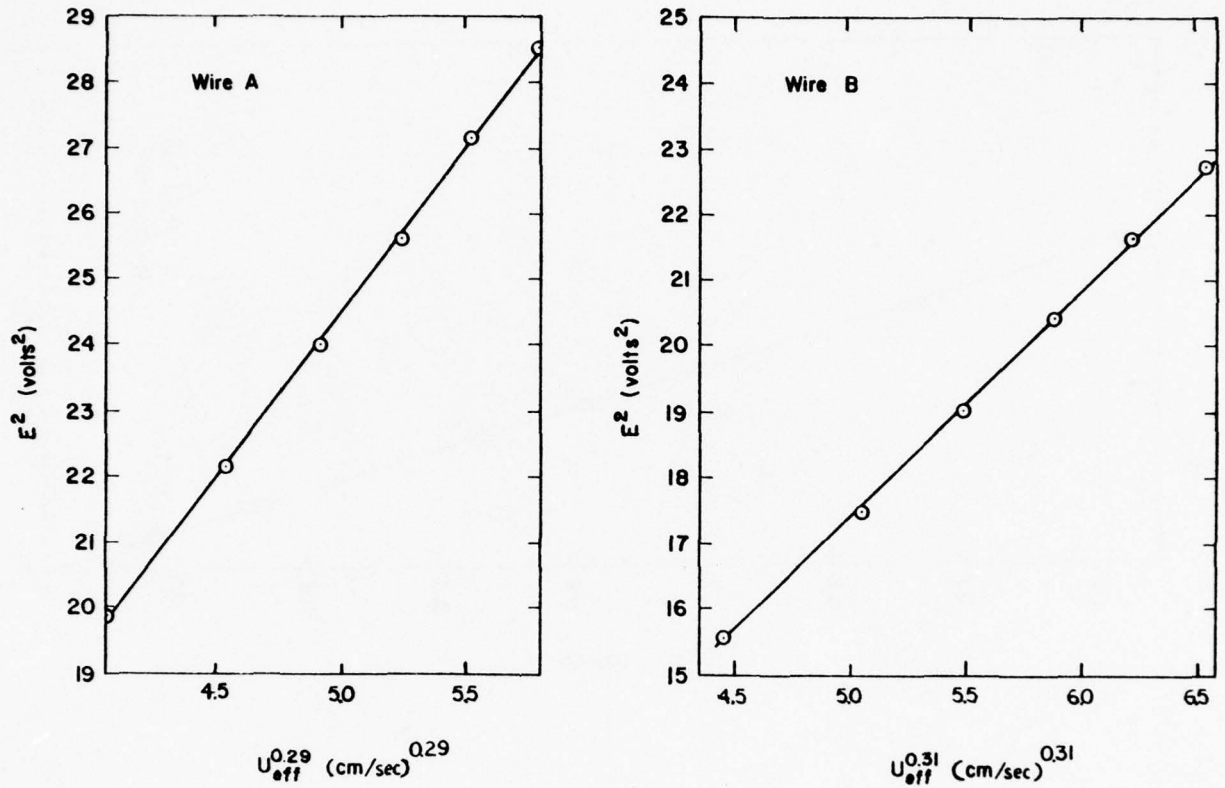


Figure 3.4 Typical Hot Film Calibration Curves

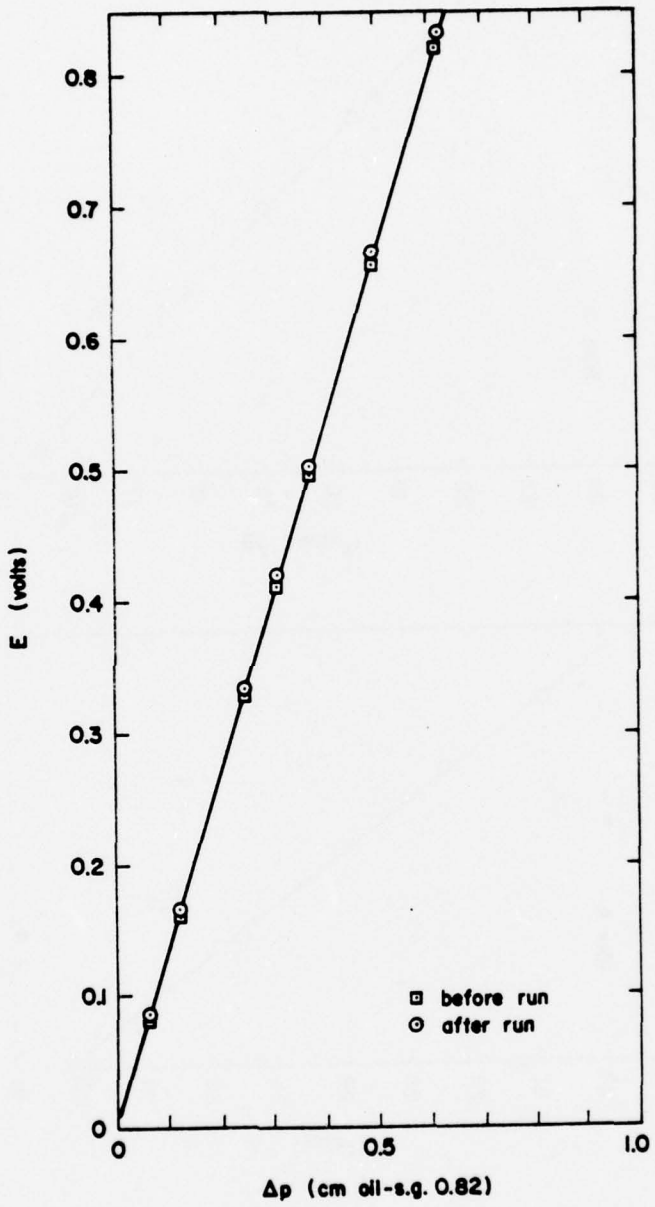


Figure 3.5 Pressure Transducer Calibration Curves

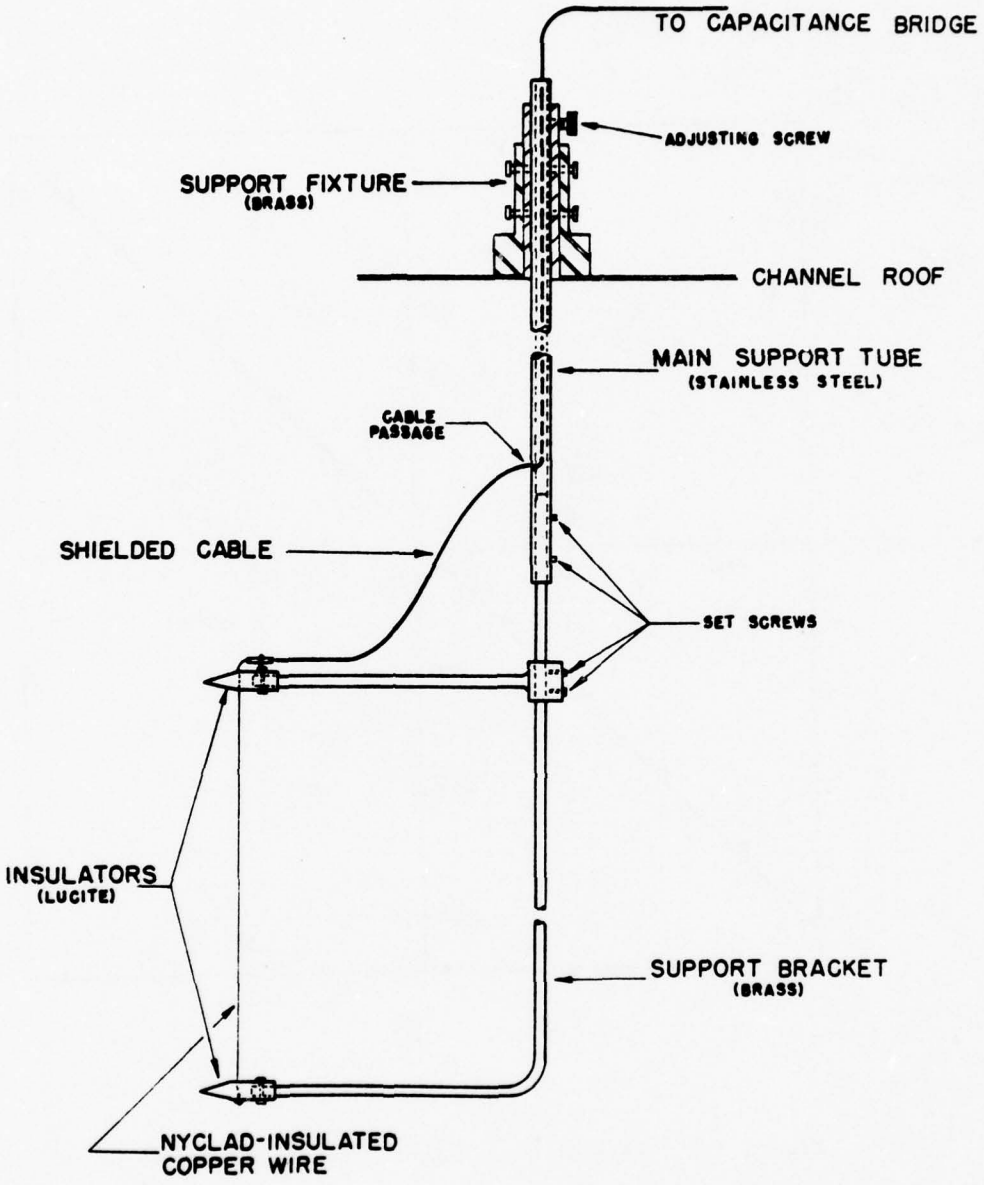


Figure 3.6 Capacitance Type Wave Gauge

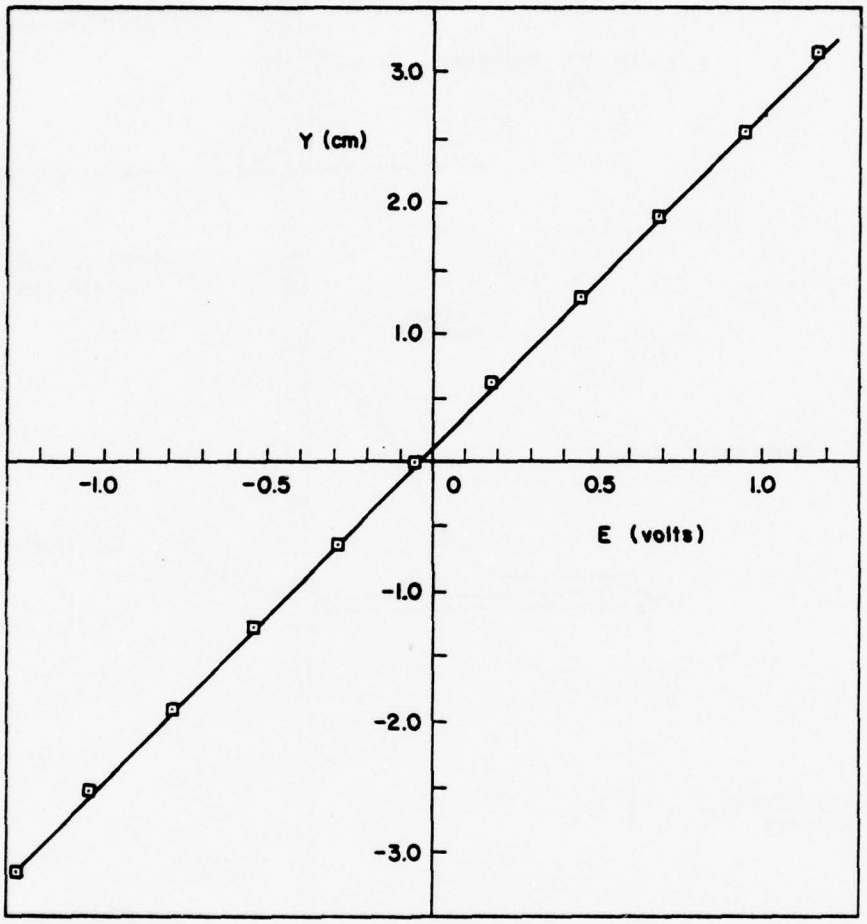


Figure 3.7 Typical Wave Height Gauge Calibration

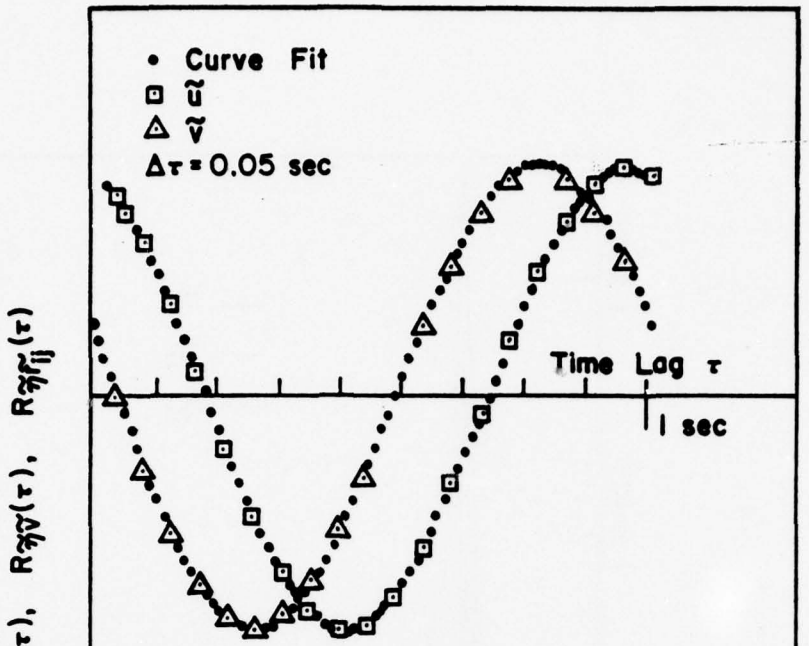


Figure 3.8a Typical Correlations of $R_{\eta\tilde{u}}(\tau)$ and $R_{\eta\tilde{v}}(\tau)$

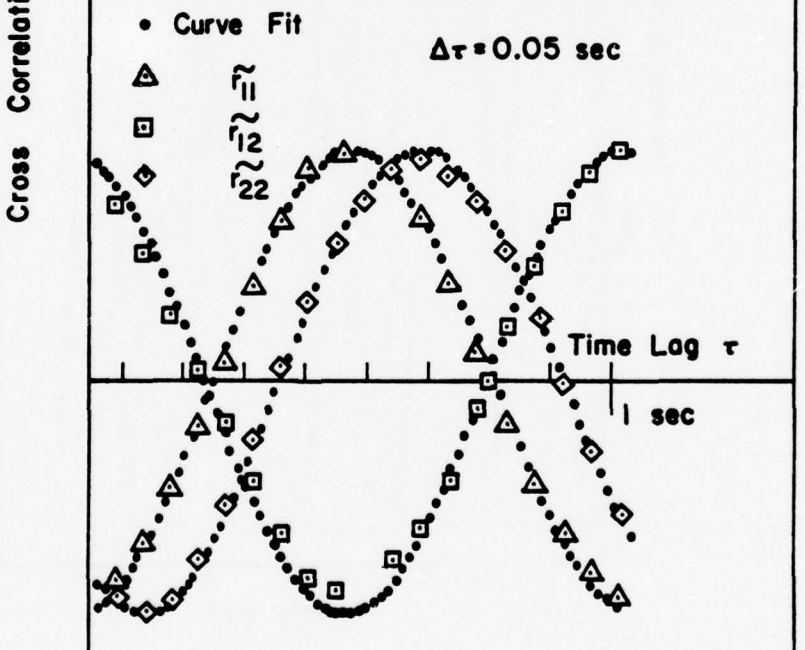


Figure 3.8b Typical Correlations of $R_{\eta\tilde{r}_{ij}}(\tau)$

Cross Correlation $R_{\eta\tilde{u}}(\tau)$, $R_{\eta\tilde{v}}(\tau)$, $R_{\eta\tilde{r}_{ij}}(\tau)$

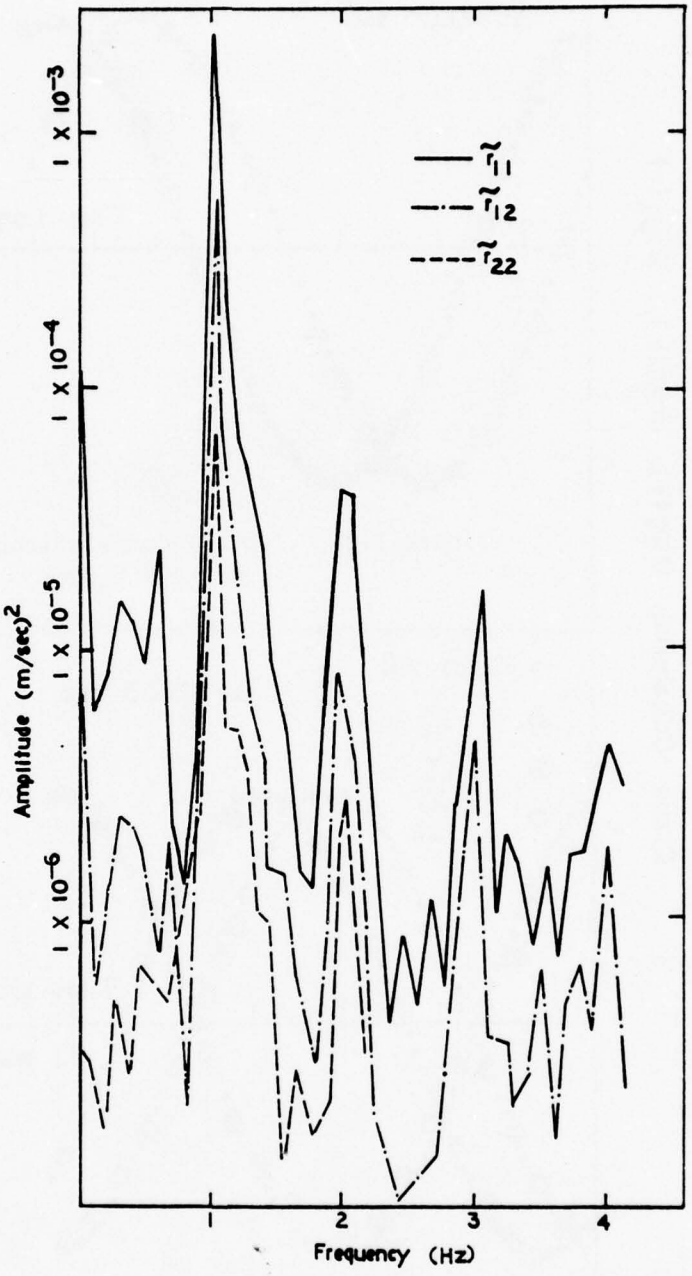


Figure 3.9 Typical Spectrum of $\tilde{r}_{ij}$

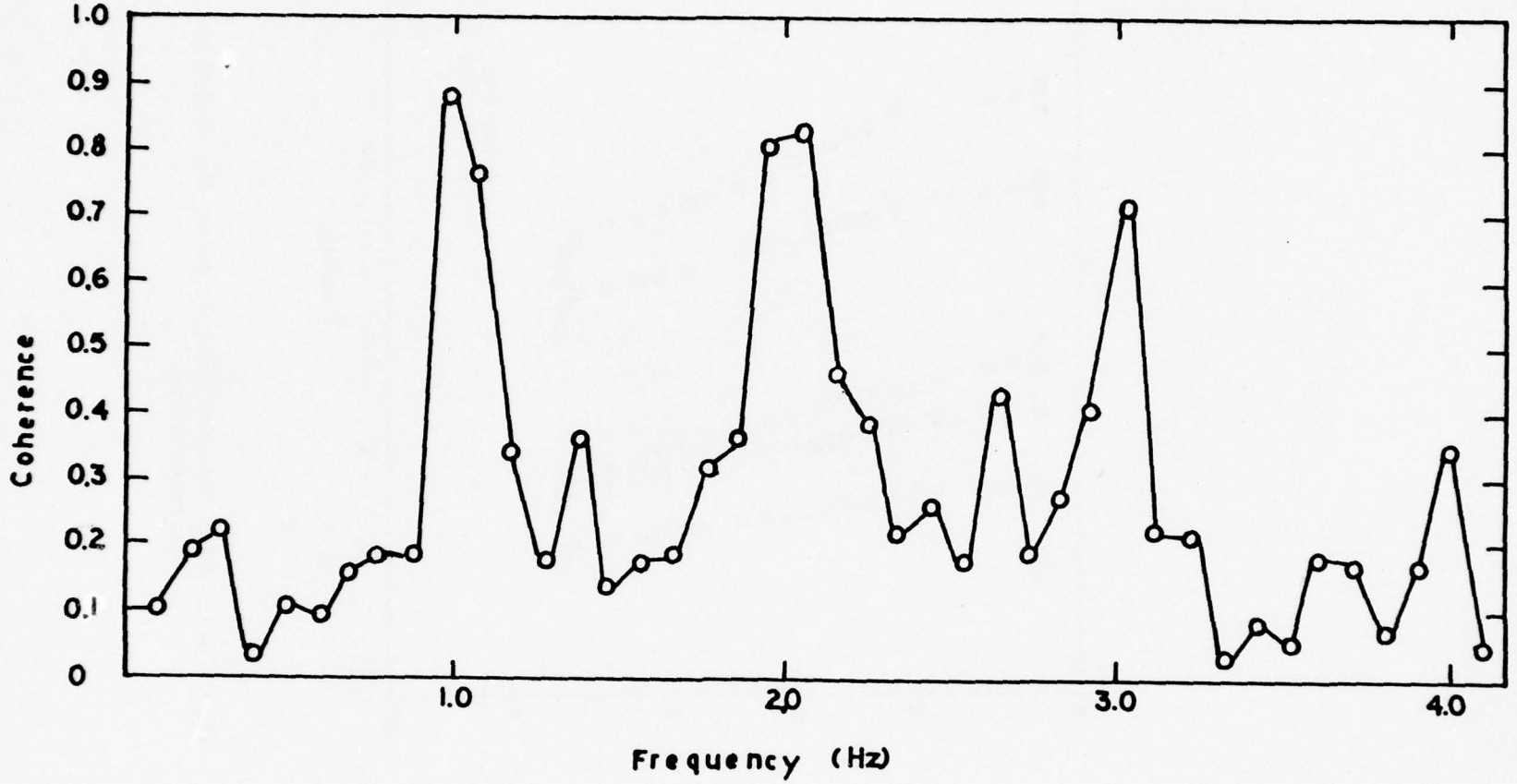


Figure 3.10 Typical Coherence Spectrum of $\tilde{r}_{22}$

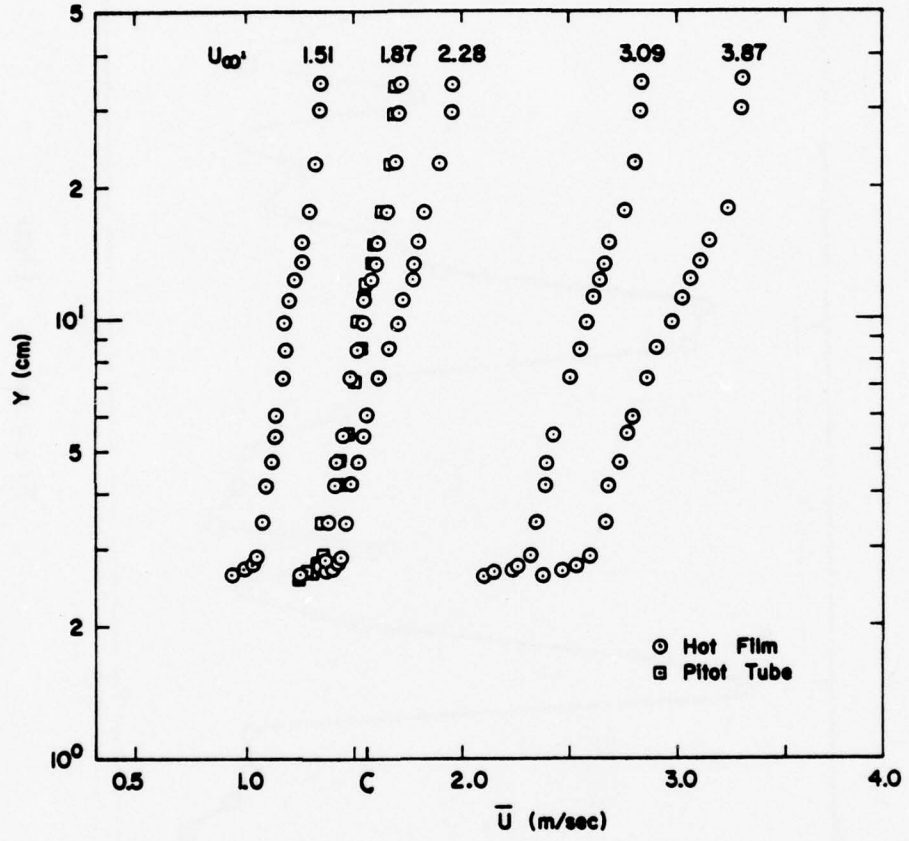


Figure 4.1 Mean Velocity Profile Above the Mechanically-Generated Waves

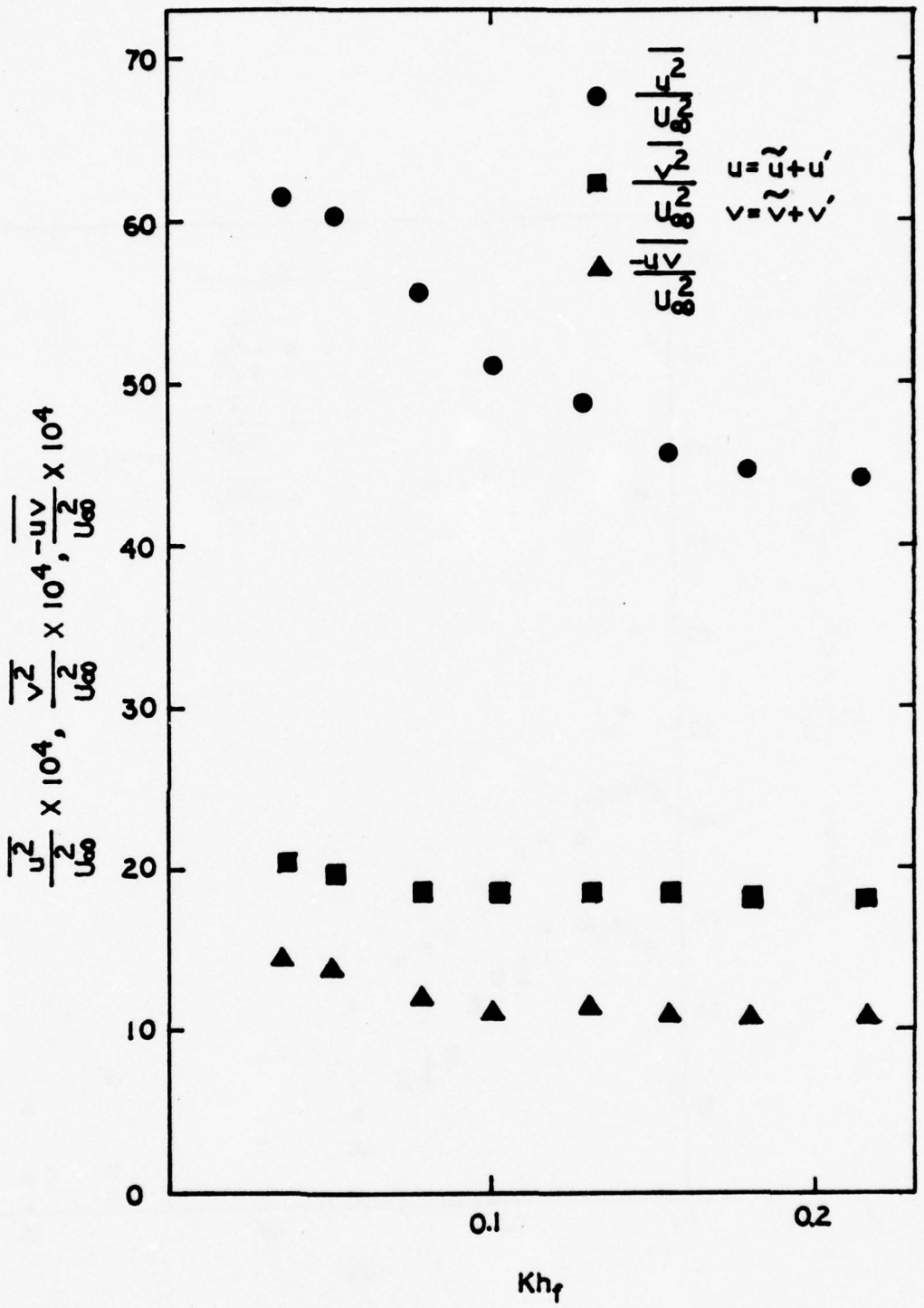


Figure 4.2a Turbulent Intensities and Reynolds Stress for $U_\infty/C = 1.115$ in Wave Following Reference Frame

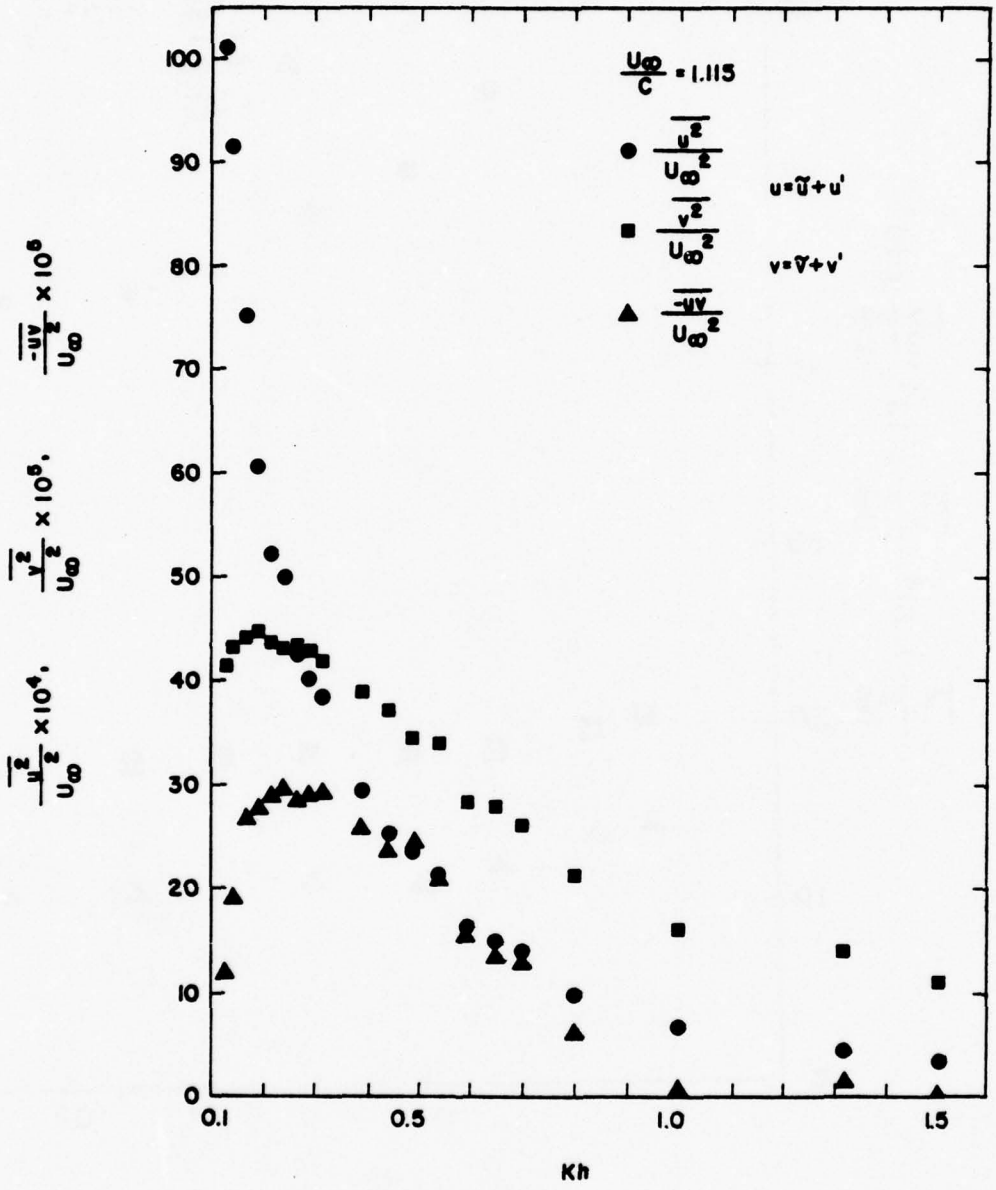


Figure 4.2b Turbulent Intensities and Reynolds Stress for $U_\infty/C = 1.115$ in Fixed Reference Frame

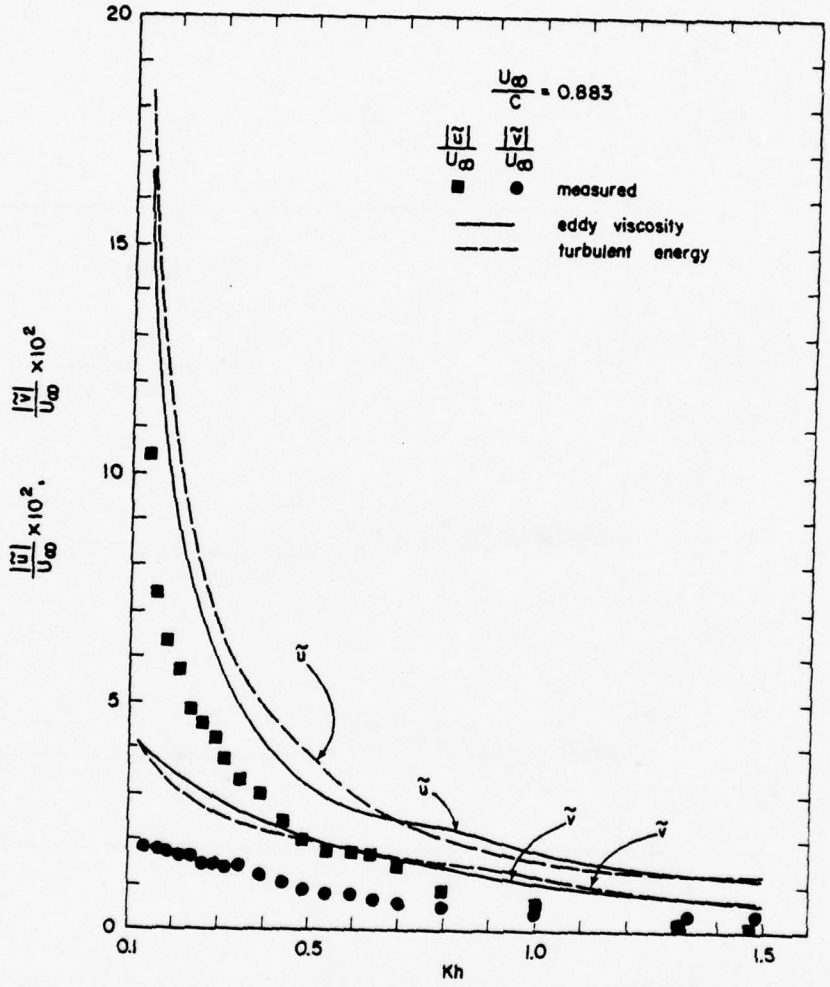


Figure 4.3 Magnitude Distributions of $\tilde{u}$ and $\tilde{v}$ and Computed Results for $U_\infty/C = 0.883$

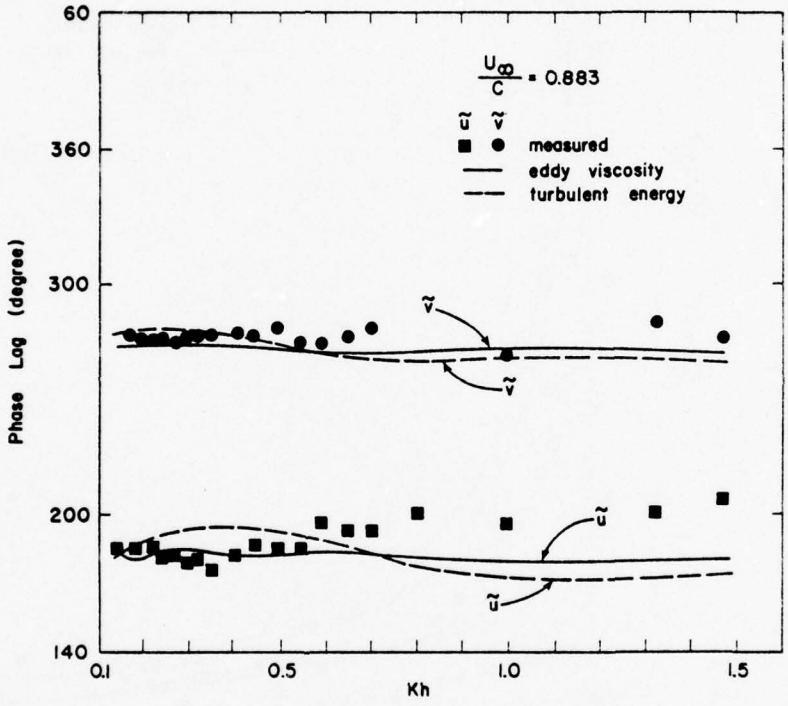


Figure 4.4 Phase Distributions of $\tilde{u}$ and $\tilde{v}$ and Computed Results for $U_\infty/C = 0.883$

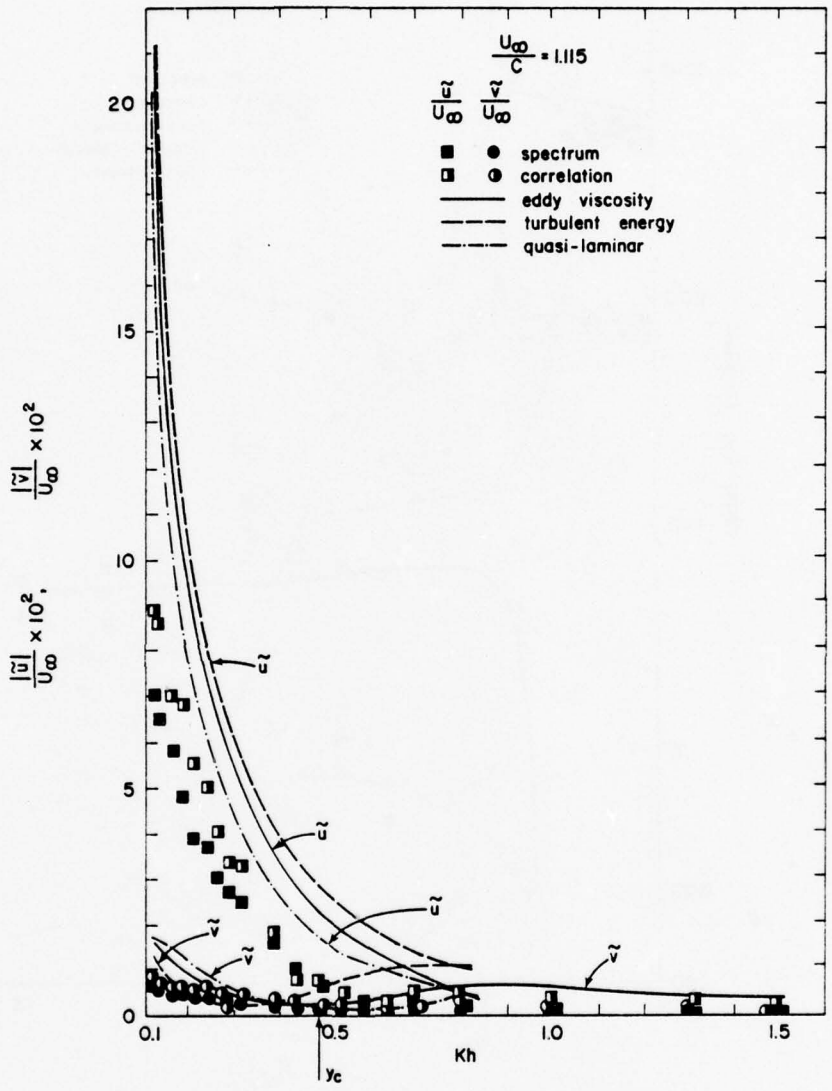


Figure 4.5 Magnitude Distributions of u and v and Computed Results for U_∞/C = 1.115

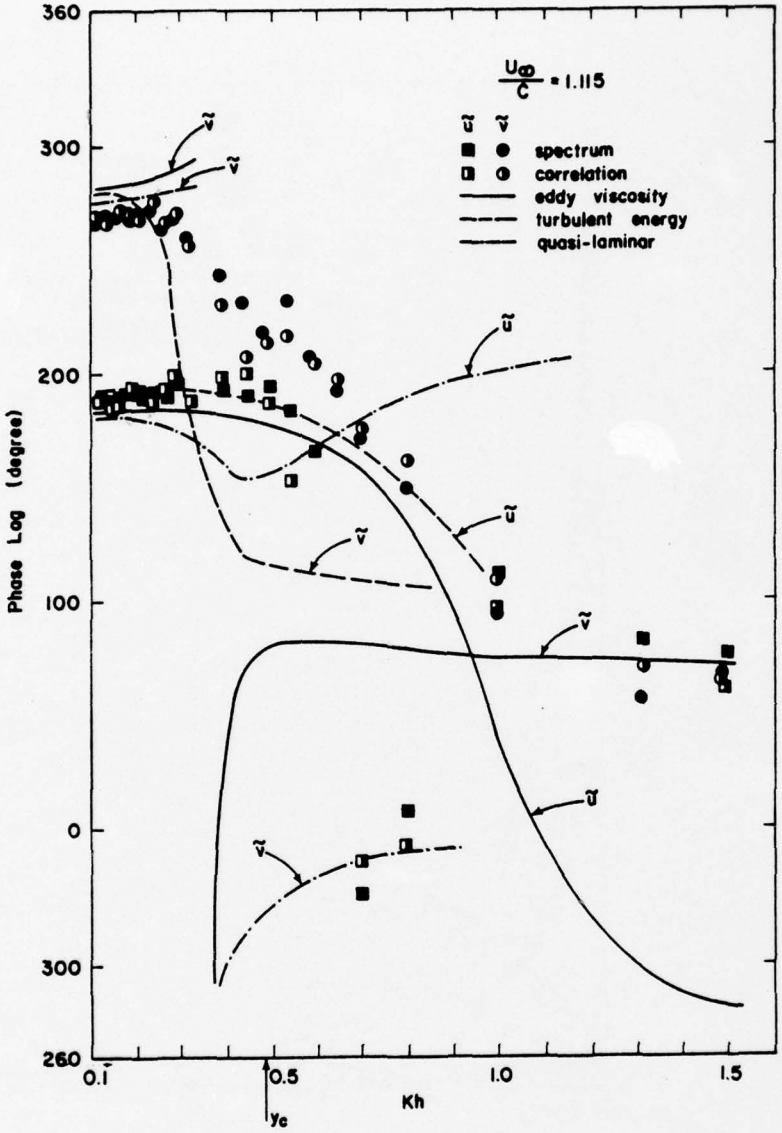


Figure 4.6 Phase Distributions of $\tilde{u}$ and $\tilde{v}$ and Computed Results for $U_\infty/C = 1.115$

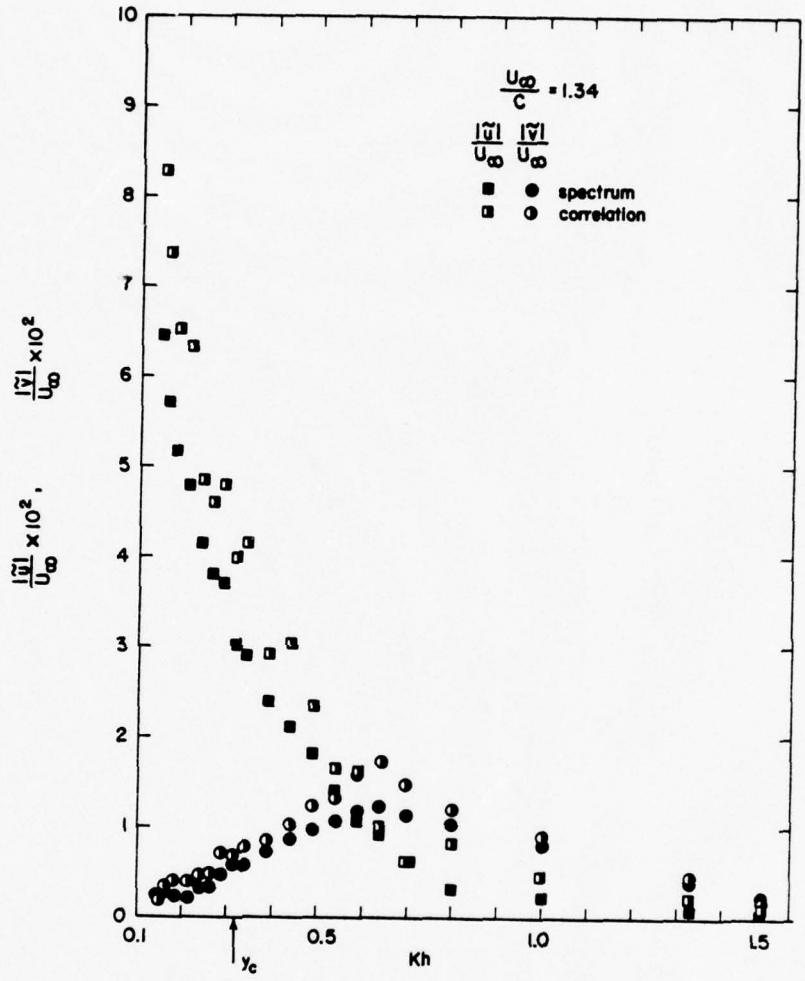


Figure 4.7 Magnitude Distributions of $\tilde{u}$ and $\tilde{v}$ for $U_\infty/C = 1.34$

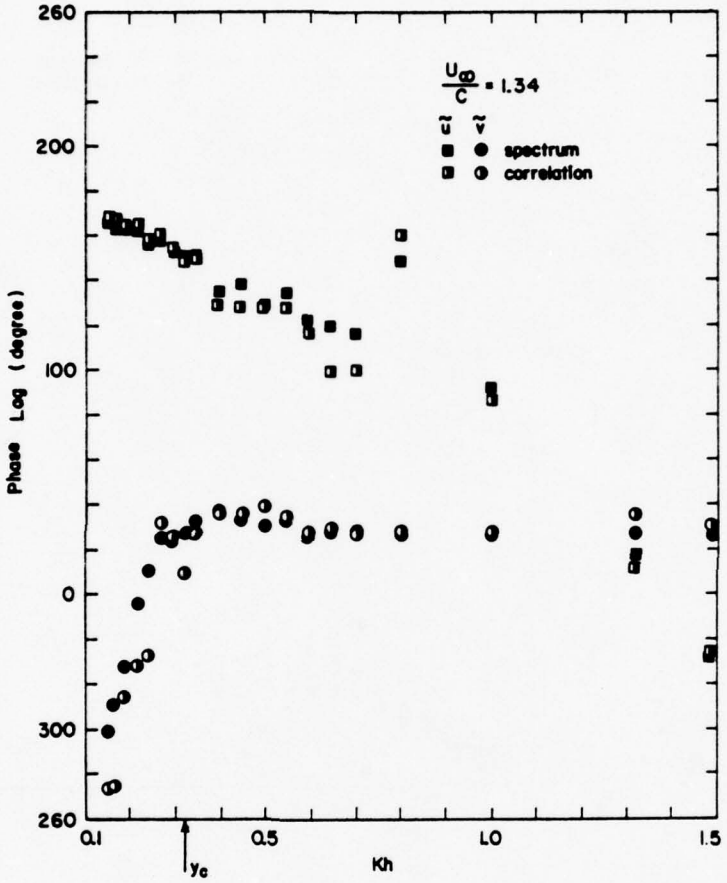


Figure 4.8 Phase Distributions of $\tilde{u}$ and $\tilde{v}$ for $U_\infty/C = 1.34$

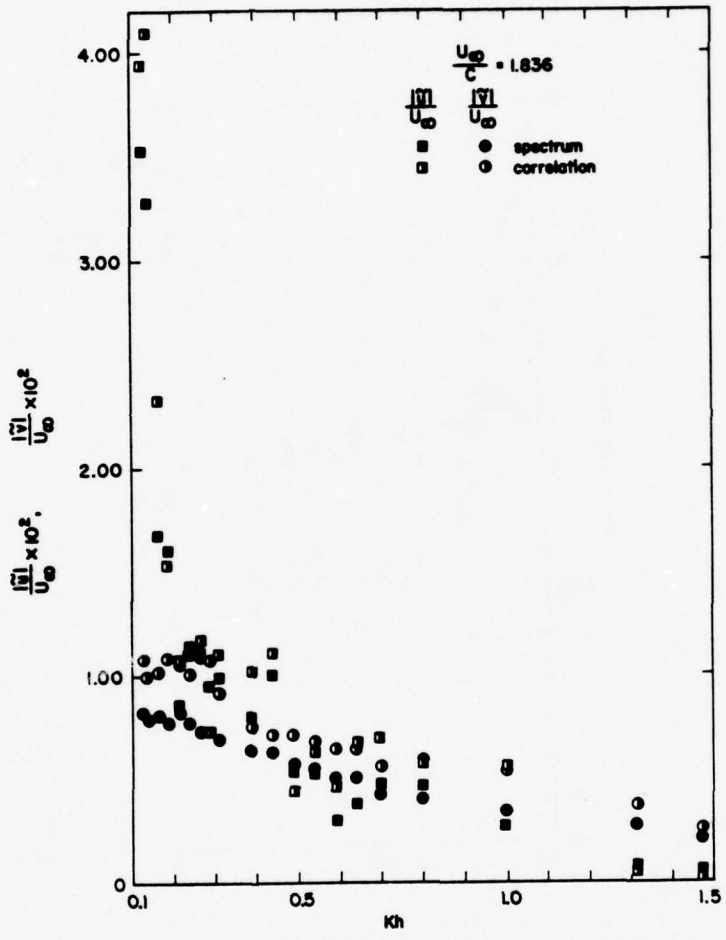


Figure 4.9 Magnitude Distributions of $\tilde{u}$ and $\tilde{v}$ for $U_\infty/C = 1.836$

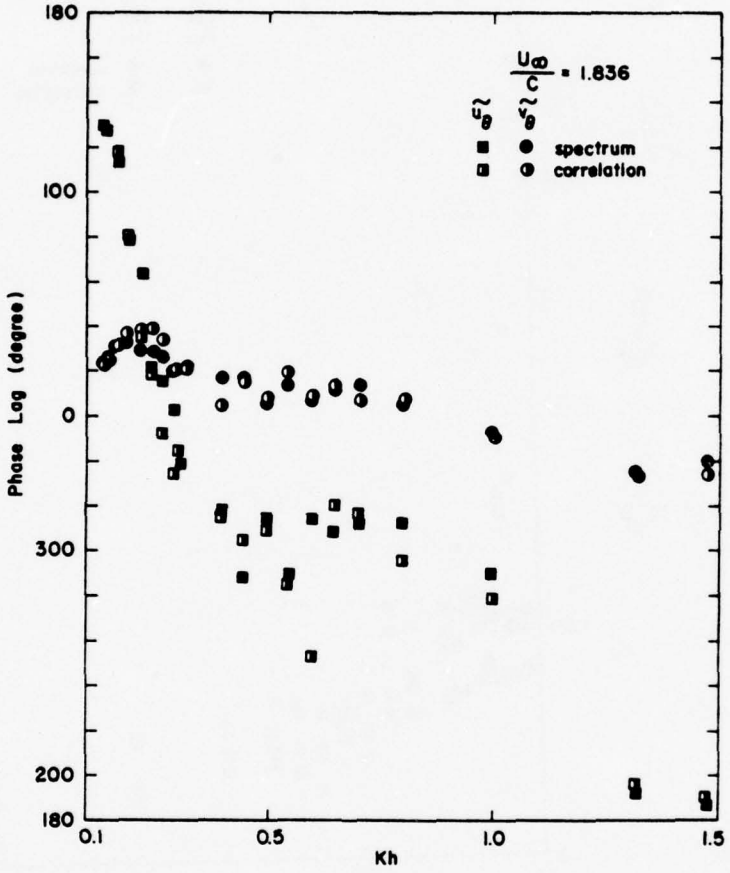


Figure 4.10 Phase Distributions of $\tilde{u}$ and $\tilde{v}$ for $U_\infty/C = 1.836$

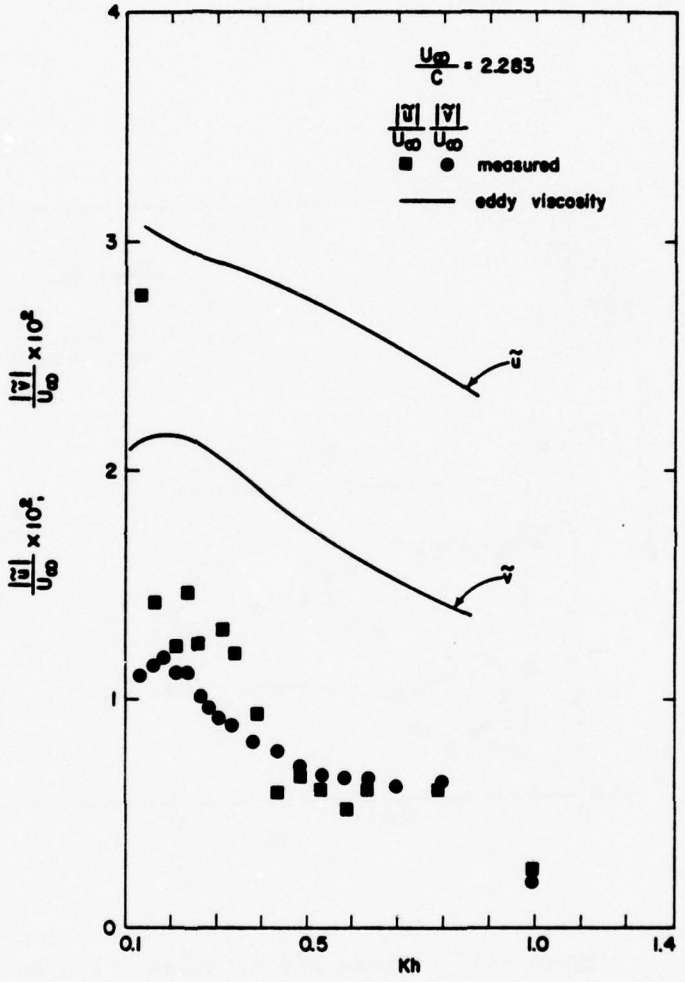


Figure 4.11 Magnitude Distributions of $\tilde{u}$ and $\tilde{v}$ and Computed Results for $U_\infty/C = 2.283$

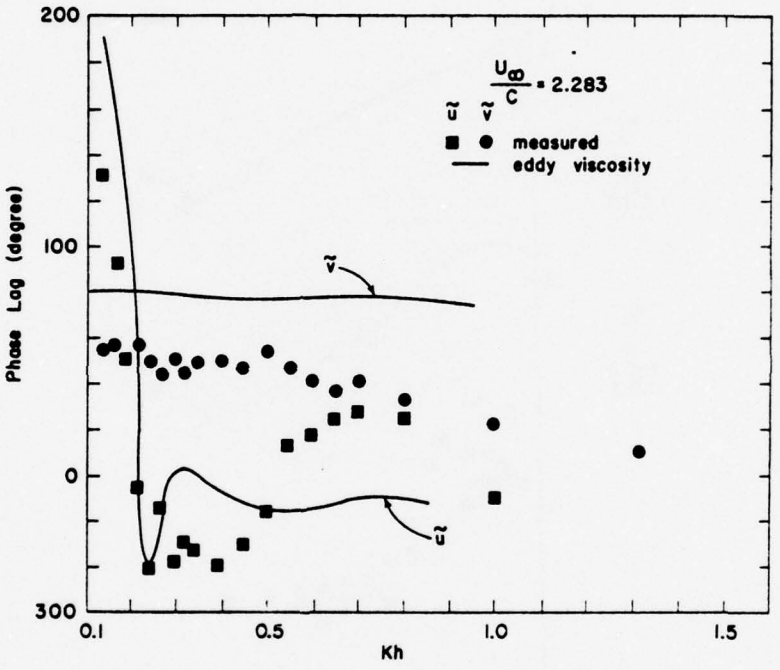


Figure 4.12 Phase Distributions of $\tilde{u}$ and $\tilde{v}$ and Computed Results for $U_\infty/C = 2.283$

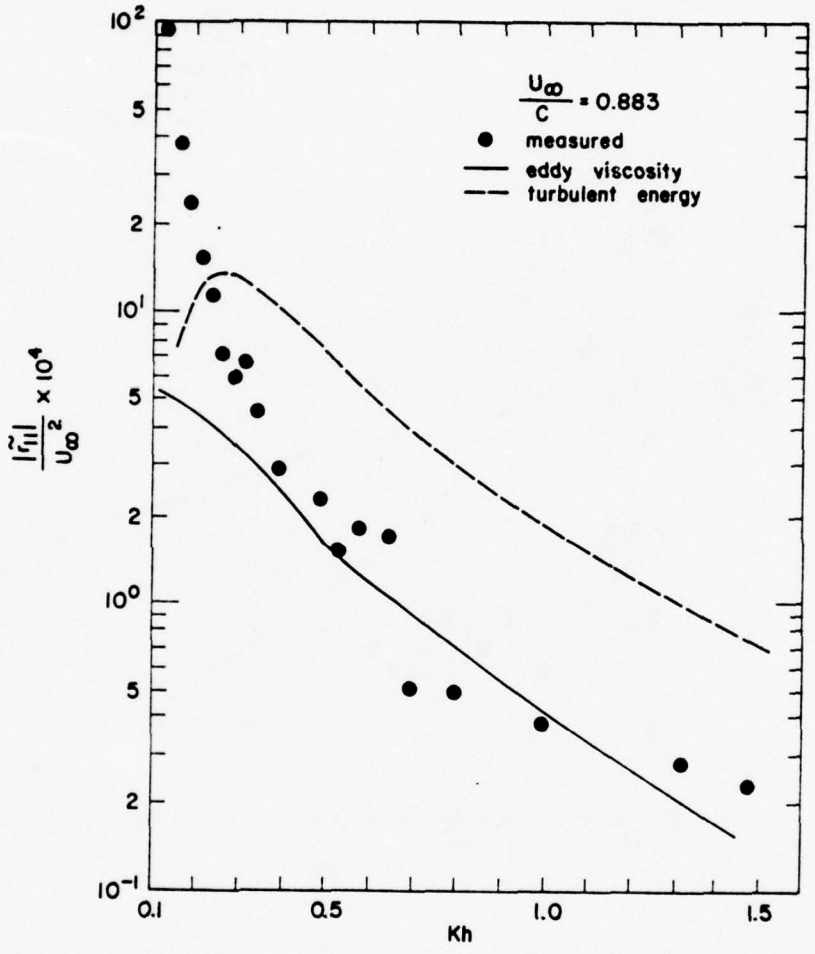


Figure 4.13a Magnitude Distribution of $\tilde{r}_{11}$ and Computed Results for $U_\infty/C = 0.883$

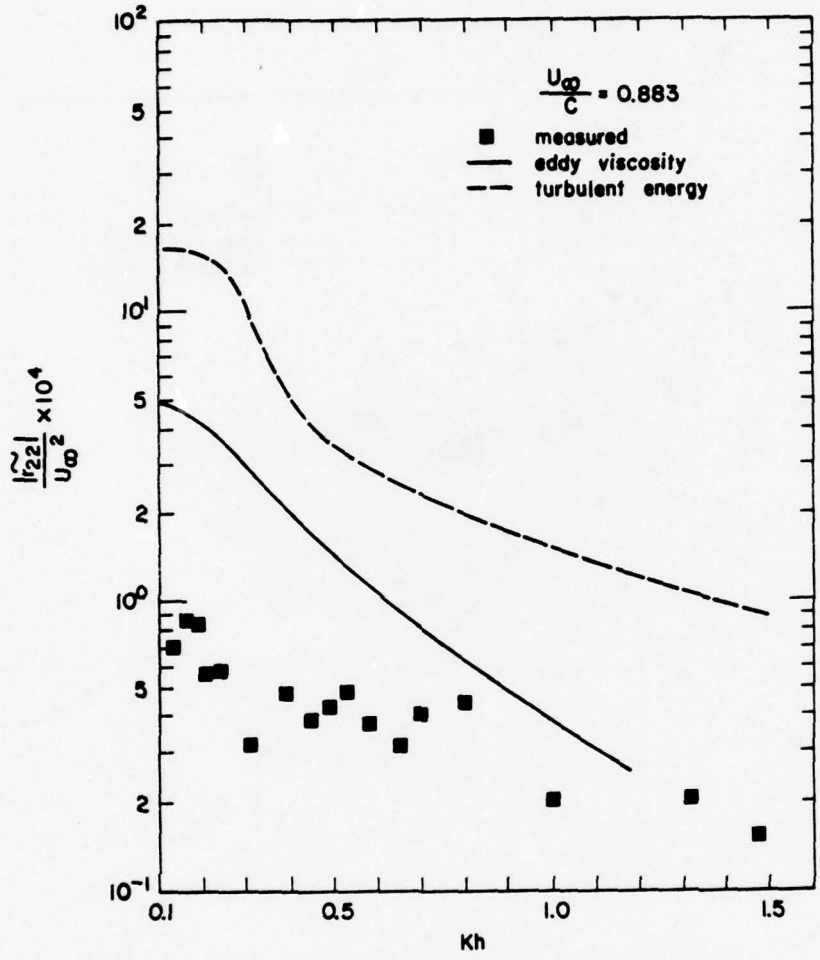


Figure 4.13b Magnitude Distribution of $\tilde{r}_{22}$ and Computed Results for $U_\infty/C = 0.883$

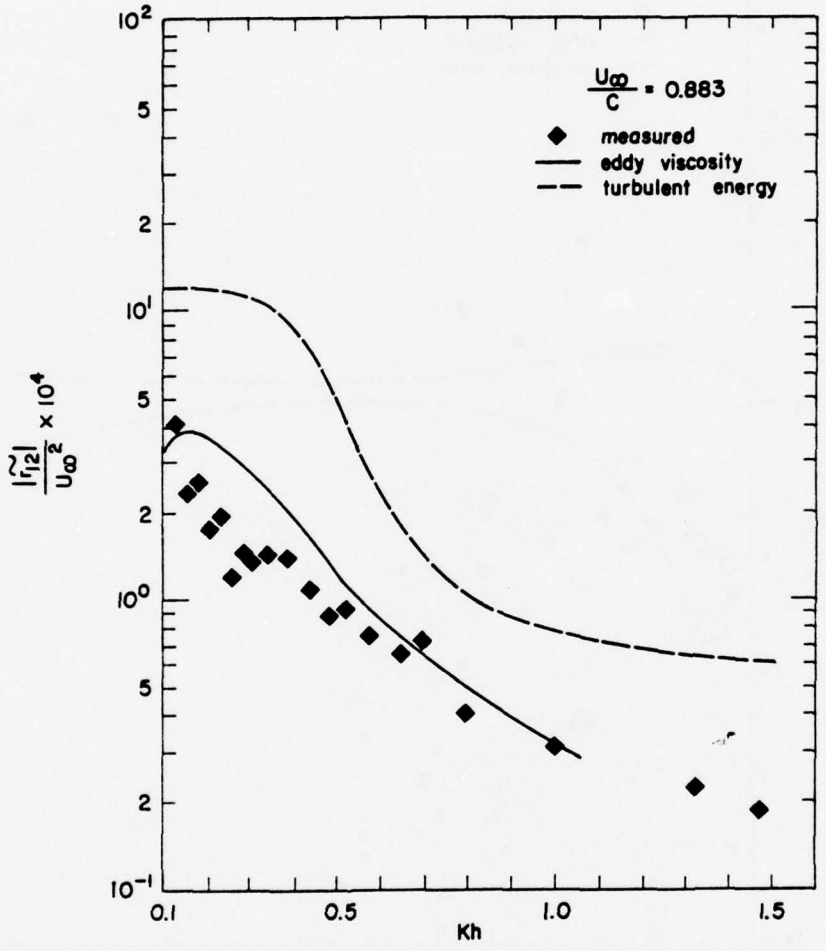


Figure 4. 13c Magnitude Distribution of $\tilde{r}_{12}$ and Computed Results for $U_\infty/C = 0.883$

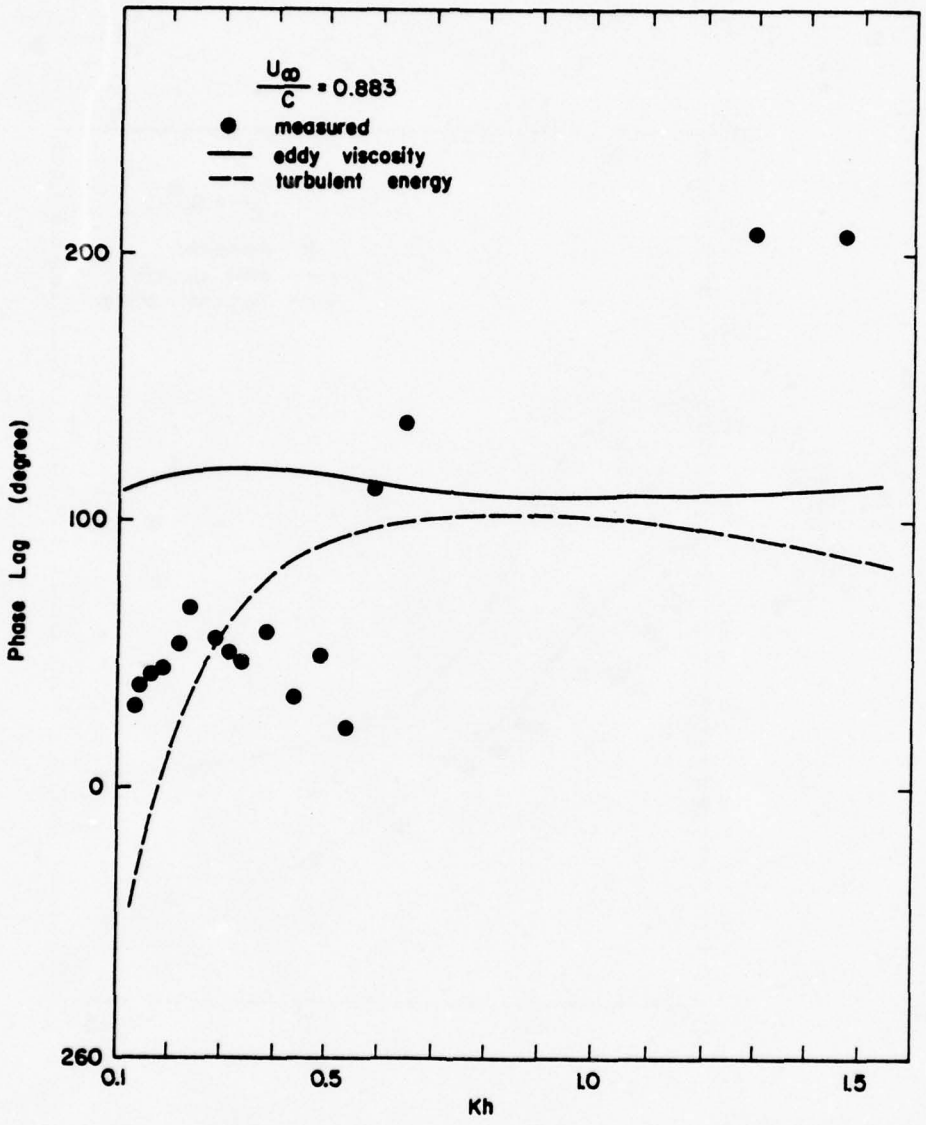


Figure 4.14a Phase Distribution of $\tilde{r}_{11}$ and Computed Results for $U_\infty/C = 0.883$

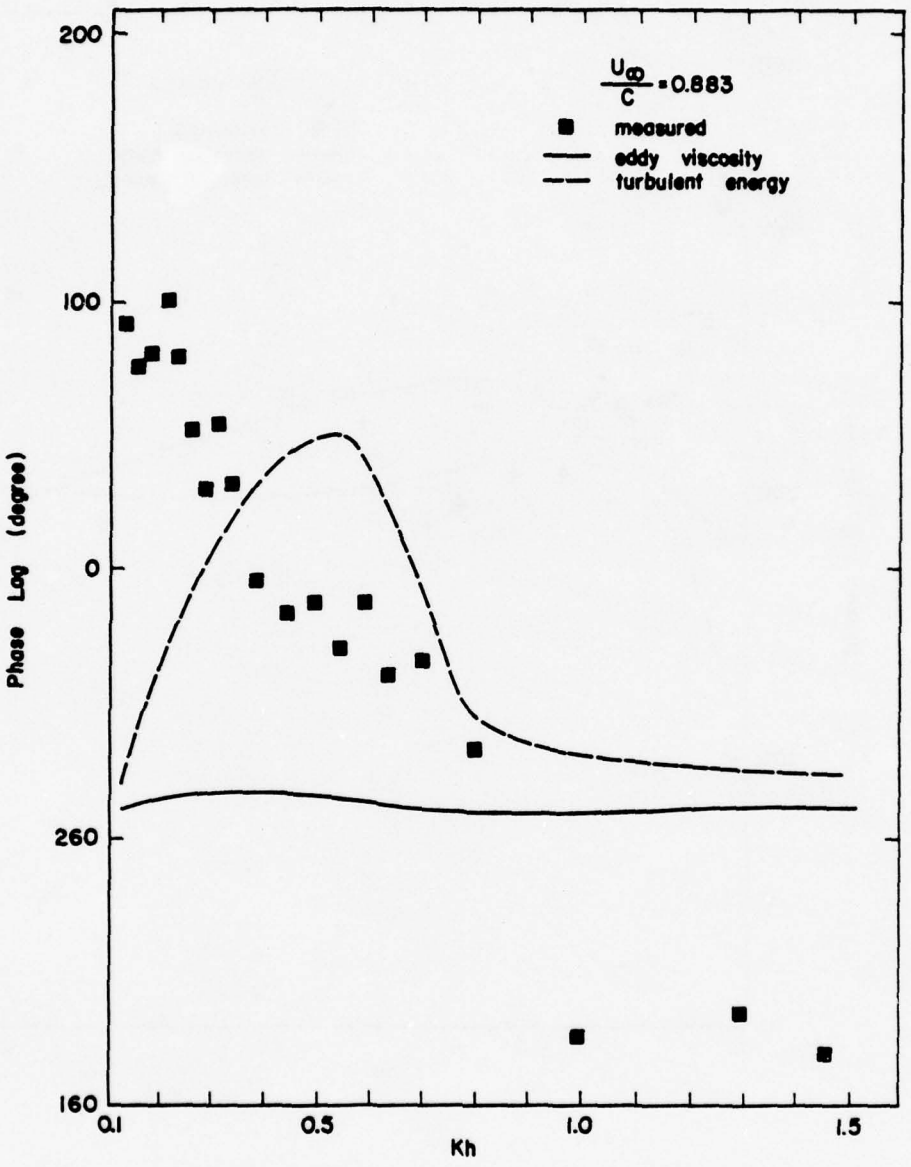


Figure 4.14b Phase Distribution of $\tilde{r}_{22}$ and Computed Results for $U_\infty/C = 0.883$

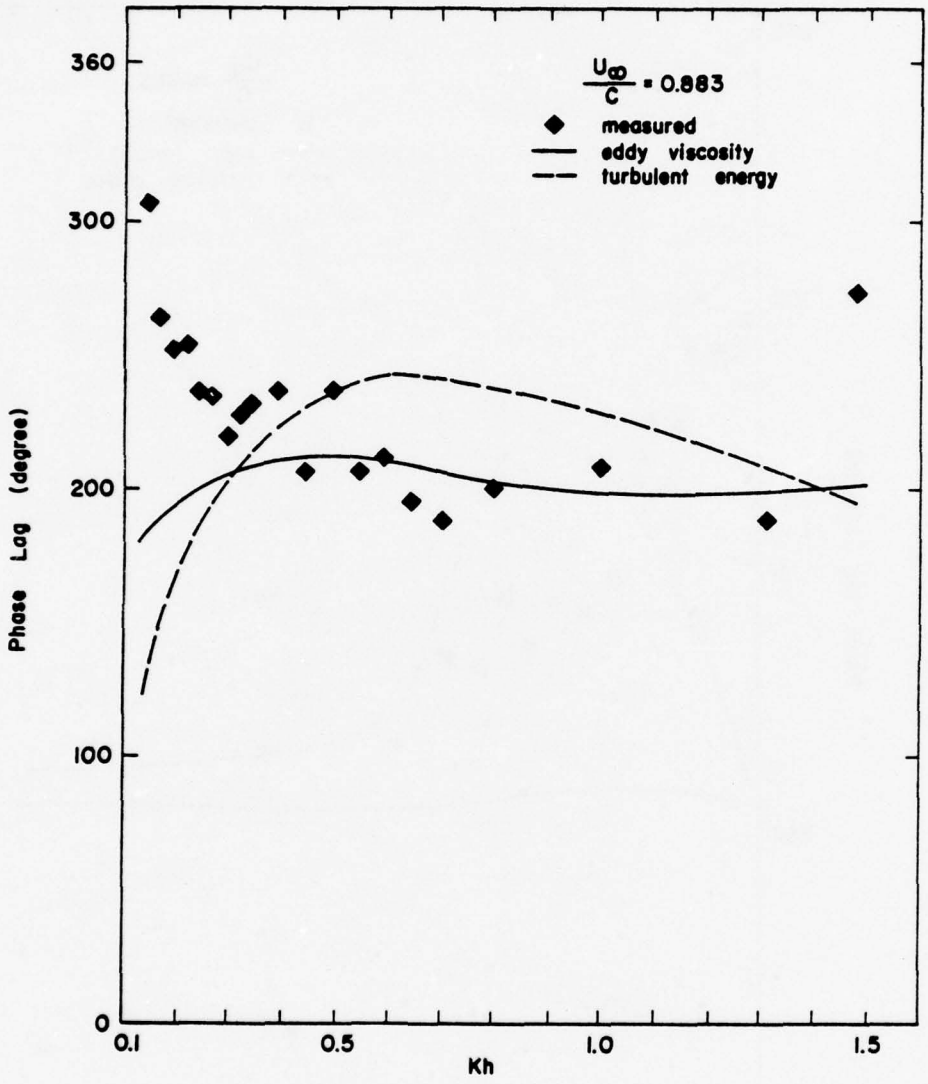


Figure 4.14c Phase Distribution of $\tilde{r}_{12}$ and Computed Results for $U_\infty/C = 0.883$

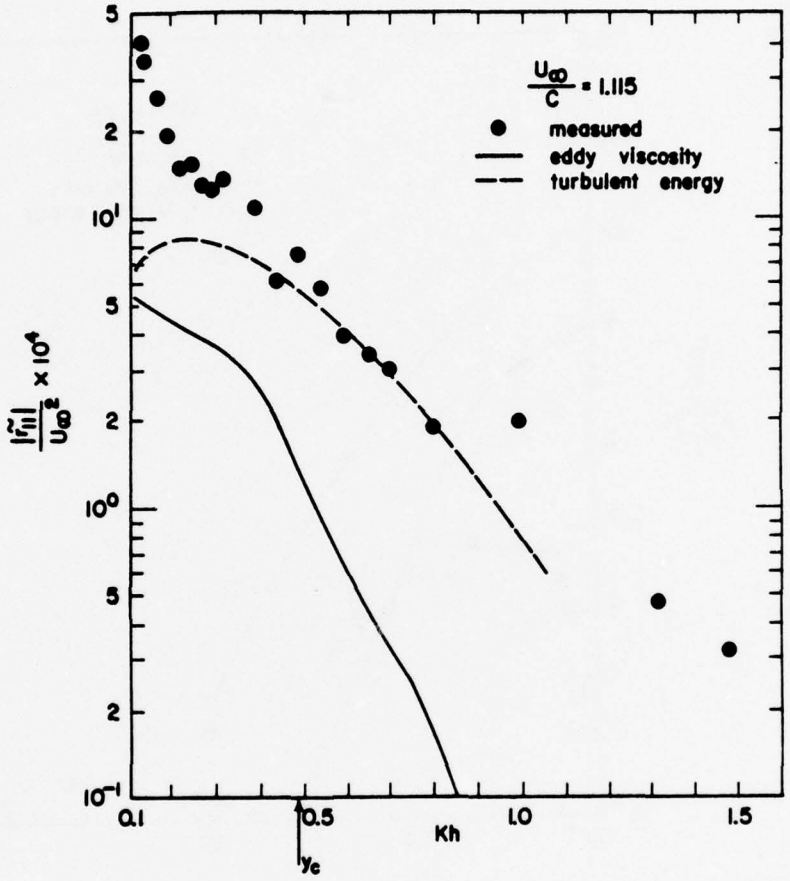


Figure 4.15a Magnitude Distribution of $\tilde{r}_{11}$ and Computed Results for $U_\infty/C = 1.115$

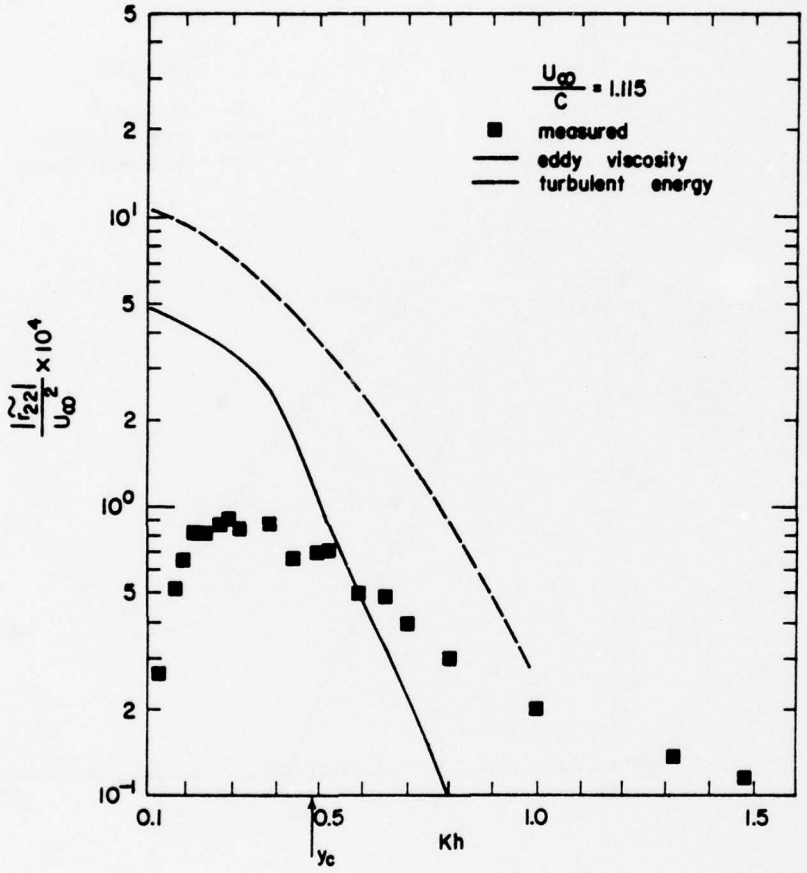


Figure 4.15b Magnitude Distribution of $\tilde{r}_{22}$ and Computed Results for $U_\infty/C = 1.115$

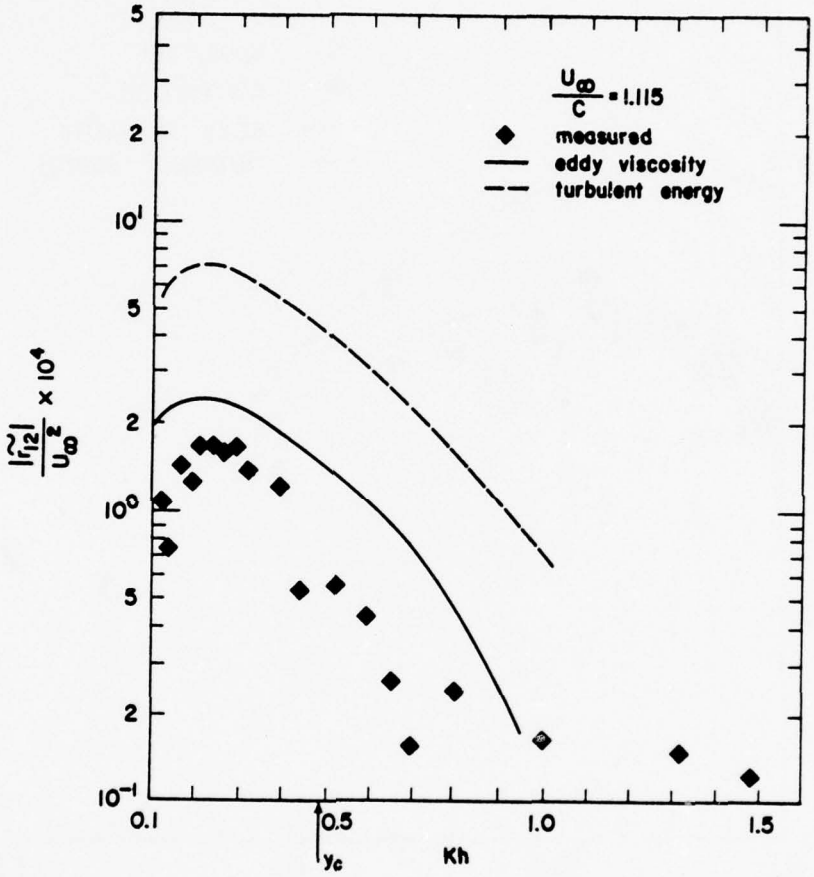


Figure 4.15c Magnitude Distribution of $\tilde{r}_{12}$ and Computed Results for $U_\infty/C = 1.115$

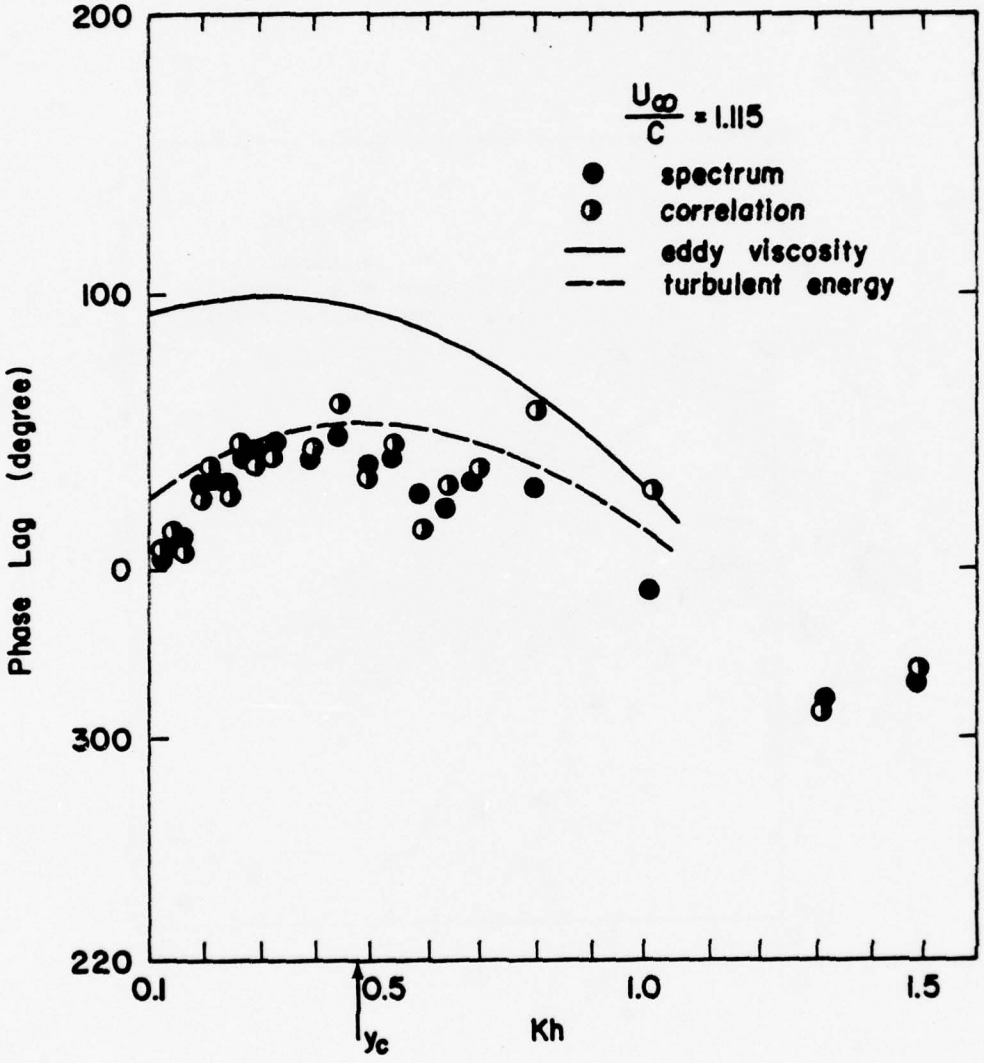


Figure 4.16a Phase Distribution of $\tilde{r}_{11}$ and Computed Results for $U_\infty/C = 1.115$

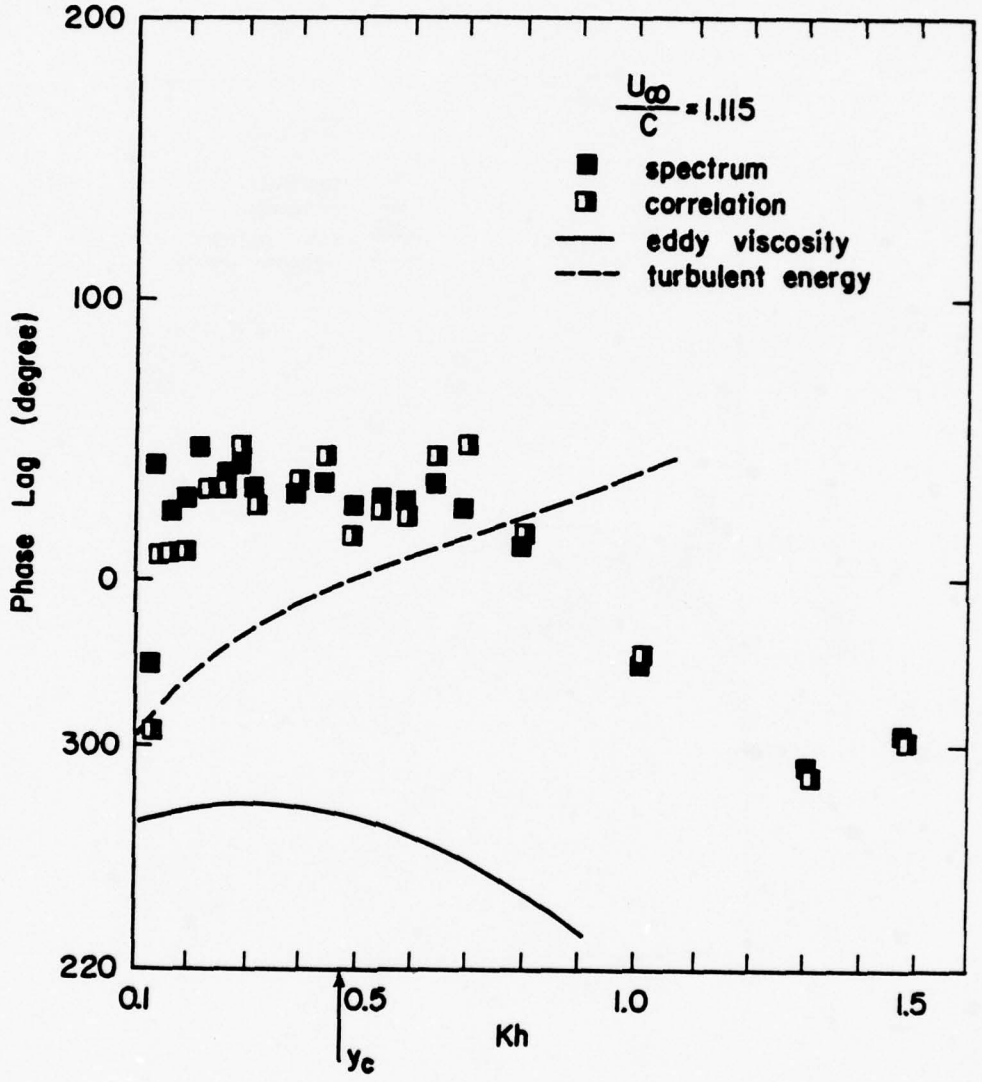


Figure 4.16b Phase Distribution of $\tilde{r}_{22}$ and Computed Results for $U_\infty/C = 1.115$

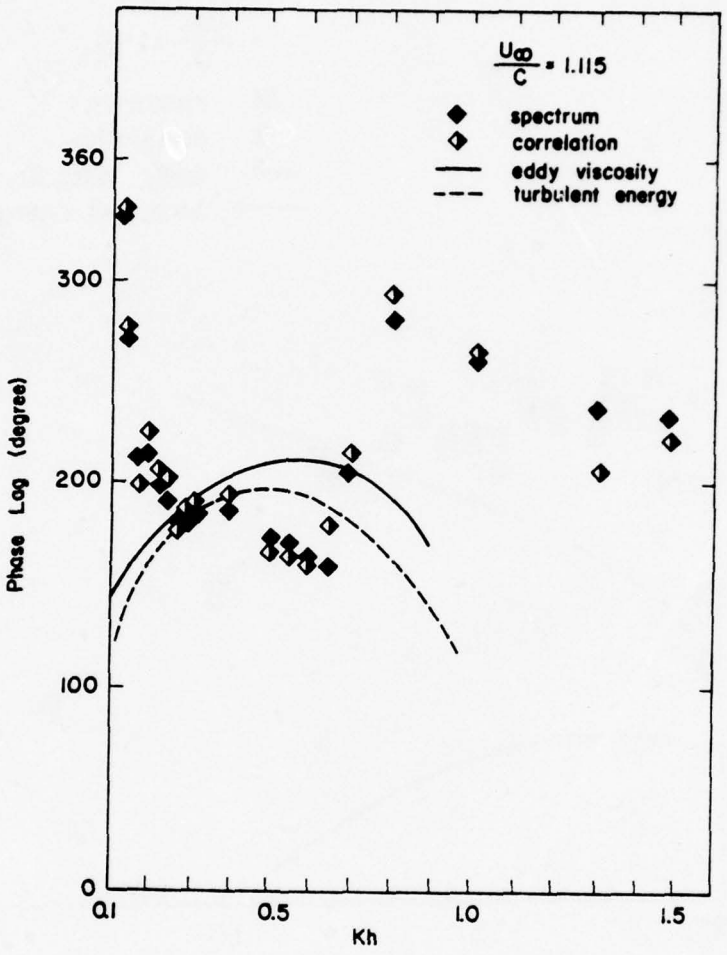


Figure 4.16c Phase Distribution of $\tilde{r}_{12}$ and Computed Results for $U_\infty/C = 1.115$

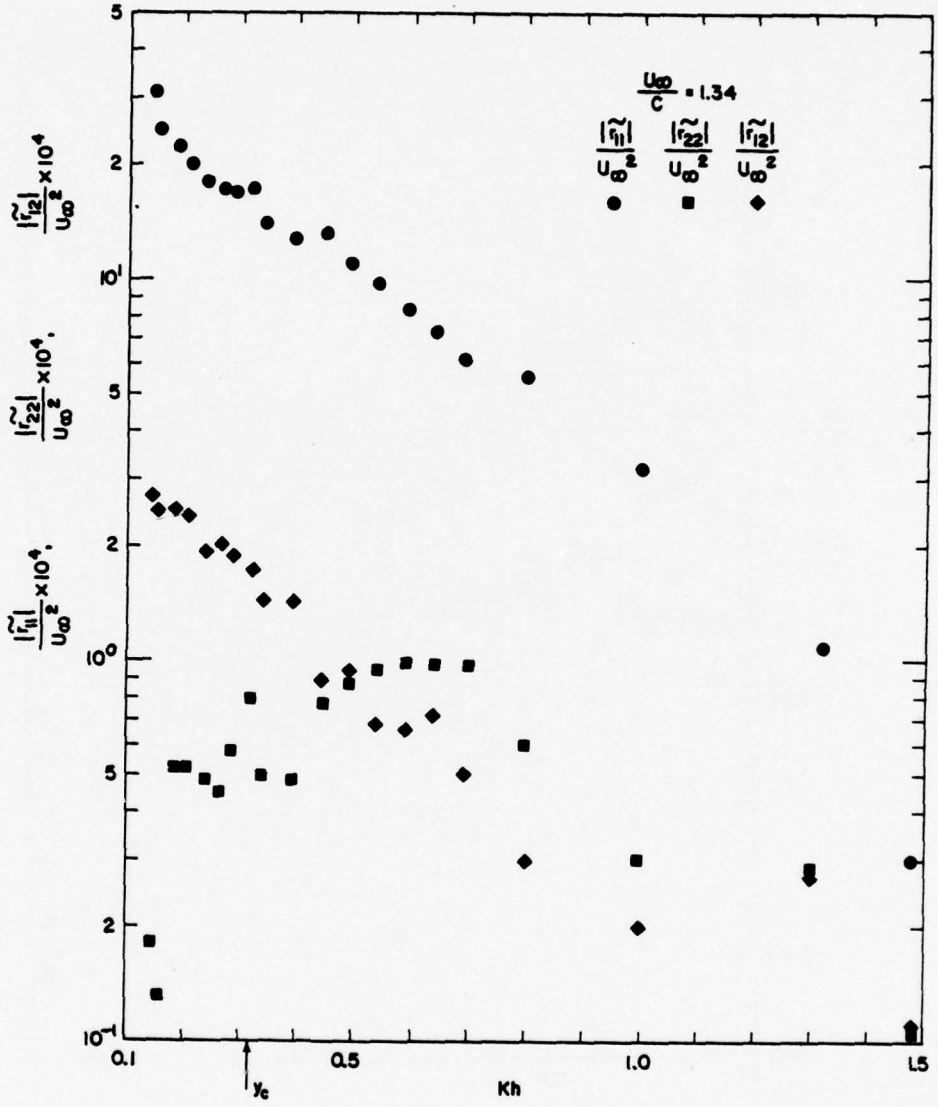


Figure 4.17 Magnitude Distributions of $\tilde{r}_{ij}$ for $U_\infty/C = 1.34$

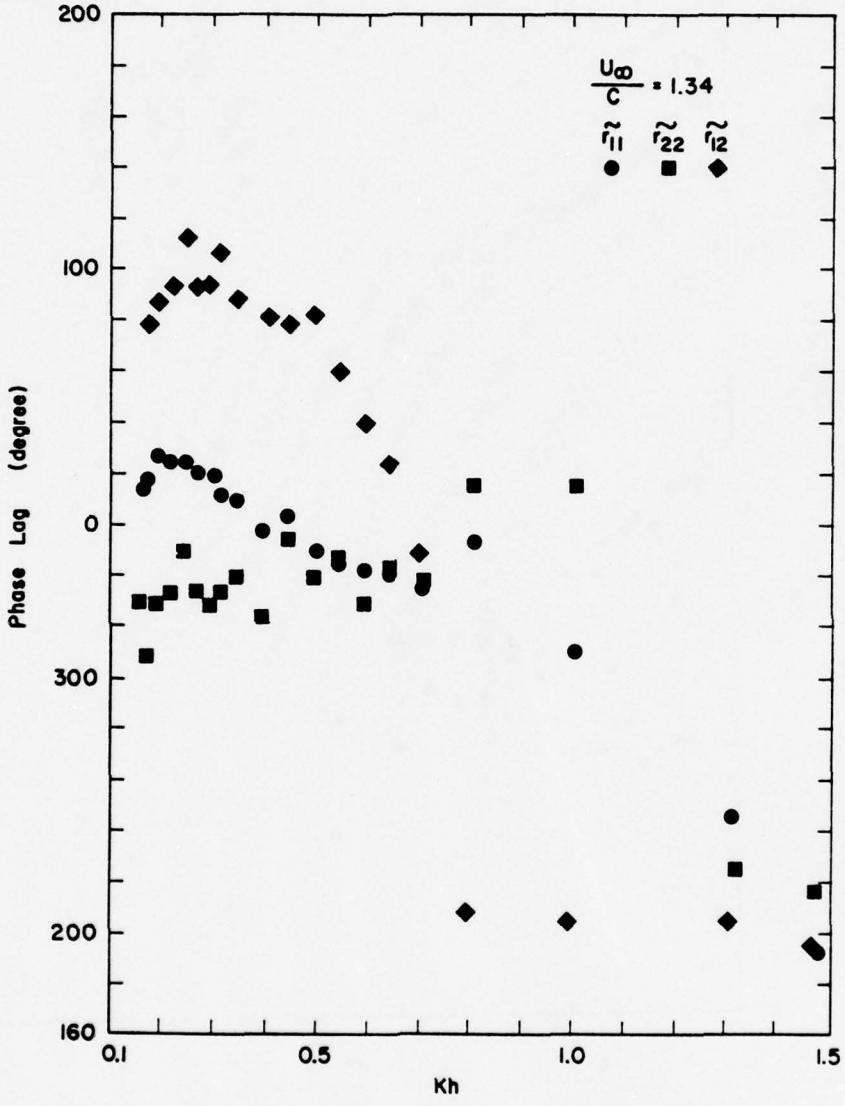


Figure 4.18 Phase Distributions of $\tilde{r}_{ij}$ for $U_\infty/C = 1.34$

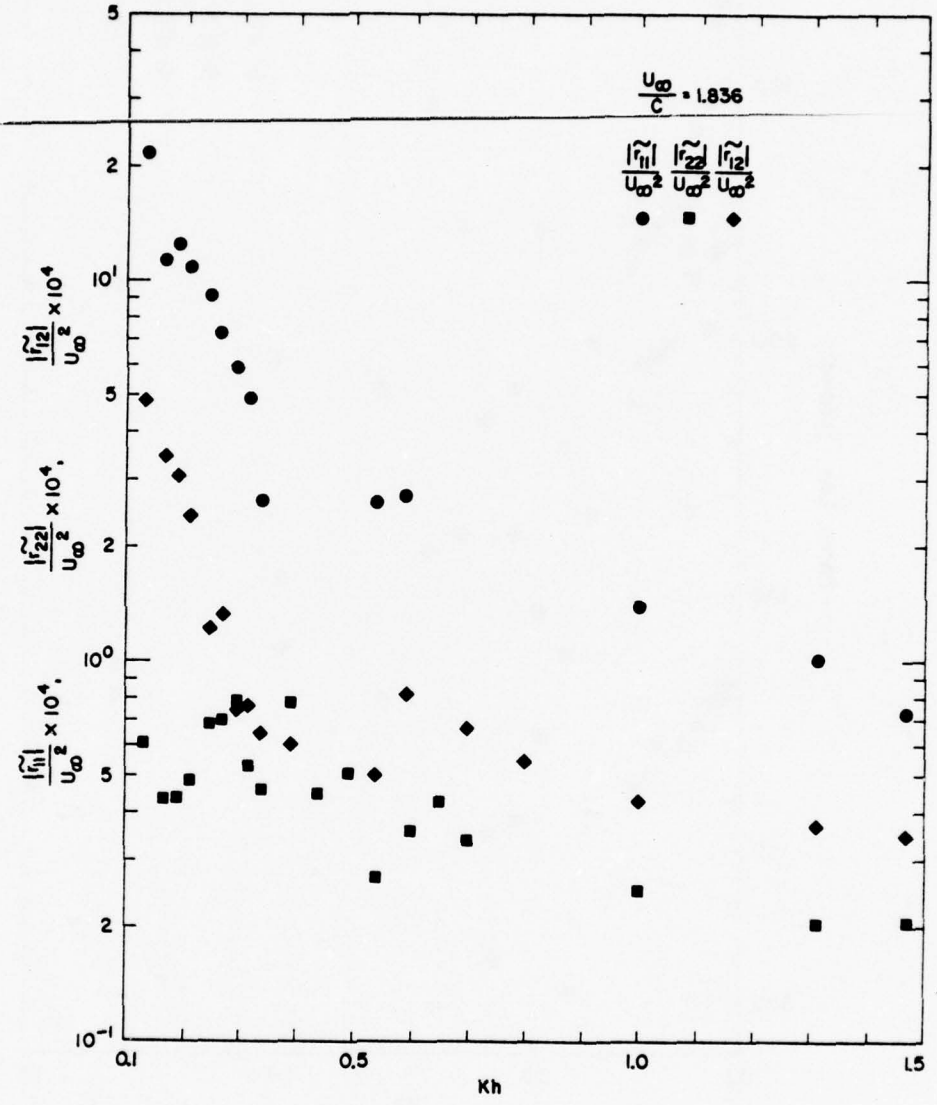


Figure 4.19 Magnitude Distributions of $\tilde{r}_{ij}$ for $U_\infty/C = 1.836$

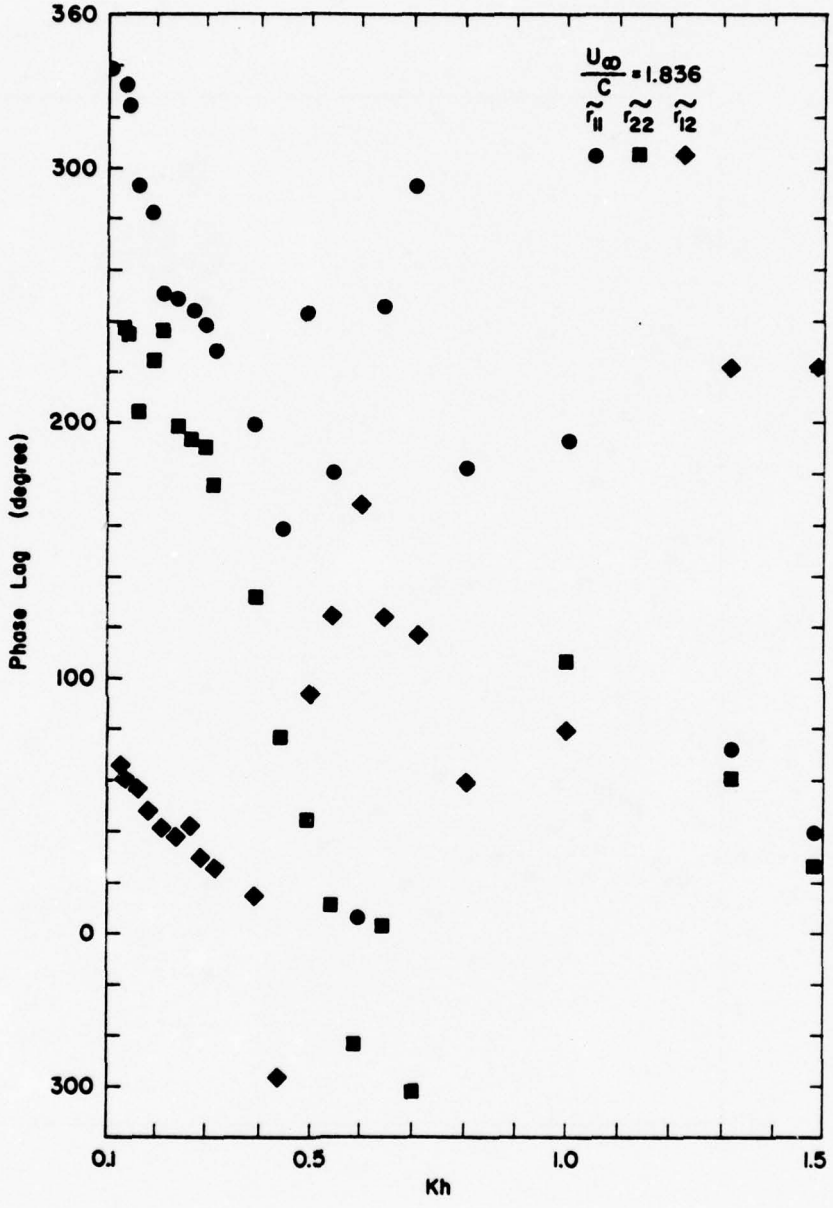


Figure 4.20 Phase Distributions of $\tilde{r}_{ij}$ for $U_\infty/C = 1.836$

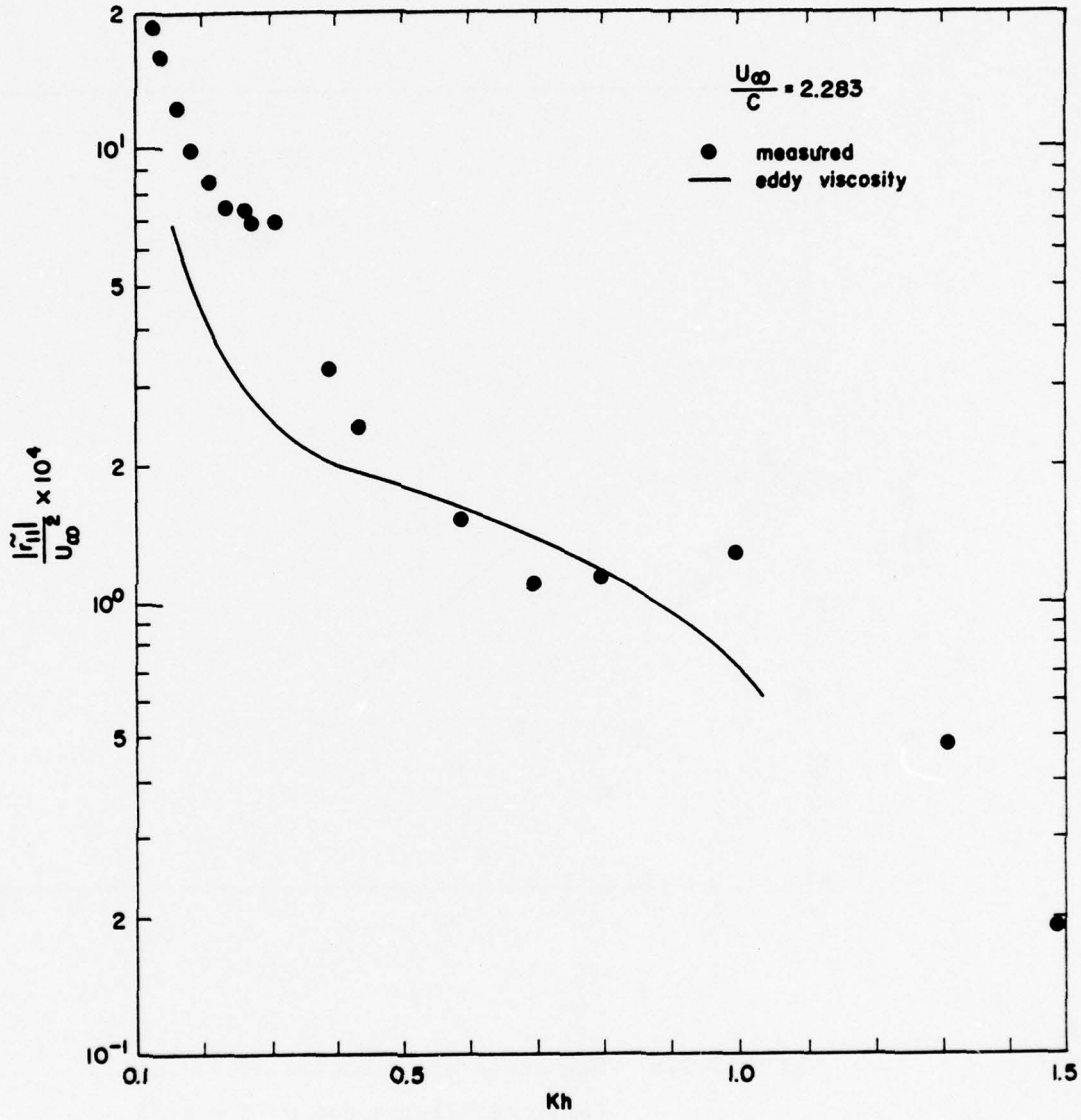


Figure 4.21a Magnitude Distribution of $\tilde{r}_{11}$ and Computed Results for $U_\infty/C = 2.283$

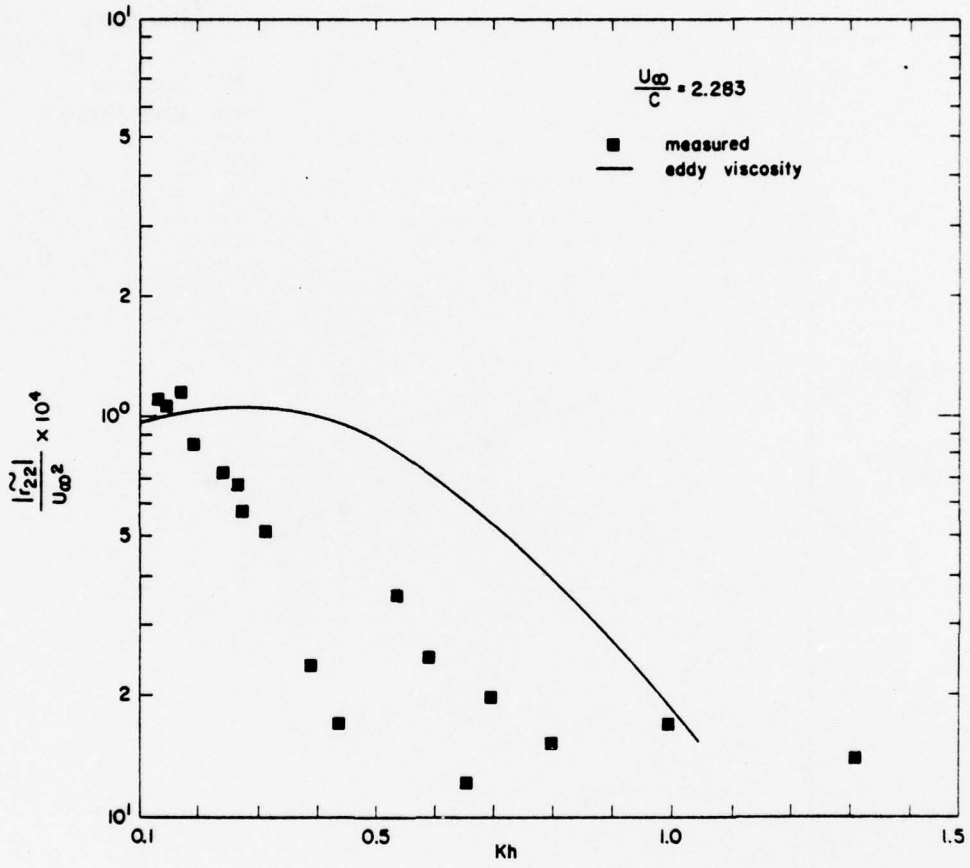


Figure 4.21b Magnitude Distribution of $\tilde{r}_{22}$ and Computed Results for $U_\infty/C = 2.283$

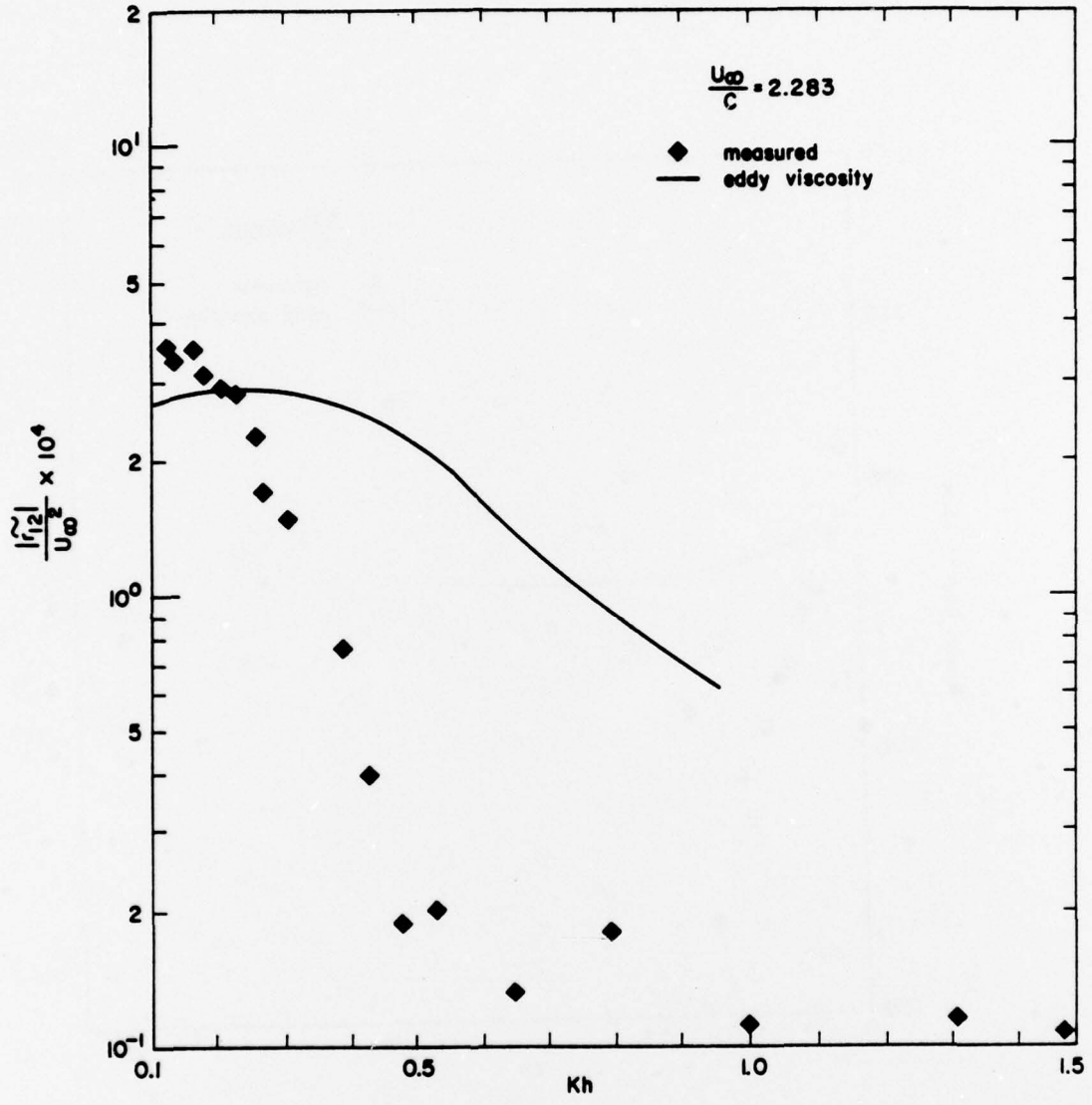


Figure 4.21c Magnitude Distribution of $\tilde{r}_{12}$ and Computed Results for $U_\infty/C = 2.283$

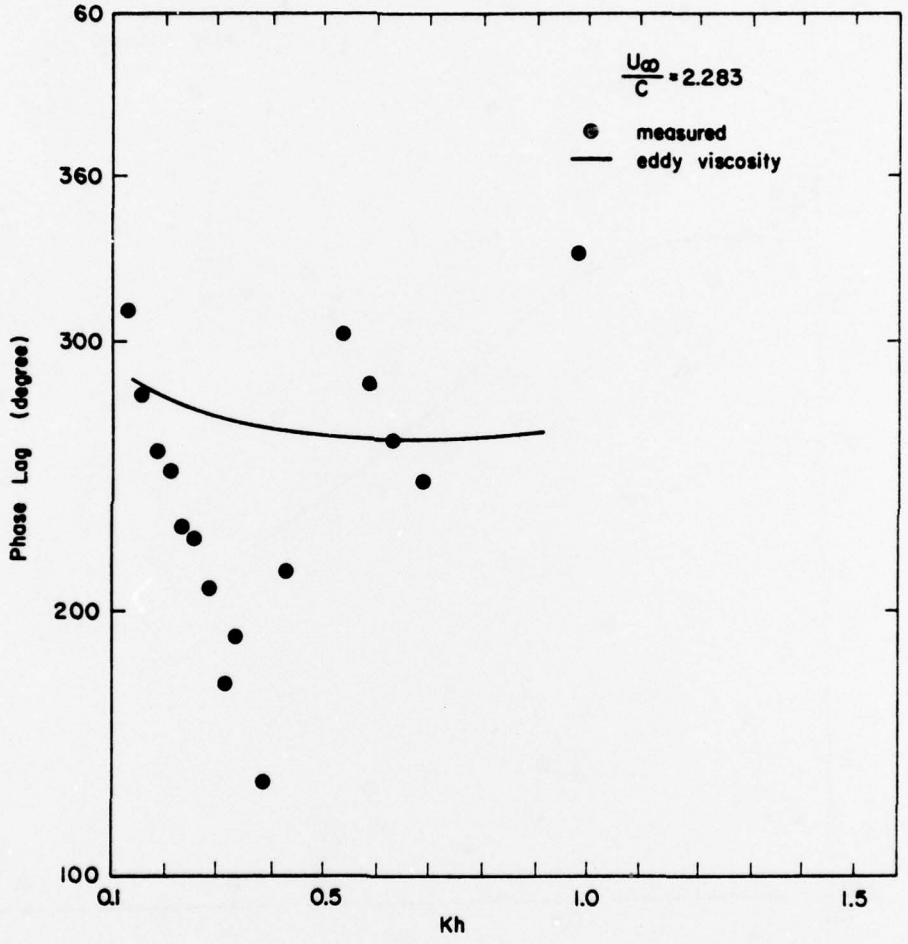


Figure 4.22a Phase Distribution of $\tilde{r}_{11}$ and Computed Results for $U_\infty/C = 2.283$

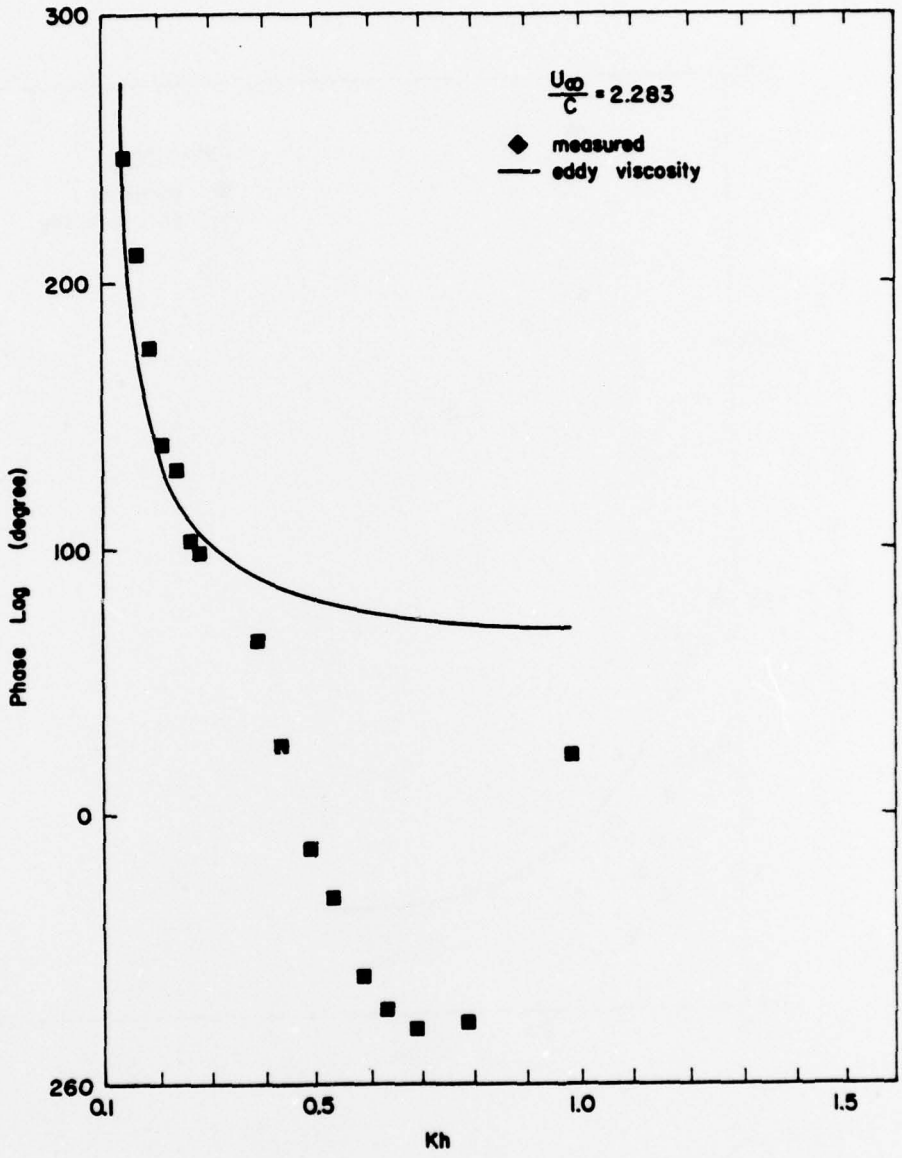


Figure 4.22b Phase Distribution of $\tilde{r}_{22}$ and Computed Results for $U_\infty/C = 2.283$

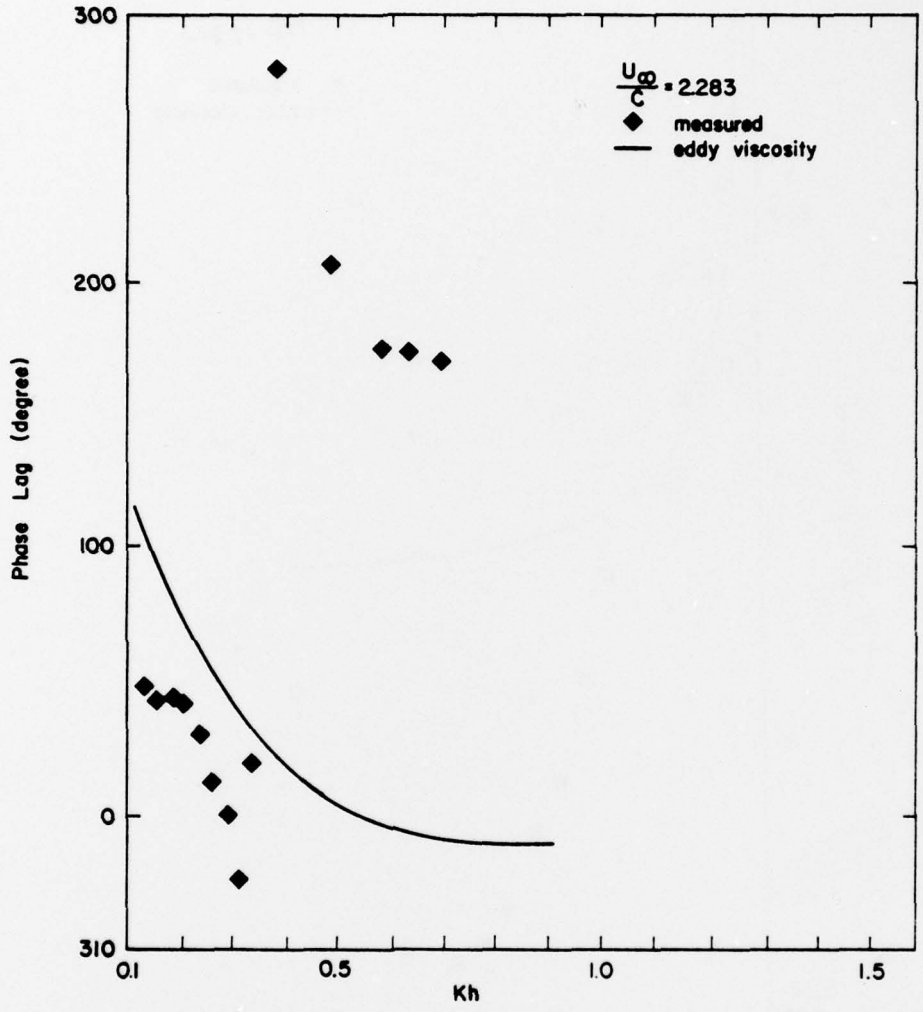


Figure 4.22c Phase Distribution of $\tilde{r}_{12}$ and Computed Results for $U_\infty/C = 2.283$

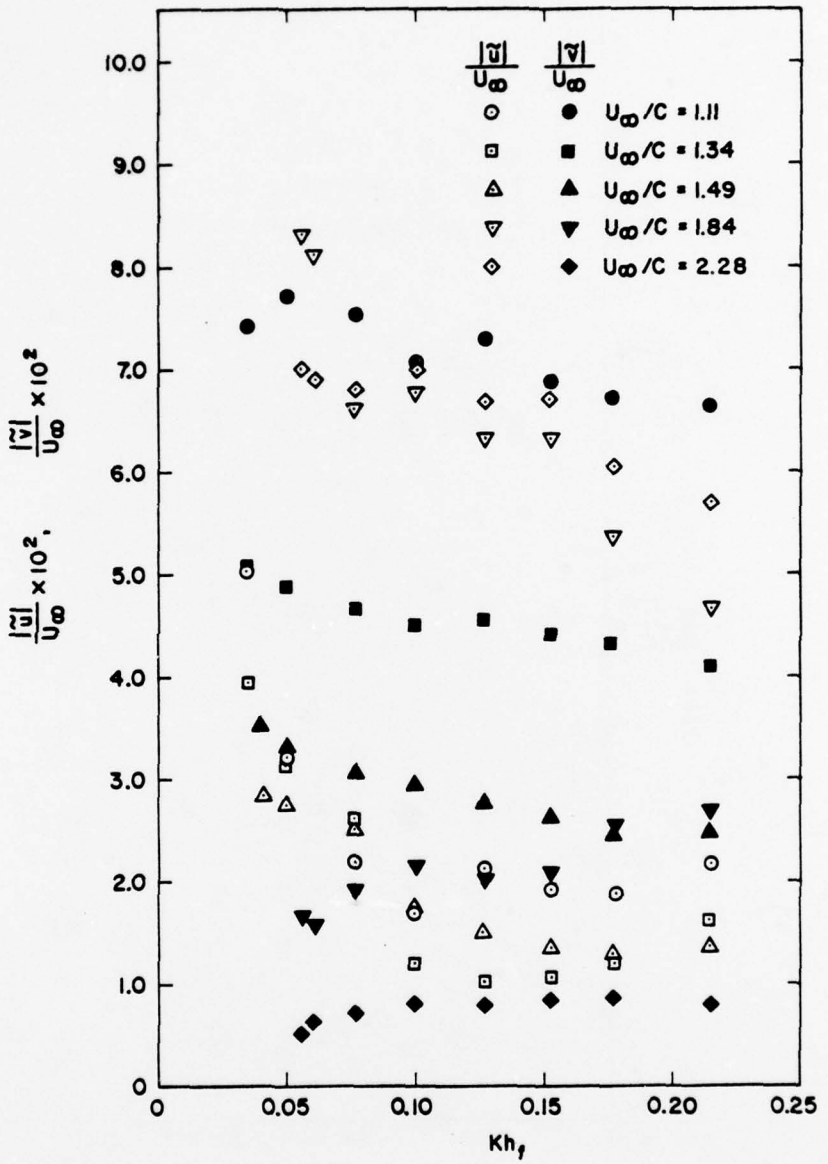


Figure 4.23 Magnitude Distributions of Wave Induced Velocities: Wave Follower Results

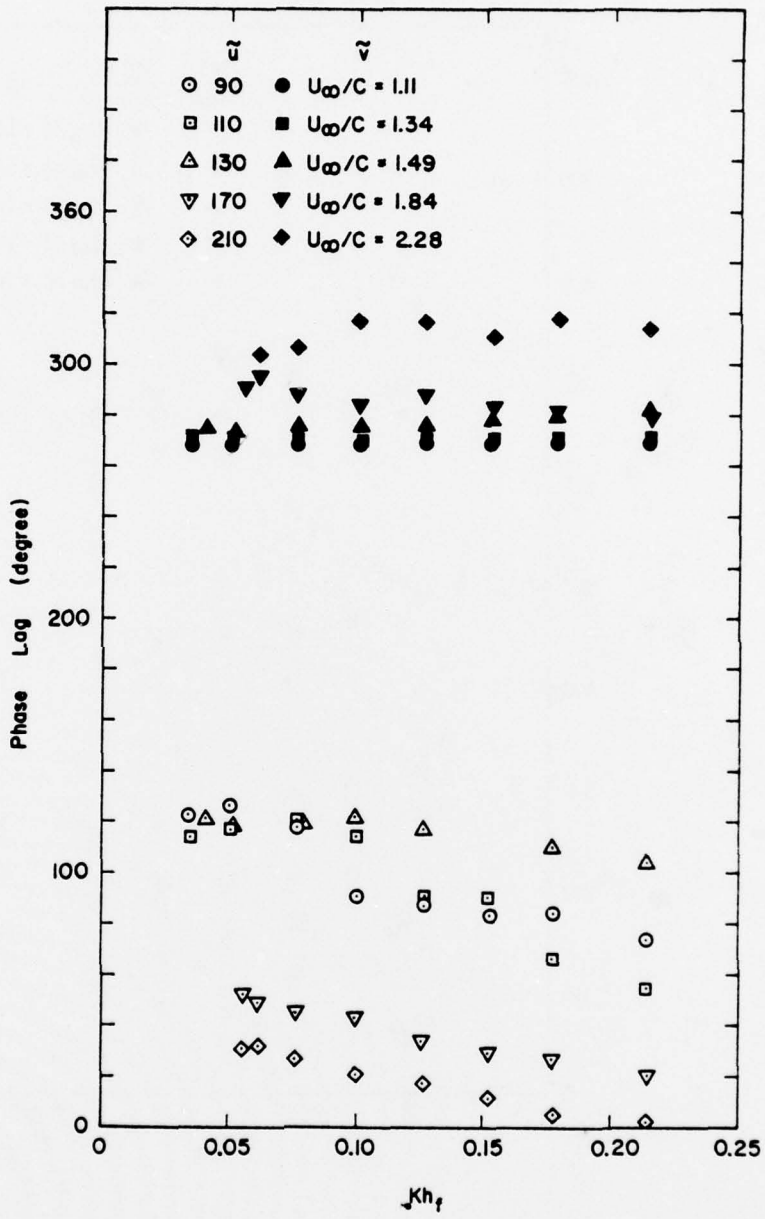


Figure 4.24 Phase Distributions of Wave Induced Velocities: Wave Follower Results

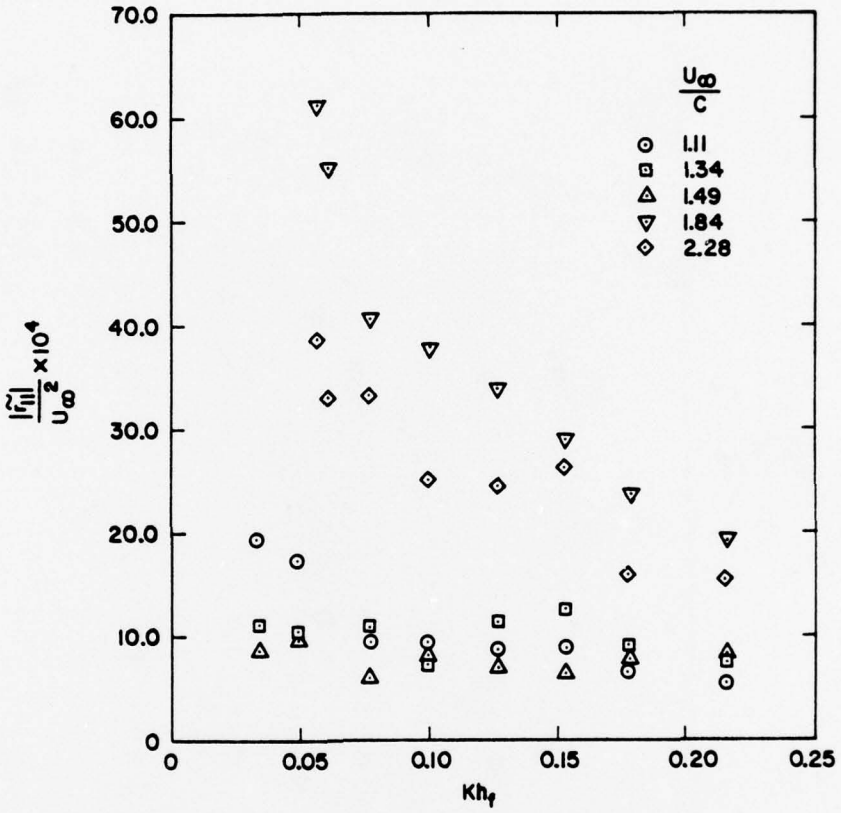


Figure 4.25 Magnitude Distribution of $\tilde{r}_{11}$: Wave Follower Results

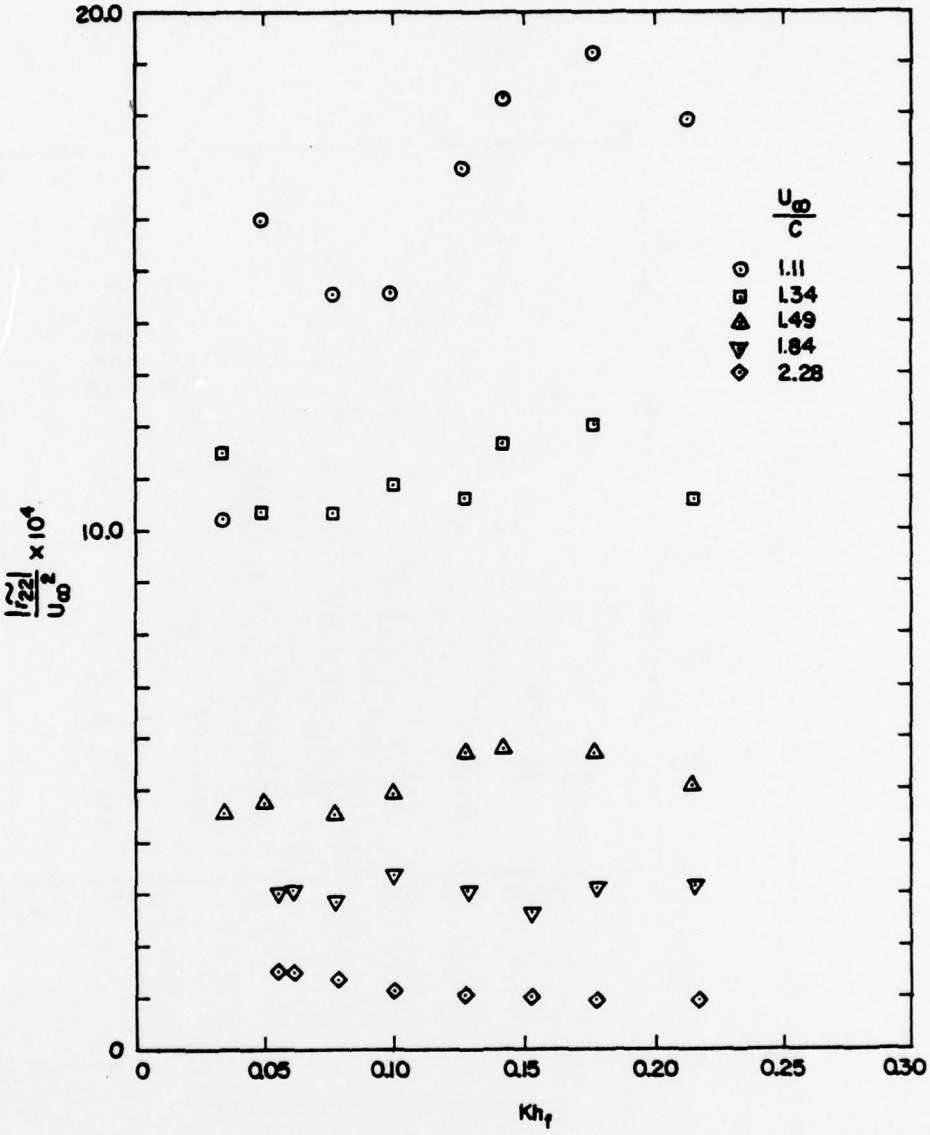


Figure 4.26 Magnitude Distribution of $\tilde{r}_{22}$: Wave Follower Results

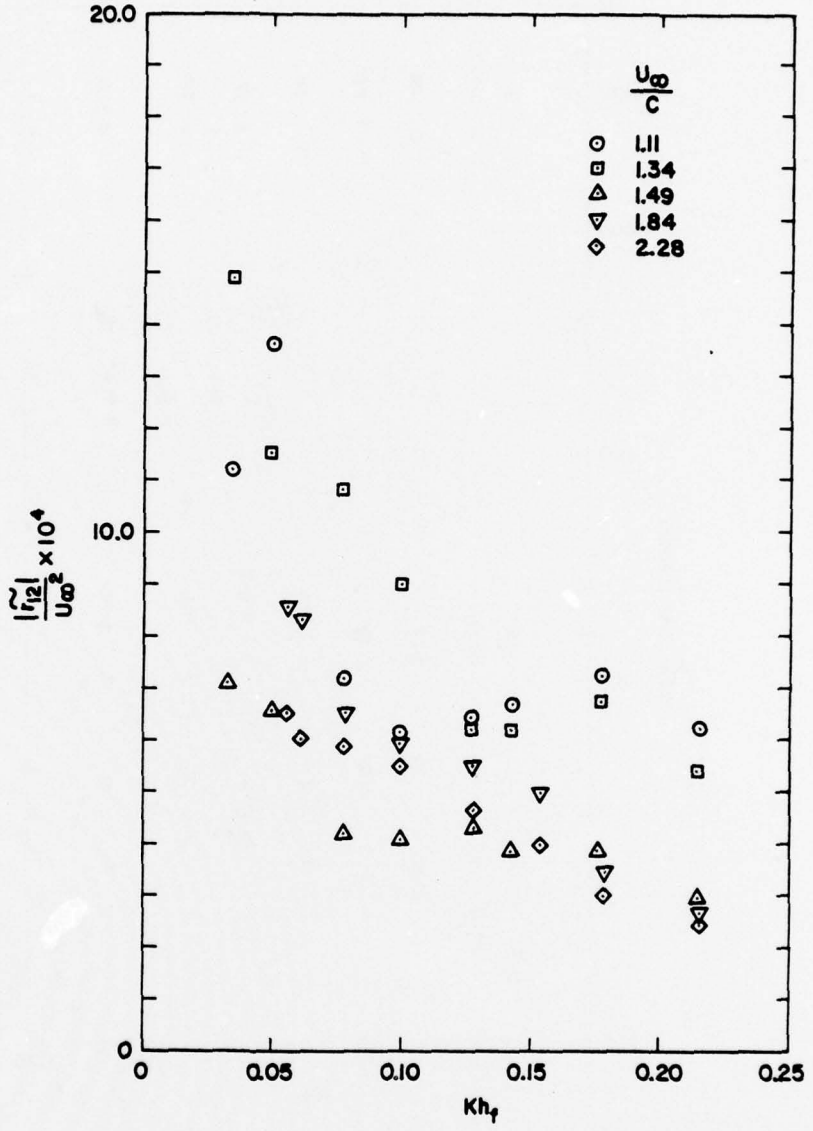


Figure 4.27 Magnitude Distribution of $\tilde{r}_{12}$: Wave Follower Results

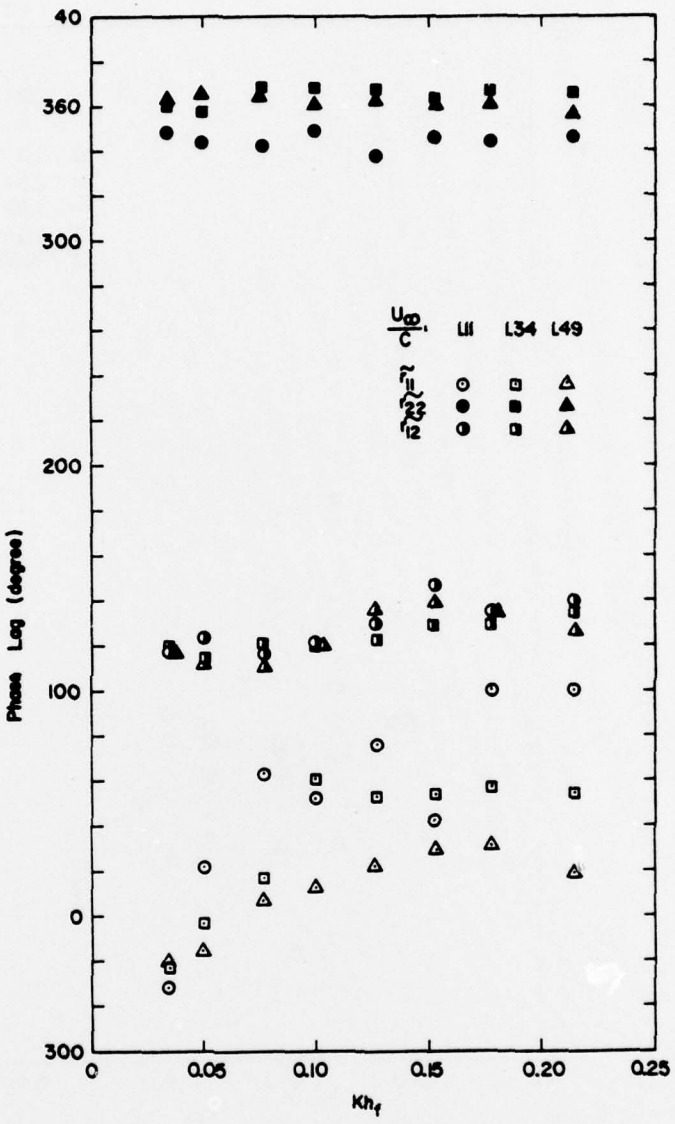


Figure 4.28a Phase Distributions of $\tilde{r}_{ij}$: Wave Follower Results

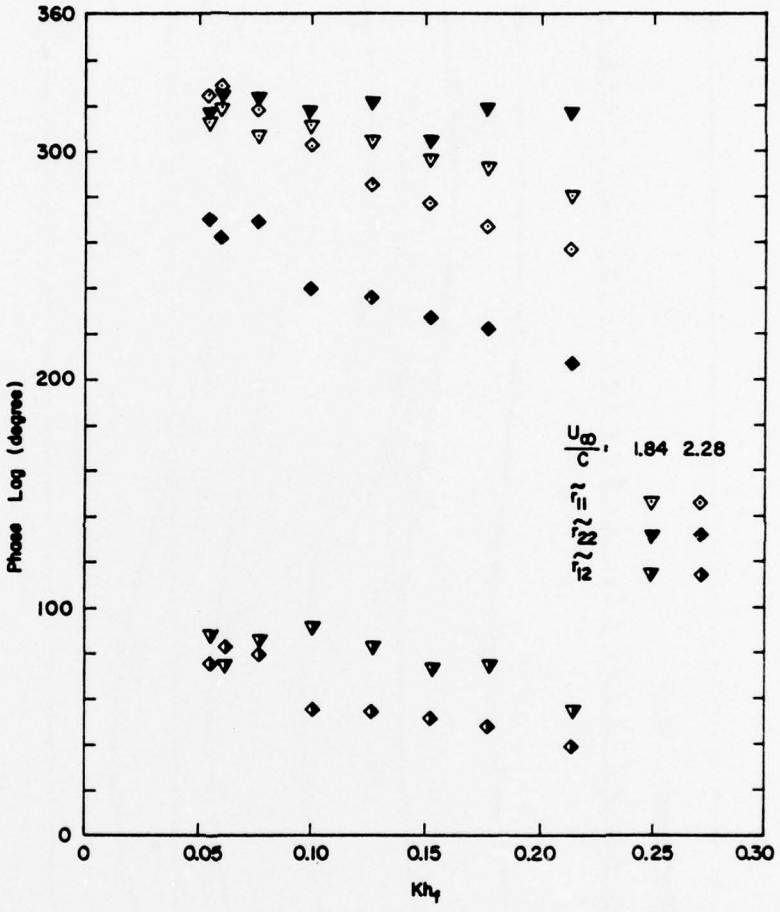


Figure 4.28b Phase Distributions of $\tilde{r}_{ij}$: Wave Follower Results

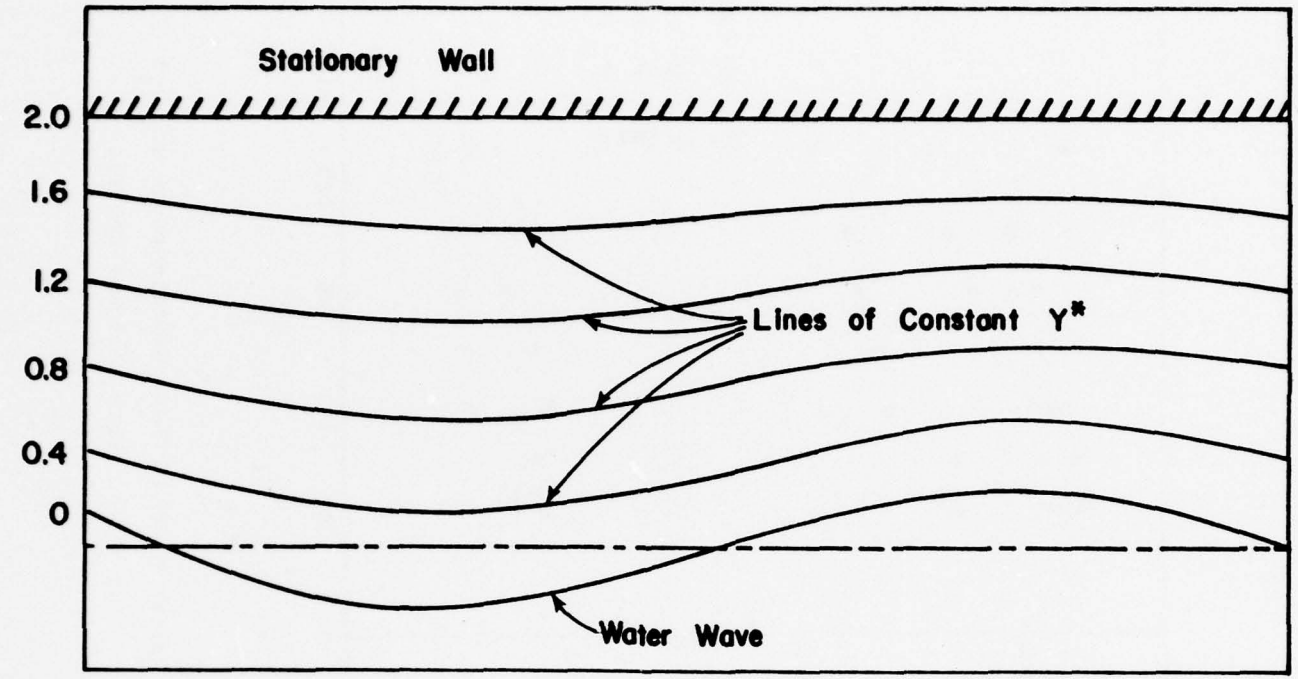


Figure 5.1 Lines of Constant y*

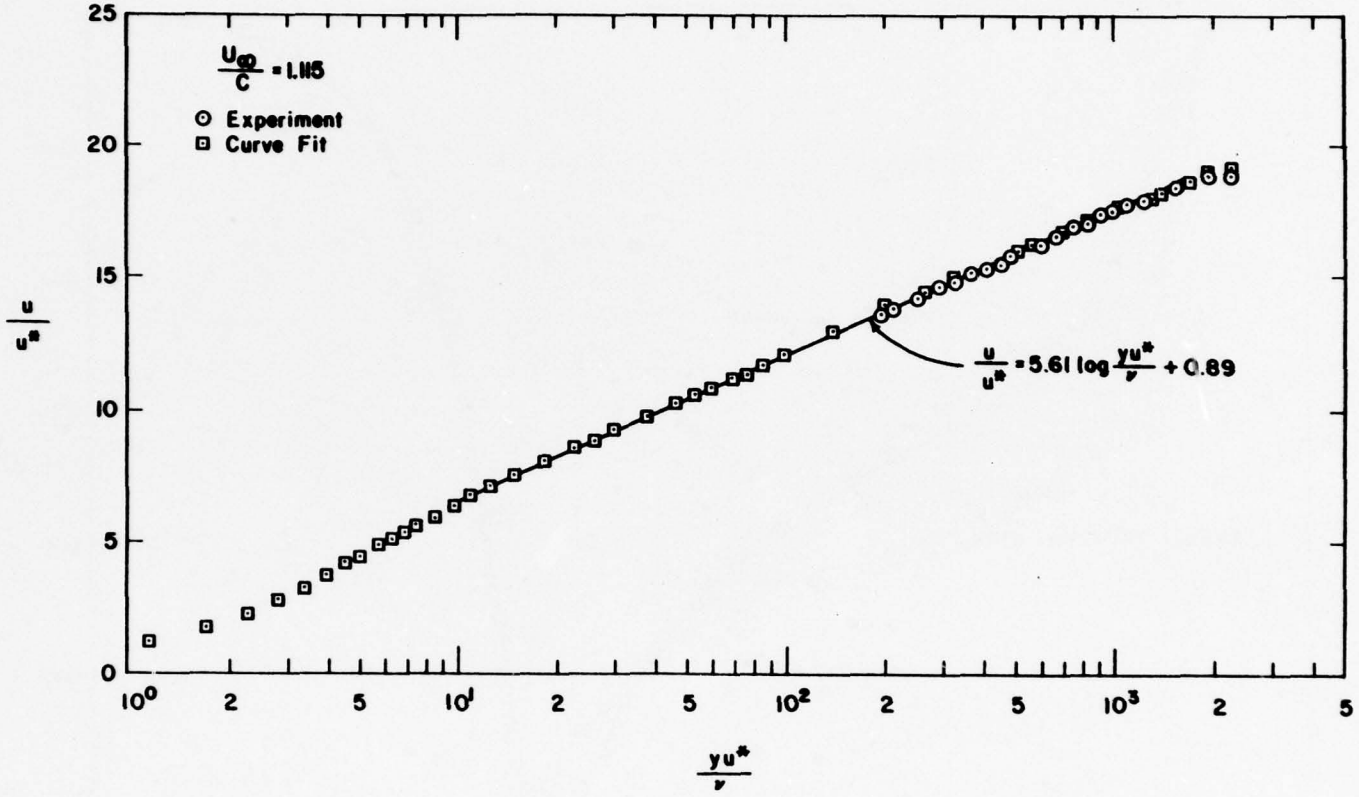


Figure 5.2 Comparison of Mean Velocity Profile

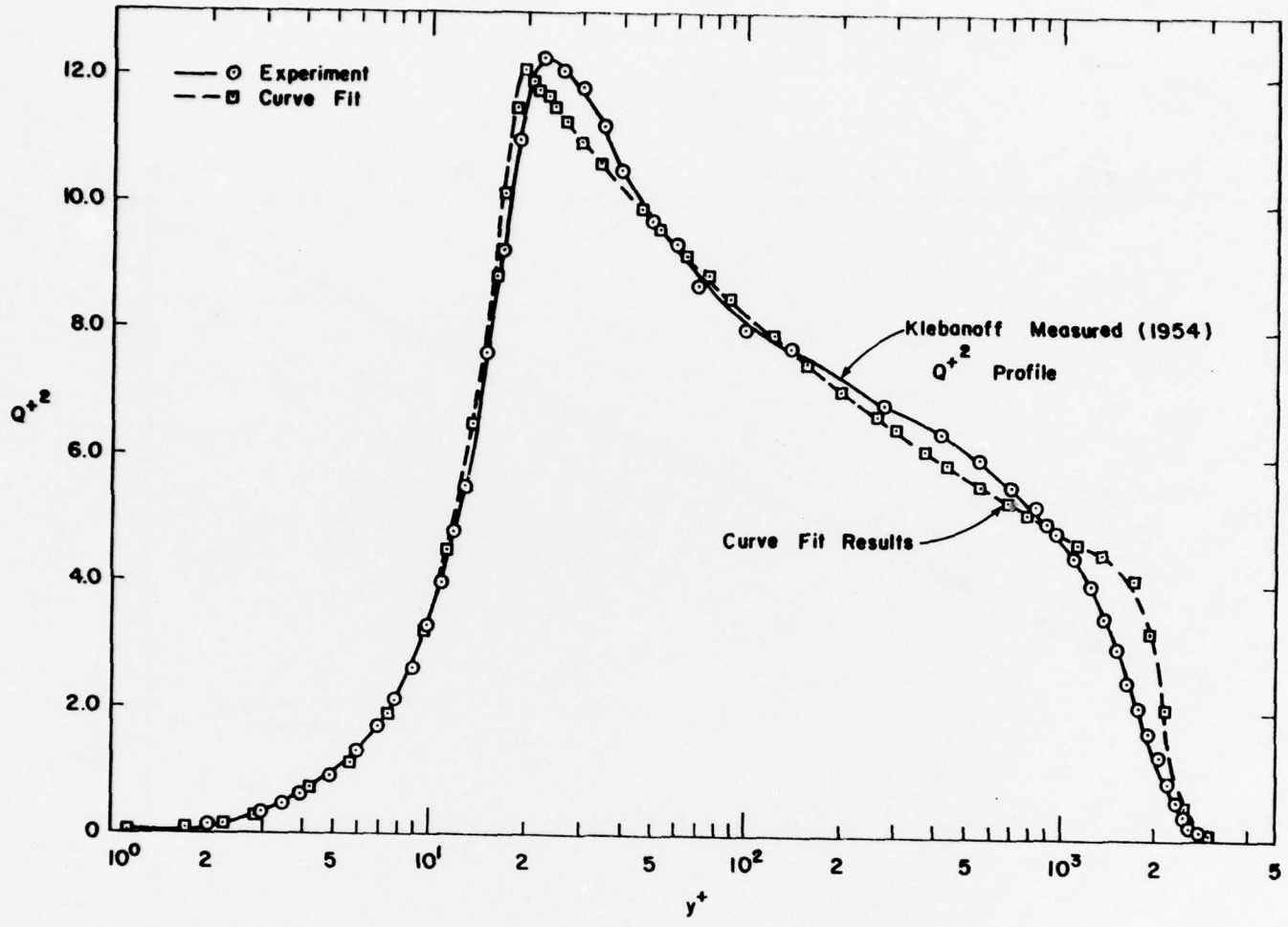


Figure 5.3 Comparison of Turbulent Kinetic Energy